Light Management in Photovoltaics and Photoelectrochemical Cells using Tapered Micro and Nano Structures

Thesis by

Sisir Yalamanchili

In Partial Fulfillment of the Requirements for the degree of

Doctor of Philosophy

CALIFORNIA INSTITUTE OF TECHNOLOGY

Pasadena, California

2019

Defended December 5, 2018

Acknowledgements

I would like to begin with thanking Caltech community and the materials science department for the opportunity they provided for me to improve intellectually, professionally, and personally. My last five years at this place has not just made me a better thinker and problem solver, it also gave me the confidence in my abilities and ideas.

I am very grateful for my advisers Harry Atwater and Nathan Lewis for giving me the opportunity to be part of their fantastic groups through which I had a chance to find a lot of collaborators for research and some close friends. In these two groups I found a lot like minded individuals who are motivated to find creative solutions for important energy and environment related problems. I want to thank Harry Atwater for constantly encouraging me to go to conferences and network with people, and for being an integral part of the Sunday soccer team. I can only wish to be able to match a twenty something year old in fitness when I am over fifty. I would like to thank Nathan Lewis for giving me all the freedom in the world to figure out my own project, and for dancing and playing games with us after intense scientific discussions during group retreats. Nate's retreats also gave us, the current members of the group to talk to alumni who are doing wildly different things in their carriers to open our mind to the limitless possibilities. I would like to see this tradition to continue. Being part of two different groups I had access to a lot of facilities without which none of the results that are presented in this thesis would have been possible. I would like to thank both my advisors for making sure I was funded until my last day as a Caltech student. I would like to thank my other thesis committee members, Julia Greer, Bill Johnson, and Bill Goddard, who also served in my candidacy committee for taking time out of their busy schedules and being flexible with my defense date changes. I had the opportunity to take classes that were taught by Julia Greer and Bill Johnson in my first year. As a non-materials science major in a materials science program my learning curve during my first year has been very steep and Julia Greer and Bill Johnson played a major part in it.

Most of my time at Caltech has been spent in the Kavli Nanoscience Institute (KNI), without which I wouldn't have realized any of my devices. I would like to thank all the current and former KNI staff including Guy DeRose, Melissa Melendes, Nils Asplund, Nathan Lee, Bert Mendoza, Steven

Martinez, Alex Wertheim, and Matthew Hunt for training me on various fabrication equipment and being patient with me while I learnt different techniques. Keeping fabrication equipment always up and running is not an easy task. Therefore, I would like to thank you all the KNI staff for keeping the facility running 24 x 7, 365 days a year. Along with the technical staff there are a lot of non-technical staff without whom no institution can ever run smoothly. Christy Jenstad, Tiffany Kimoto, Jennifer Blankenship, Lyann Lau, Barbara Mirallas, and finally last but not the least Jonathan Gross have been the reason that the two research groups run so smoothly. I would like to say a special thank you to Jonathan who has been a huge help in scheduling my defense talk and making my life easy with conference travel. I want to convey a special thank you for Kimberley Papadontanakis without whom the Lewis group would not function in an organized manner for editing my manuscripts and helping with my next career move.

I had a lot of mentors during my time at Caltech without whom my learning would have been much slower. Hal Emmer showed me around in the lab, trained me on many experimental techniques, and has been a mentor in my first couple of years. He let me just walk into his office without notice and disturb him from his work with a lot of questions. Without Hal I would have taken a lot more time to become a productive researcher. Kate Fountaine has continued to be my go-to person whenever I needed some advice and help with optical simulations and writing papers. She has always been enthusiastic to work with me due to our mutual interest in nanowires and nanocones, and without her contributions I would have certainly taken a much longer time to complete my projects. I want to thank Christopher Chen for his help with transmission electron microscopy (TEM) and tolerating me while I fell asleep when he was showing me the TEM sample preparation. I want to thank Shu Hu for asking me to look up alternate ways to make Si microwires. Due to that advice I learnt dry etching techniques which were a main part of me being able to fabricate a lot of interesting structures for my work in this thesis.

I want to acknowledge Mita Dasog and Azhar Carim for proving me wrong when I said something in the lines of our project seems to silly and obvious, for their contributions for the paper that is responsible for chapter 4 of this thesis that resulted in a publication in nano letters. Erik Verlage and Sophia Cheng have been an integral part in the TiO_2 nanocone project. Looking back at a time when we had no clue about how to fabricate them to ending up realizing a working TiO_2 cone device, this project has been a very long journey which, without their important contributions wouldn't have

been possible. Sophia has been a very helpful KNI partner who helped me with a lot of electron beam lithography, and her never give up on a hard fabrication project attitude is very infectious. Paul Kempler has been my go-to electrochemistry collaborator, who despite our different working styles made our collaborations fruition into a manuscript. I am looking forward to Paul taking the Si microcones to a new level by realizing future devices using them.

During my PhD I have been an integral part of "ETC" team where ETC stands for effectively transparent front contacts. Rebecca Saive has led this project during her time as a post doc in Atwater group. Because of Rebecca reaching out to me for making hard masters I had a chance to be a close witness to an idea starting as a research project and ultimately into a startup led by Thomas Russel, along with multiple publications and patent applications in that process. I am very excited to see how the ETC story unfold in the future. Colton Bukowsky has been an integral part of the ETC team in the earlier years and continued to be a collaborator on SiO_X nanocones project which is not included in this thesis. I hope one day he will finish writing that paper :). I want to thank him for letting me play with Napa sometimes. In the past year I had a lot of fun working alongside other ETC team members: Kelly McKenzie, Sophia Coplin, Chris van de stadt, and Michael Kelzenberg. I want to thank Sophia for teaching me the PDMS stamp fabrication secrets. I want to wish Kelly all the best for the ETC project and I hope we will see one new dot on the NREL solar cell efficiency chart in near future; no pressure! I want to thank Chris for gifting me his squash racket which he blamed when he lost a bunch of games to me ;). Before I met Mike Kelzenberg, I only heard stories through Hal, and I am very glad I got a chance to work with him. His unending enthusiasm towards science, his ability to mentor students with a lot of patience, his capacity to handle multiple projects, and his vast knowledge about every random topic are an inspiration. I also thank Mike for organizing many group events which were a lot of fun.

Stefan Omelchencko has been my friend and partner in Si / perovskite tandem project that isn't part of this thesis. We persisted on this project for three years, and finally seeing that fruition into a publication gives me immense satisfaction. Stefan was a constant listener of my rants in the office, and a travel buddy to various conferences and to India. I intentionally skipped detailed acknowledgements to Azhar Carim earlier since I know he is one of the people who will take time to read this :). I want to thank you for introducing me to a lot of places to hangout around Los Angeles, inviting me to "events" at his place, and losing a bet to me over the extent of aerodynamic

liftoff of a cap when worn while sitting in the back of a convertible car. I am looking forward to the day he defends his thesis. I thank Katie Hamann for being a wonderful office mate and hiking partner to explore hikes around LA over the last couple of years. Madeline Meier is a fellow coffee addict along with Azhar and Katie with whom I got to know almost every coffee place in Pasadena along with a bunch of Asian restaurants. I thank you for joining us in our meat eating expedites despite being a vegetarian with limited options. Kelly Mouser and I joined the Atwater group roughly around the same time. Kelly was soccer team mate and co-guru for the PECVD. I want to thank her for taking care of the beast and help fix it multiple times. I am sure I would have made things worse without your help.

I want to thank Phil Jahelka for being the responsible one for the beast after I am gone, helping me learn how to use sentaurus, and helping me find my lost files. I want to thank Paul Nunez for entertaining us with his dance and helping me learn a little non-aqueous electrochemistry. I want to thank Yulia Tolstova, Sunita Darbe, Amanda Shing, Ke Sun, Deep Jariwala, Michael Litcheman, Fadl Saadi (mere jaan!), Giulia Tagliabue, Michelle Sherrot, Dagny Fleishman, and Keith Wong for taking time out for giving me scientific, grad school, and career advices at multiples times. I thank Joeson Wong, Zak Al Balushi, and Souvik Biswas for inviting me to Burgers and Bourbon Tuesdays. I hope this tradition continues. I thank David Needle, and Pankaj Jha for being part of the soccer team and being the goalkeepers, we needed. Softball was an integral part of my every summer as a grad student. John Lloyd, Michael Floyd, Rebecca Glaudel, and Cora Went are my predecessors and successors to lead Atwater softball team. I want to thank them for their commitment and I hope the team keeps growing. Dan Torelli was the captain of Cold Fusion soft ball for all I knew until Charlie Hansen took over after his graduation, and I want to thank Dan for making me the crazy pitcher as some people may end up remembering me. Mike Wong was my Cambrian Explosion co-captain when we had that unforgettable unbeaten season, and thanks to him this team was the most fun team to play with. I wish Lucas Andrade Meirelles, and Lee Saper, our current team captains all the best, and I am confident that the relaxed atmosphere of our team is safe in your hands. I want to thank other members of the two groups especially Michael Mazza, Haley Bouser, Ivan Morreno Hernandez, Annelise Thompson, Katherine Rinaldi, Jackie Dowling, Pai Buabthong, Ethan Simonoff, Joe Duchene, Yuri Tokponov, and Zachary Ifkovitz for various scientific collaborations, and non-work hangouts. A special shout-out to Ivan for the collaborative project with Si microcone

photoanodes which is also not included in this thesis. I also want to thank my Caltech materials science class especially Andrew Robbins, Ottman Tortuliano, Dylan Tozier, Nick Weadock, Nate Thomas, Michael Floyd, Fred Yang , and Haemin Paik for inviting to their parties.

I want to thank the summer undergraduate research students Eugeen Vaughan, Miranda Schwacke, and Ruby Wallen with whom I got a chance to work with. They helped me learn how to be a mentor.

I want to thank the fellow Indian graduate students at Caltech especially Utkarsh Mittal, Neel Nadkarni, Siddharth Jain, Abhinav Aggarwal, Aditya Date, Ishan Tembekar, Rohit Gurjar, Srikanth Tenetti, Anupama Lakshmanan, Sumanth Dathathri, Pushkar Kopparla, Gaurav Sinha, Subrahmanyam Duvvuri Prachi Parihar, and Kishore Jagannathan for being available to share and discuss very Indian things that others would have hard time understanding. A special thanks to Utkarsh, Neel, Rohit, Siddharth, Abhinav, and Aditya for being my housemates who could tolerate me. A special shout out to Pushkar for travelling to Argentina with me to meet some penguins.

Finally, I want to thank my immediate family in India and my extended family in Los Angeles for continuous encouragement and feeding me and sending me delicious food. Without their encouragement I wouldn't have gotten this far in my career. I sincerely apologize if I ended up forgetting anyone in this long list of acknowledgements.

Sisir Yalamanchili
November 2018
Pasadena, CA

Abstract

Enhancing the efficiency and reducing the cost of solar photovoltaic (PV) systems is critical for increasing their penetration into energy generation market. The intermittency of energy generation from such systems due to diurnal, seasonal, and weather-related variation of sunlight limits them to low capacity factors (typically ~ 25%). Therefore, despite the cost of electricity from solar PV systems being cost competitive, further reductions are necessary to incorporate storage and increase the fraction of solar energy in total energy generation. An integrated photoelectrochemical (PEC) system that can generate fuel directly from sunlight could potentially reduce the balance of systems cost that dominates current PV systems, and provide an alternative way for energy storage. PEC systems are currently in research stage.

In this work conical and triangular micro-nano structures are utilized to explore optical solutions for maximizing the light absorption and therefore enhancing the efficiencies of both PV and PEC systems. Silicon (Si) based micro conical arrays demonstrate < 1 % Spectrum-and-Angle-Averaged reflection, and absorption nearing ray optic light trapping limit in a 20 μm effectively thick Si substrates. Si microcone based photocathodes prepared for performing hydrogen evolution reaction (HER) show that thick layers of light blocking Pt and Co-P catalysts can be incorporated with only a 6 % photocurrent loss. The light trapping properties of Si micro-cones are a result of efficient coupling of light to available waveguide modes in a conical geometry. Alternatively, TiO_2 based dielectric nano-conical arrays are shown to couple the light to waveguide modes and transmit the light into a planar Si substrate despite covering 54 % of the planar front surface with a light blocking Ni catalyst as an alternative way of light trapping without texturing the light absorber.

Triangular silver (Ag) front contacts in place of conventional flat contacts over PV cells are shown as another alternative for reducing front contact reflection losses and enhancing the efficiency by ~ 1% in Si heterojunction solar cells. These structures are implemented using a polymer stamp prepared from a Si master with triangular groves, and by flowing Ag ink through them. A Si master fabrication method is shown for fabrication of multiple configurations of triangular Ag contacts which can potentially be applied to other PV and PEC systems to enhance their efficiency.

List of Publications

Portions of this thesis have been drawn from the following publications

S. Yalamanchili, N. S. Lewis, H. A. Atwater, "Role of Doping Dependent Radiative and Non-radiative Recombination in Determining the Limiting Efficiencies of Silicon Solar Cells", 45th IEEE PVSC, 2018.
DOI: 10.1109/PVSC.2018.8547758
S.Y. conceived and performed simulations. The manuscript was prepared by S.Y. with inputs from co-authors.

S. Yalamanchili, H. S. Emmer, N. S. Lewis, H. A. Atwater, "Highly Absorbing and High Lifetime Tapered Silicon Microwire Arrays as an Alternative for Thin Film Crystalline Silicon Solar Cells", 43rd IEEE PVSC, 2999-3003, 2016.
DOI: 10.1109/PVSC.2016.7750213
S.Y. and H.S.E. conceived, designed, and performed the experiments. Manuscript was prepared by S.Y. with inputs from co-authors.

S. Yalamanchili*, H. S. Emmer*, K. T. Fountaine, C. T. Chen, N. S. Lewis, H. A. Atwater, "Enhanced Absorption and < 1 % Spectrum-and-Angle-Averaged Reflection in Tapered Microwire Arrays", ACS Photonics, 3 (10), 1854-1861, 2016.
DOI: 10.1021/acsphotonics.6b00370
S.Y. performed simulations with inputs from K.T.F. S.Y., and H.S.E. conceived, designed, and performed the experiments. S.Y., and H.S.E. prepared manuscript with inputs from all co-authors. (*equal author contributions)

M. Dasog, A. I. Carim, S. Yalamanchili, H. A. Atwater, N. S. Lewis, "Profiling Photoinduced Carrier Generation in Semiconductor Microwire Arrays via Photoelectrochemical Metal Deposition", Nano letters 16 (8), 5015-5021, 2016.
DOI: 10.1021/acs.nanolett.6b01782
S.Y. performed simulations and prepared samples. S.Y. assisted M.D. and A.I.C in preparation of manuscript, and data analysis.

S. Yalamanchili*, P. A. Kempler*, K. M. Papadantonakis, H. A. Atwater, N. S. Lewis, “Integration of Electrocatalysts with Silicon Microcone Arrays for Minimization of Optical and Overpotential Losses During Sunlight-Driven Hydrogen Evolution”, *submitted*
(*equal author contributions)
S.Y. and P.A.K. conceived, designed, and performed experiments. S.Y. and P.A.K. prepared the manuscript with inputs from all co-authors.

S. Yalamanchili*, E. A. Verlage*, W. H. Cheng*, K. T. Fountaine, P. R. Jahelka, P. A. Kempler, R. Saive, N. S. Lewis, H. A. Atwater, “Near Unity Broadband Light Transmission Using Opptical Waveguides in Dielectric Nanocone Arrays”, *in preparation*
(*equal author contributions)
S.Y., E.A.V., and W.H.C. conceived, designed, and performed experiments with inputs from P.R.J., P.A.K., and R.S.. S.Y., E.A.V., and W.H.C. performed simulations with inputs from K.T.F. S.Y. prepared the manuscript with inputs from all co-authors.

Excerpts are included from the below:

R. Saive, A. M. Borsuk, H. S. Emmer, C. R. Bukowsky, J. V. Lloyd, S. Yalamanchili, H. A. Atwater, “Effectively Transparent Front Contacts for Optoelectronic Devices”, Advanced Optical Materials 4 (10), 1470-1474, 2016.
DOI: 10.1002/adom.201600252
S.Y. assisted in sample fabrication and manuscript preparation.

R. Saive, M. Boccard, T. Saenz, S. Yalamanchili, C. R. Bukowsky, P. Jahelka, Z. J. Yu, J. Shi, Z. Holman, H. A. Atwater, “Silicon heterojunction Solar Cells with Effectively Transparent Front Contacts”, Sustainable Energy & Fuels 1 (3), 593-598, 2017.
DOI: 10.1039/C7SE00096K
S.Y. assisted in sample preparation and manuscript preparation

Table of Contents

List of Figures

List of Tables

Chapter 1
Introduction

1.1 Energy

The ability of human beings to utilize energy creatively has seen the human civilization transform from being hunter gatherers to reach for the moon and beyond. Easy access to utilizable energy enabled human beings in their creative pursuits and scientific explorations as they could worry less about their basic needs for survival such as food, water, shelter, and clothing. Many studies show that energy consumption correlates to the standard of living and economic growth [1-3]. According to world bank data nearly a billion people have no access to electricity, which is the easiest way to access energy. Many nations seek to reach the standards of living of the "developed" countries and therefore the global energy demand is expected to raise by another 28 % by 2040 [4, 5]. Fossil fuels continue to dominate electricity generation at, therefore the net CO_2 emissions from manmade sources and global temperatures. International climate agreement aims to limit the raise of global temperature to 2 ^{0}C, and in order to realize that goal, renewable energy sources must start dominating the electricity generation portfolio [6-8]. Solar energy conversion into electricity and fuels is one of the attractive alternatives especially given that the total solar insulation incident on the Earth's surface in less than 2 hours is equivalent to total energy consumption of the world in 2014 [9, 10]. Despite the vast solar resource the current global electricity generation from solar cells is below 2% in 2017 [11].

1.2 Solar Photovoltaics

The solar photovoltaic (PV) market has taken off exponentially in the last decade with an installed capacity of ~ 400 GW [12]. Currently, crystalline Silicon (Si) solar cells dominatethe PV market and account for 95% of the global production. The boom in PV installations over the last 10 years coincided with a reduction in module prices, and an increase in cell efficiency, making PV cost

competitive with conventional electricity generation. Currently the balance of systems cost, which includes installation, wiring, support structures, inverter, and permit costs, account for 70 % of the cost of a fully installed Si PV system [13]. Therefore, any increase in a solar cell efficiency will increase the module efficiency and implies systems that require less area to generate an equivalent amount of electricity. This reduction in area directly translates to a reduction in the balance of systems cost. Current laboratory efficiency record for a Si solar cell stands at 26.6 % [14], and the theoretical limit at 29.4 %, which means there still is some room for improvement. Pushing the efficiency towards the limit is an exciting challenge for scientists, and this thesis attempts to find some ways for achieving that.

Another important limiting factor stopping solar photovoltaics from increasing their penetration into the electricity generation market is its intermittency. The seasonal and diurnal variation of solar insolation coupled with weather related effects limit the capacity factor of solar PV installations to ~ 25 % in best case scenarios. This requires a way to redistribute the electricity generation from photovoltaics in time to match the demand. Currently by ramping up or down, the electricity generation from natural gas power plants which emit CO_2 [15] achieves this redistribution. Alternative could be to store the excess electricity generated from solar when not required and to use it as per demand. A further reduction in PV systems cost is necessary to increase its grid penetration which requires utilizing storage technologies. Another solution could be to build integrated solar fuels system utilizing a photoelectrochemical (PEC) system that can convert sunlight directly into a fuel, which may have the potential for reducing the balance of systems cost. Such a technology is only at a research stage and thus requires many more breakthroughs to be realized in the energy market.

1.3 Thesis summary

In this thesis various nano and micro architectures for optically enhancing the efficiencies of solar PV and PECs are explored. Below is the brief overview of each chapter in this thesis:

Chapter 2 explores the primary factors determining the realistic efficiency limit of a Si based solar cell calculated by including effects of non-radiative recombination pathways using most recent

models, along with unavoidable effects such as radiative recombination, parasitic absorption, and bandgap narrowing due to bulk doping.

Chapter 3 discusses texturing Si into a micro conical architecture that enables record low reflection (to my knowledge at the time of writing) and nearly ray optic limiting broadband absorption in a 20 μm effectively thick Si for PV and PEC applications. The chapter elucidates these optical properties utilizing wave-optical simulations.

Chapter 4 demonstrates a photoelectrochemical method for depositing Au which can act as a catalyst for CO_2 reduction into CO on textured Si micro wire arrays. This method enables visualization of charge carrier distribution profiles by imaging Au deposition patterns and can potentially be extended to other architectures in the future.

Chapter 5 shows the fabrication and characterization of Si microcone based photocathode for performing photoelectrochemical H_2 evolution. This chapter shows that the Si microcones suffer a very minimal photocurrent loss when designs incorporate light blocking catalysts onto them, and therefore could potentially be able to improve the efficiency of a PEC system.

Chapter 6 demonstrates a more general broadband light trapping using dielectric nanocones that is applicable to both PV and PEC systems. This design can incorporate high loadings of metallic front contacts or catalysts, and a proof of principle Si based photoanode system is demonstrated incorporating dielectric nanocones to perform photoelectrochemical oxygen evolution reaction.

Chapter 7 explores another optical light management strategy utilizing triangular shaped Ag front contacts. These triangles were incorporated over Si heterojunction solar cells to demonstrate a ~1% efficiency boost. A fabrication method for facilitating multiple sizes and spacings of these triangular Ag contacts is developed to expand their applicability to other solar PV and PEC technologies.

Chapter 8 concludes the thesis by discussing some ideas that could be an extension of these light management strategies towards improving the efficiencies of PV and PEC devices.

Chapter 2

Realistic Limiting Efficiencies of Silicon Based Solar Cells

2.1 Context

Realizing maximum efficiency in Si photovoltaics is of significant practical and fundamental interest. Shockley-Queisser limit for Si based single junction solar cells is ~ 32 %. This limit assumes that all the light above band gap energies is absorbed, and recombination occurs only radiatively [16]. Auger recombination, free carrier absorption, and bandgap narrowing effects are intrinsic to Si. The efficiency limit for Si including the unavoidable intrinsic effects is 29.43 % [17]. Shockley-Read-Hall (SRH) recombination, and surface recombination also occur in practical devices depending on the defects in the bulk and surfaces. Along with these the thickness of the Si substrate limits the absorption of light. There are various light trapping mechanisms to improve absorption in Si substrates [18, 19]. Lambertian limit [20] gives the maximum absorption in Si under ray optic considerations. Surface texturing is one way to increase absorption, but such a strategy increases the amount of surface area and thus the surface recombination. Reducing the thickness of Si while maintaining light trapping has the advantage of increasing the carrier density resulting in higher quasi fermi level splitting and therefore higher open circuit voltage, provided the surface recombination are kept low. This chapter discusses the effect of these mechanisms one by one [21, 22] for different material qualities, but the effect of bulk doping and thickness of a Si substrate on the maximum achievable efficiency considering all the recombination mechanisms is not explicitly dealt with. In this chapter we show that all these factors when included to calculate the maximum achievable Si solar cell efficiency, there still is room for reaching above the current efficiency record of 26.3 % [23] at an intermediate thicknesses of ~ 80 μm. The optimal bulk doping of Si depends primarily on the fraction of radiative recombination at open circuit voltage, and band gap narrowing, especially in thin Si substrates.

2.2 Numerical Approach

Optical generation in Si substrates was calculated using commercial software package Lumerical FDTD. A rectangular 2D slab of Si was constructed with periodic boundary conditions along *x-axis* and infinite boundary conditions rendered as perfectly matched layers along *y-axis*. Palik data provided by Lumerical was used for modeling Si optical properties. Broadband illumination from 300 nm to 1200 nm was used to calculate absorption in the Si slab. Built in solar generation rate analysis group was used to obtain the photo generated carrier density profile in the Si slab. This optical data was input into a Sentaurus TCAD, a commercial software for device physics simulations. The absorption data was scaled to match the carrier density generated according to lambertian light trapping limit for a Si slab of given thickness to artificially introduce light trapping. The device physics simulations were performed in Sentaurus TCAD. A 2D rectangular slab of Si with varying doping density was constructed in Sentaurus structure editor. Insulator material was introduced at the top and bottom surfaces of the Si. The surface recombination velocity (SRV) was set at this interface and varied between 1 cm s^{-1} to 1000 cm s^{-1} in decade steps. The radiative recombination in the bulk of Si was calculated using a radiative recombination coefficient (B_{rad}) of 4.7 x 10^{15} cm^3 s^{-1} [24]. Auger recombination was incorporated using the default auger coefficients in Sentaurus Device that include carrier injection level dependence of these auger coefficients [25]. Doping dependent SRH recombination model was used by incorporating empirical Scharfetter relation [26]. Finally the degradation of mobility due to doping was incorporated using the Masetti model [27] to simulate conditions for electron and hole transport to the surface and then undergo recombination. In our simulations we assumed a narrow selective contact; therefore, steady state recombination-generation at open circuit conditions can be obtained in the 2D slab of Si via iteratively solving Poissan, and electron and hole transport equations. Under steady state we obtain the distribution of electron and hole densities in Si along with recombination density. Due to thin selective contact approximation we can calculate the open circuit voltage from equation 1 below.

$$V_{OC} = E_{fn} - E_{fp} = \frac{kT}{q} \ln\left(\frac{(N_A + \Delta n)\Delta n}{n_i^2}\right) \quad (1)$$

Short circuit current is extracted by integrating the total photogeneration, and the fill factor is calculated using the empirical model developed by Green, et.al., in an ideal device without series or

shunt resistances [28]. This calculation gives the maximum achievable efficiency of a solar cell using a Si wafer of typical quality available in the market for a given thickness under lambertian light trapping conditions at various SRVs.

2.3 Role of Recombination Pathways in Optimal Bulk Doping

Figures 2.1 and 2.2 illustrate the effect of phosphorus (P) bulk doping optimization in n-Si on the maximum achievable efficiency. In Figure 2.1 the bulk doping was fixed at 10^{15} cm^{-3}, where as in Figure 2.2 (a) the bulk doping was optimized to achieve the maximum efficiency. Figure 2.2 (b) plots the optimized bulk doping value at which the maximum efficiency was achieved. Figure 2.1 and 2.2 together show that an increase in bulk doping counter acts the effect of surface recombination, and this effect is significant in thinner Si with higher surface recombination.

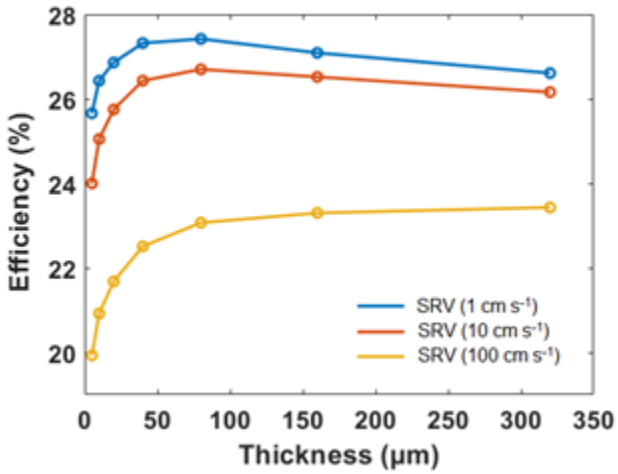

***Figure 2.1**: Efficiency vs Si Thickness plot for constant bulk P doping density of 10^{15} cm^{-3}. Blue, orange, and yellow correspond to SRVs 1 cm s^{-1}, 10 cm s^{-1}, and 100 cm s^{-1} respectively.*

When the bulk doping was fixed at 10^{15} cm^{-3}, the maximum efficiency peaks at ~80 μm thickness at low surface recombination velocities (SRV) of 1 cm s^{-1} and 10 cm s^{-1}. At 100 cm s^{-1} SRV the efficiency increases with increasing thickness while plateauing around 23.5%. When bulk doping is optimized at 10^{17} cm^{-3} the maximum achievable efficiency at SRV of 100 cm s^{-1} peaks at ~80 μm at 25.6%, a considerable 2% more. This effect is even higher for thinner substrates. For 5 μm thick Si

at 100 cm s^{-1} SRV and constant doping of 10^{15} cm^{-3}, maximum achievable efficiency is 19.9%, while at an optimized doping of 5 x 10^{17} cm^{-3} it is 23%, a 3% change in efficiency.

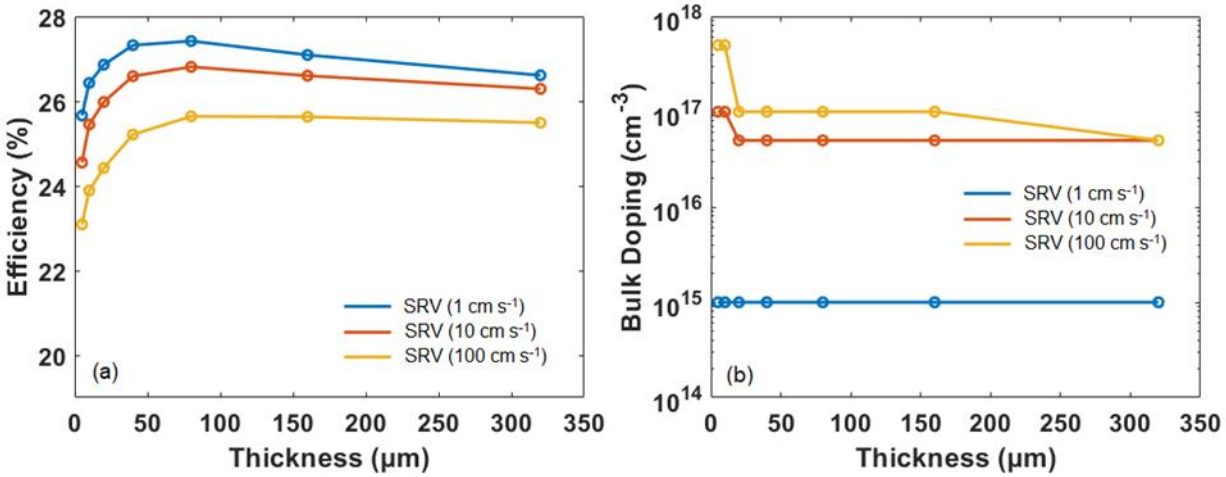

Figure 2.2*: (a) ad (b) plot optimum efficiency and corresponding optimized bulk P doping density respectively vs thickness with same color code as Figure 1*

Figure 2.3 explains the reason for increase in efficiency that comes with an increase in bulk doping. Figure 2.3 (a) and (b) plot the change in maximum open circuit voltage of 80 μm and 20 μm thick Si solar cells while the bulk doping was varied while the SRV is kept constant. Figure 2.3 (c) and (d) plot the fractions of radiative (Rad), auger (Aug), SRH, and surface (Sur) recombinations at open circuit voltage for the case of 100 cm s^{-1} SRV for 80 μm and 20 μm thick Si respectively under various bbulk doping densities. At open circuit voltage no current is flowing, therefore all the photo generated carriers are recombining via various pathways. At low bulk doping the primary recombination pathway at open circuit voltage is surface recombination accounting for nearly 50% of photo generated carriers. As the doping density increases, the fraction of auger and radiative recombination increase due to increase in the product of electron and hole concentrations. According to equation (1), this increases the numerator and thus the open circuit voltage. This is consistent with the results shown here [29]; where higher radiative emission corresponds to higher open circuit voltage. It was observed in Figure 2.3 (c) that open circuit voltage peaks at a bulk doping of 10^{17} cm^{-3} for 80 μm thick Si and so does the radiative recombination. But for 20 μm thick Si the radiative recombination peaks at a higher doping of 5 x 10^{17} cm^{-3}, while open circuit voltage peaks at 10^{17} cm^{-}

[3]. This discrepancy in case of thinner Si is a result of band gap narrowing effect that becomes prominent at very high bulk doping. Band gap narrowing results in an increase in intrinsic carrier concentration, thus increasing the denominator in equation (1) as shown in Figure 2.4 according to updated slotboom model employed in this case [30]. Therefore, a reduction in open circuit voltage appears.

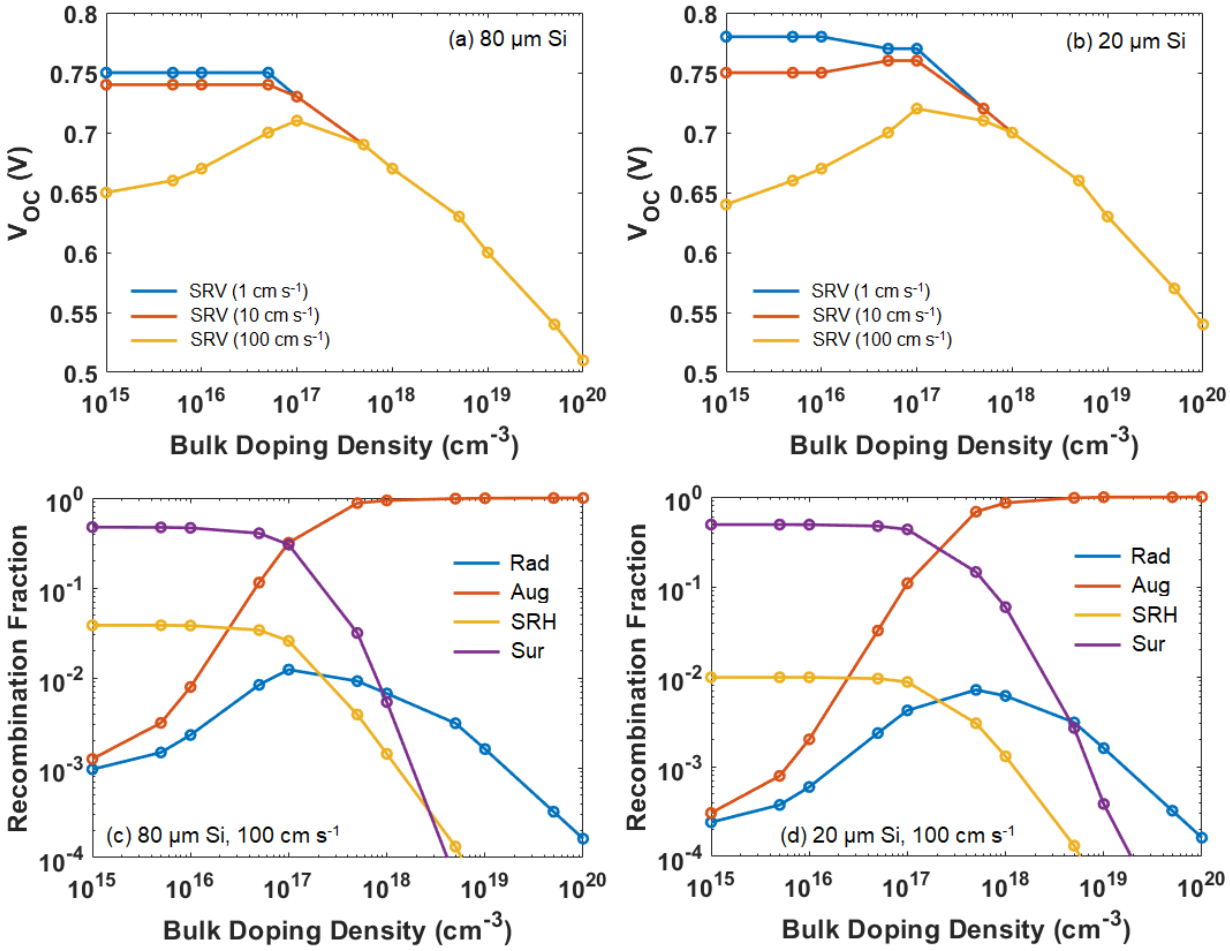

***Figure 2.3**: (a) and (b) plot the variation of maximum achievable open circuit voltage wrt. Bulk doping density for 3 different SRVs. (d) and (e) plot the fraction of each recombination pathway using which the photogenerated carriers recombine in 80 µm and 20 µm thick Si*

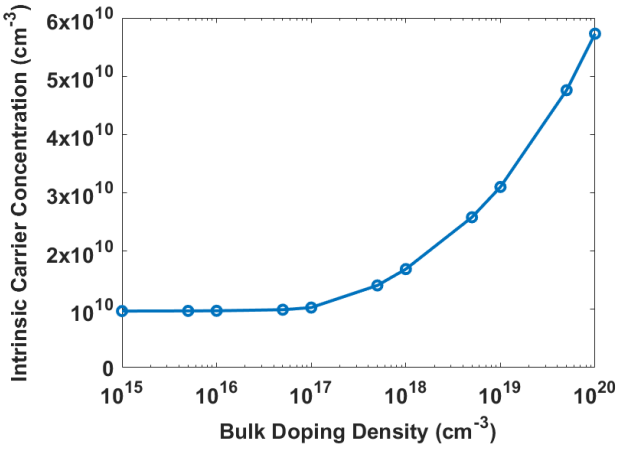

***Figure 2.4**: Plot of change in intrinsic carrier concentration according to slotboom model of band gap narrowing*

2.4 Conclusion

In conclusion we show that when we consider all radiative and non-radiative recombination pathways, the performance of a Si based solar cell was maximized by optimizing the bulk doping. It is shown such that the doping offsets the effect of high surface recombination by increasing the fraction of radiative recombination. In general, a change in the doping concentration can improve the open circuit voltage in cases where non-radiative recombination is high, as long as the doping is not too high for the band gap narrowing effect to start counteracting. Si solar cells typically employ surface texturing for light trapping, increasing the total surface area and thus the total surface recombination. Especially in case of thin silicon substrates to achieve lambertian light trapping elaborate high aspect ratio nano/micro structures [31, 32] are required. In such cases the surface area increase can be an order of magnitude. Therefore, the doping density in the bulk was optimized accordingly in these cases to achieve maximum voltage and hence efficiency.

Chapter 3

Silicon Microcone Arrays

3.1 Introduction

Reaching towards the ultimate conversion efficiency limits for Si photovoltaics is of considerable fundamental and practical interest and motivates research on thin Si solar cells with high minority carrier lifetimes and extremely efficient light management. While the limiting efficiency [16] for a single-junction crystalline Si solar cell under 1 sun illumination of 29.43% with the only constraints of free carrier and Auger absorption losses [33], [34], record experimental Si cells have reached efficiencies as high as 25.6% [35]. To achieve higher efficiencies, lower surface recombination velocities were to be achieved in structures with very efficient light management that enable a reduced bulk recombination by virtue of reduced absorber volume in the solar cell. Current high-efficiency Si solar cells utilize intrinsic amorphous silicon (i-a-Si) [36]or Al_2O_3 [37] surface passivation layers that produce very low surface recombination velocities, so that the cell performance is typically limited by the bulk carrier lifetime. Consequently, a further decrease in bulk recombination could lead to yet higher cell efficiencies. Heterostructure with intrinsic thin layer (HIT) Si solar cells have demonstrated an efficiency enhancement by the use of thinner substrates [36]. In such HIT cells, the dark current due to recombination is reduced compared to the current under illumination, increasing the quasi-Fermi level. Use of even thinner substrates would be desirable in order to reduce the bulk recombination volume, but the indirect band gap of Si yields reduced absorption in very thin samples. Additionally, the surface/bulk ratio increases as the substrate becomes thinner. The optimal Si cell thickness thus depends strongly on the achievable surface recombination velocities as well as on the ability to achieve enhancements in light trapping. Optoelectronic transport calculations indicate that with realistic surface recombination velocities, and high bulk material quality, efficiencies as high as 24.4% was achieved in a 10 μm thick cell [38] if the light trapping were at the $4n^2$ Lambertian limit [20]. It was also suggested that modulated silicon nanowire photonic crystal architectures have the potential to reach 15 – 20 % solar cell efficiencies in only 1 μm equivalent thick silicon [39]. Previous demonstrations of thin film

crystalline Si cells with effective thickness under 50 μm with various light trapping schemes include: 20.62% efficiency in a 35μm device[35], 19.1% in a 43μm thick device [40], 16.8% in a 20μm thick device [41], 15.7% [42] and 13.7% [43] in 10μm thick devices .

Researchers have explored various nanostructured antireflection and light-trapping strategies for thin-film crystalline Si [44],[19]. Some recent studies have shown limitations in light-trapping structures arising from parasitic absorption, as opposed to limitations in the Si absorber material of the cell. Hence structuring the absorber layer to maximally harvest light while minimizing parasitic absorption and reflection losses, was required to maximize absorption in thin crystalline Si solar cells [45],[46],[47]. Si microwire arrays facilitate light absorption near the $4n^2$ limit for very small Si planar equivalent thicknesses, [48] with reports of absorption exceeding the $4n^2$ limit near the band edge. However to date, Si microwires fabricated by vapor- liquid-solid growth methods using metals such as Au or Cu as growth catalysts have not demonstrated high minority carrier recombination lifetimes, since these metals can produce defects that reduce the bulk recombination lifetime in Si [49],[48].

We fabricate Si microwires with high minority carrier bulk lifetimes using cryogenic inductively coupled plasma reactive ion etching (ICPRIE), which is predominantly a chemical etch. The etching conditions were modified to taper the Si microwire shape to achieve extremely low, angle- and spectrally-averaged low reflectivity. These arrays were embedded in polydimethylsiloxane (PDMS) and peeled off of their substrate, which can then be reused to etch additional microwire arrays, provided the remaining wafer thickness is sufficient. Such peeled off films exhibited near $4n^2$ light trapping compared to the volumetric equivalent planar Si thin film. Electrodynamic simulations indicate that the tapered Si microwire structure facilitates highly effective coupling of incident light into waveguide modes and yield high optical absorption.

3.2 Fabrication

Czochralski (CZ) and Float Zone (FZ) grown <100> Si wafers were photolithographically patterned into a square grid with 3μm circles of 200nm thick Al_2O_3 mask evaporated over it separated by 7μm. SF_6/O_2 etch chemistry was used in Oxford DRIE System 100 ICP/RIE to perform the etching.

Etching was performed at low capacitive coupled power of 5W to reduce damage due to momentum of ions. A high inductively coupled power of 900 W was used to increase the number of ions in the plasma to reach high rates of chemical etch. Flow of SF_6 was fixed at 70 sccm, O_2 flow was varied from 4.5 - 6.5 sccm, and etching was performed for 30 minutes. Figure 3.1 (b-f) show the change in microwire tapering profiles while O_2 flow was varied in steps of 0.5 sccm from b to f. The tapering of the microwire sidewall vary from being slightly thinner at the bottom compared to the top of the wire to being broad. Increase in O_2 content in the plasma improves the sidewall protection during the etching at low temperatures and therefore results in the change in the taper of the microwires.The rate of etching remained constant at 1 μm/min resulting in microwires with 30 μm height in all the cases.

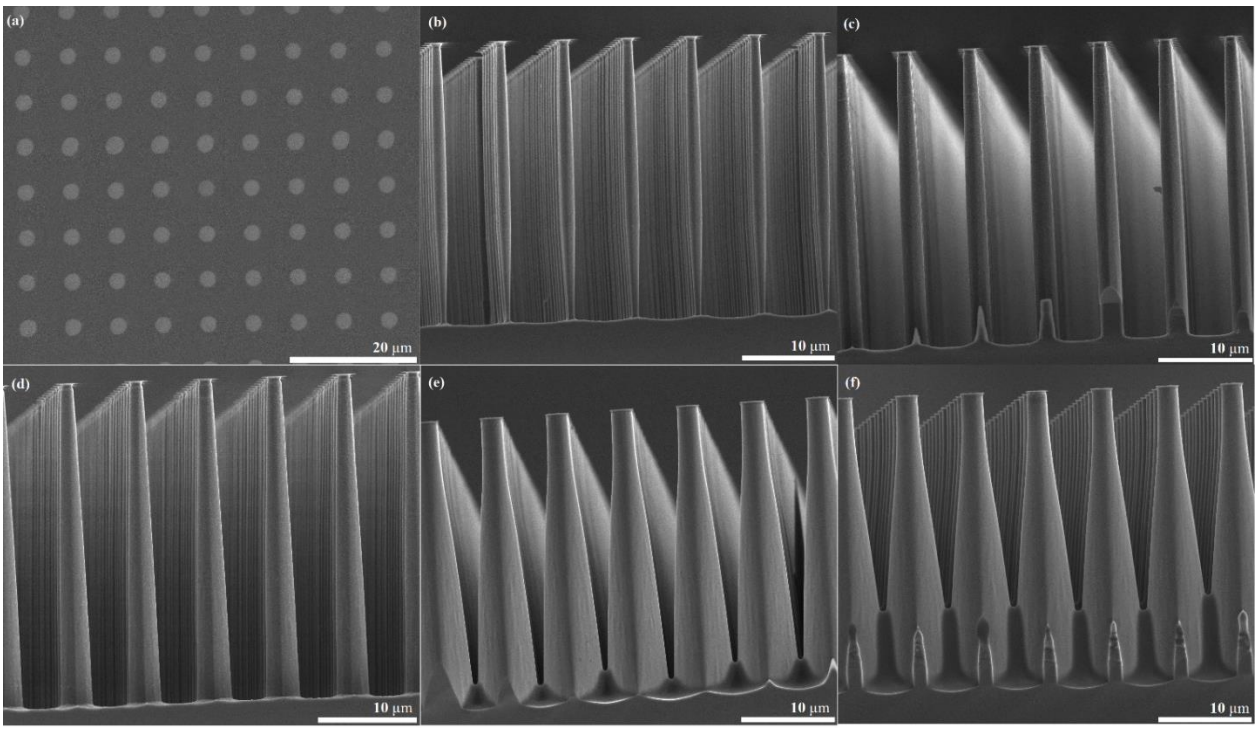

Figure 3.1*: (a) Photolithographically patterned Si substrates with Al_2O_3 etch mask. (b) - (f) show the etch profiles of the microwires as O_2 flow during the etching varies from 4.5 – 6.5 sccm in steps of 0.5 sccm. Al_2O_3 mask can be seen at the top of the wires.*

Figure 3.2 shows the optimized morphology of the microwires with a pointed tip and gradual taper to achieve minimum reflection. These tapered microwires have a top tip diameter < 100 nm, a bottom base diameter of 7 μm, and a height of 75 μm. These structures are fabricated by ICPRIE by etching

for 90 minutes while varying O_2 flow at 0.5 sccm at every 30 minutes starting from 5 sccm to 6 sccm. Post etching, the wafers were dipped in buffered hydrofluoric acid solutions to etch away the Al_2O_3 mask. The bar on the silicon microwires visible at 30 µm from the base of the wires was a result of stopping and starting the plasma during the transition from step 2 with 5.5 sccm O_2 flow rate to step 3 with 6 sccm of O_2 flow rate. The samples were then cleaned using modified RCA1 and RCA2 cleaning processes [50].

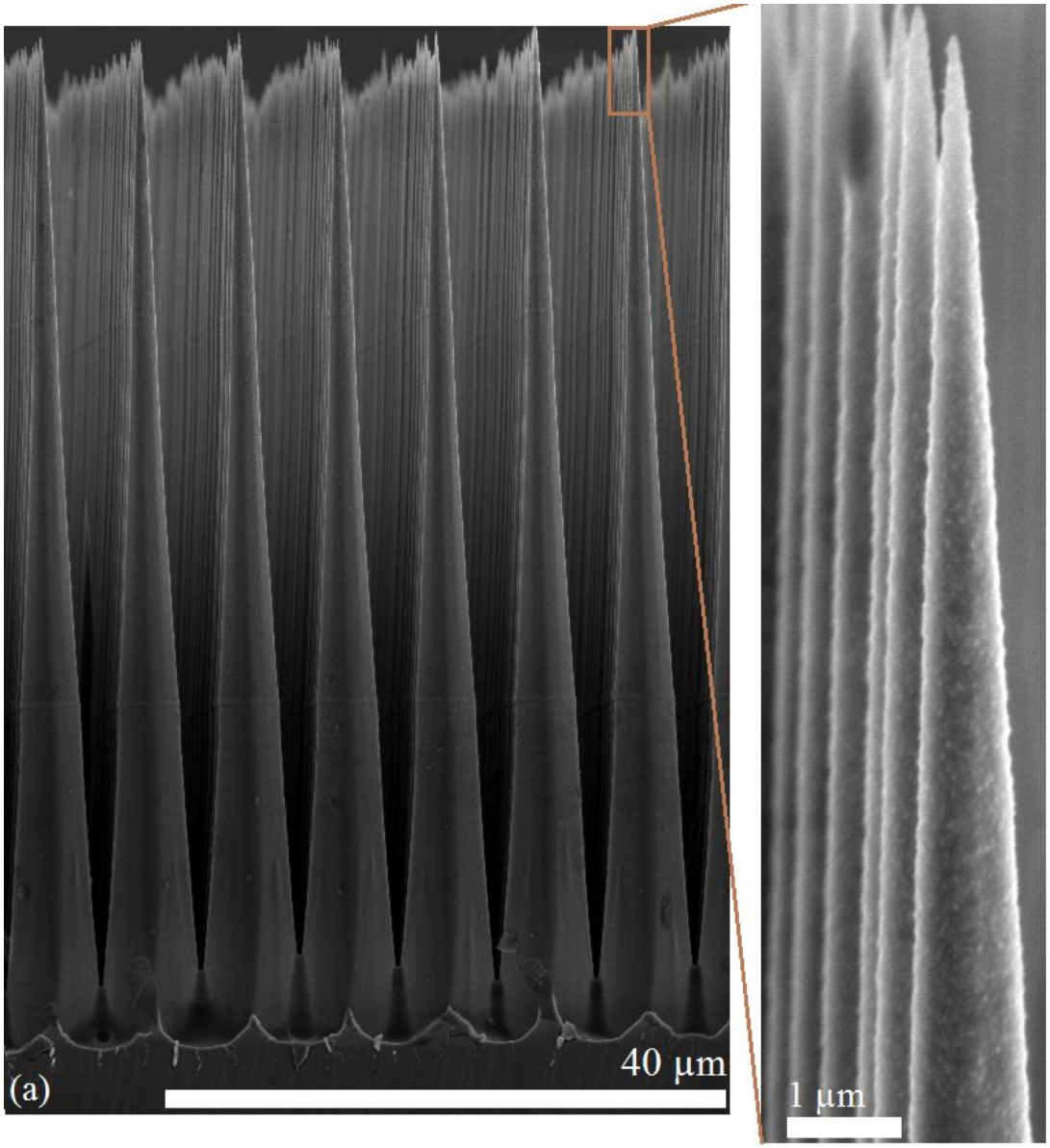

Figure 3.2*: Si substrates with microcone arrays etched via ICPRIE. The inset shows the morphology of the microcone tip.*

3.3 Optical Characterization

Figure 3.3 plots the integrating sphere measurements for reflectivity from etched Si substrates after etching away the Al_2O_3 mask by dipping in 50 % HF solution for 1 minute. The curves labelled from (b) – (f) represent change in reflectivity from the etched substrates due to varying taper of microwire arrays in an order consistent with Figure 3.3 (b) – (f). The reflectivity decreases from (b) to (d) and starts going up for (e). A graded index can explain the changes in [51] since the average index of the medium increases as one moves down from top of the wires to the bottom. In Figure 3.3 (e) due to the broad bottoms the average index transitions from air to Si more gradually than in cases (b) to (d) and therefore has much lower reflectivity. In Figure 3.3 (f) the change in average index from air to Si on the substrate as one moves from top to bottom is quicker compared to Figure 3.3 (e), therefore the reflectivity starts increasing. In all cases discussed till now the top surface of microwires was flat and therefore the surface suffers an unavoidable top surface reflection.

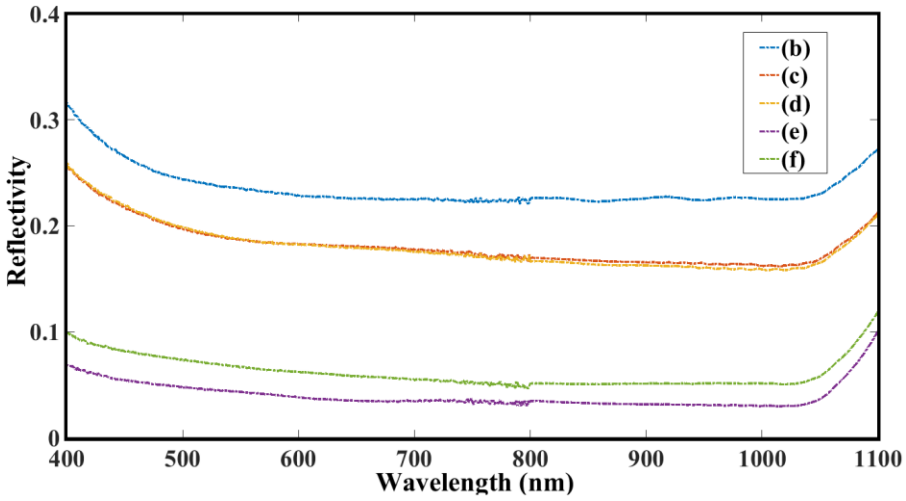

***Figure 3.3**: Curves (b) – (d) show reflectance of Si substrates with etched microwires as shown in Figure 3.1 (b) – (d) after removal of etch mask*

Angle-dependent reflectance measurements of the microcone arrays were performed using tunable monochromatic radiation from a supercontinuum laser and a Si photodetector [48]. Measurements were done on bare Si substrates with microcones and with antireflective SiNx coating. SiN_x was deposited over the Si microcone substrates by plasma enhanced chemical vapor deposition (PECVD)

using an Oxford Instruments Plasmalab System 100. Silane and ammonia gas chemistry was used at 350 ^{o}C and 1 torr at previously optimized conditions for microwire arrays [48].

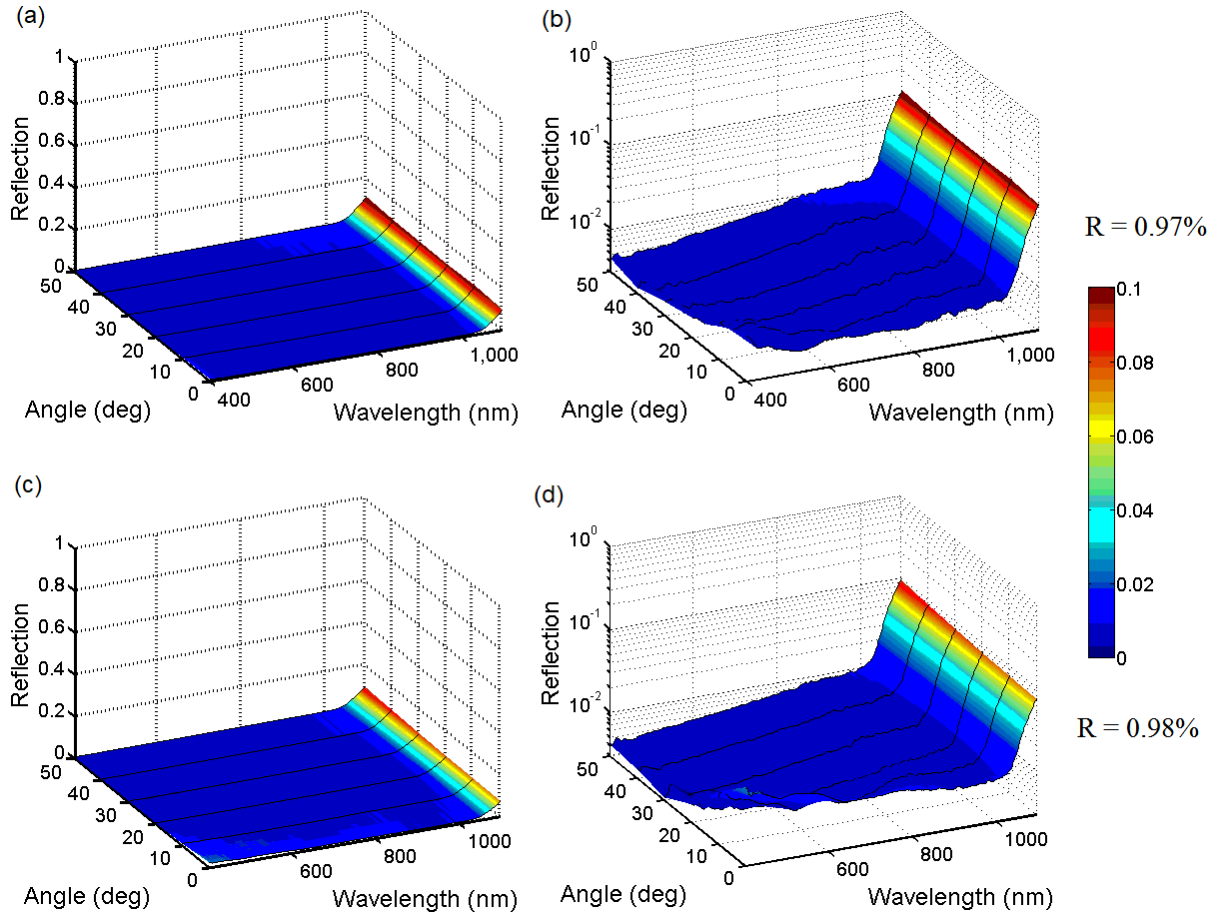

Figure 3.4*: (a) and (b) show the reflectance (0.98%) of Si substrates with microcone arrays measured using an integrating sphere plotted on a linear scale and log scale respectively. (c) and (d) show the reflectance (0.97%) of the arrays with a SiNx anti-reflection coating.*

Figures 3.4 (a) and 3.4 (b) show the measured microcone array reflectance on linear and log scales, respectively, from 400 nm – 1100 nm, while the angle was varied from 0^{0} to 50^{o}. Averaged over 0^{o} to 50^{o} and over the range 400 nm-1100 nm, the integrated reflectance was 0.98 % for uncoated Si microcone arrays and 0.97 % for arrays coated with SiN_x dielectric layers. During these measurements no back reflector was employed. The microcone arrays thus act as nearly ideal antireflection surfaces, not only at normal incidence but also at oblique incidence angles even without any anti reflection coating.

The angular reflectance without and with SiN_x anti reflection coating is shown in Figure 3.4 (a), and (b) and Figure 3.4 (c), and (d) respectively in linear and log plots. The surface reflectance is comparable- -and in some cases lower than-- typical black Si front-surface texturing methods [52]-[53]-[54]. Notably, low reflection was achieved at wavelengths near the Si band gap, i.e., 1000 nm – 1100 nm, where Si has a large absorption length. In the 1000 nm – 1100 nm wavelength range, where the absorption depth is of the order of hundreds of microns, the reflection varied from 3.6 % at normal incidence to 2.7 % at 50^o for uncoated microcones, which is limited by reflection from back surface of the ~300 μm thick sample. In the 400 nm – 1000 nm range, the reflection varied from 0.7% - 0.5%. Although not all previous work has reported angular averages for reflectance, the present result of <1% angular averaged reflection is to our knowledge a record for low reflectance silicon structures and compares very favorably to other methods for reducing reflection in the range 400 nm – 1100 nm, the wavelength range of interest for Si-based solar cells.

In order to experimentally measure absorption in microcone arrays without effects due to the substrate, the uncoated arrays were embedded in ~120 μm thick Polydimethylsiloxane (PDMS) by spin coating a 1:1 by weight solution of Toluene : PDMS at 500 rpm so that all the cones were completely embedded in PDMS to avoid any damage to the tip while handling. The sample was heated on a hot plate at a temperature of 120^0C for 5 hours. The microcone arrays embedded in PDMS were peeled off the surface using a razor blade to obtain flexible films as shown in Figure 3.5 (a) and (b) [55]-[56]. The filling ratio of Si / PDMS in these films was ~1:5. The fill fraction of Si vs height is shown in Figure 3.6. These films were placed on a nearly ideal Lambertian back scattering $BaSO_4$ (6080 White Reflectance Coating; LabSphere) coated sample holder in an integrating sphere, and reflection (R) measurements were performed. The absorption (A) was calculated from the reflectance (R) data by using $A = 1 – R$. Figure 3.5 (c) shows the absorption calculated from the reflection measurement in the integrating sphere from 400 nm – 1100 nm while the angle was varied from 0^o to 50^o. Averaged over 0^o to 50^o, such films showed an integrated absorbed solar spectrum photon flux as high as 89.1%, demonstrating the remarkable absorption properties of these tapered microwire arrays at various incident angles in the solar spectrum of interest. The effective planar thickness of these polymer-embedded arrays calculated assuming a truncated cone with tip radius of 25 nm, base radius of 3.5 μm, and a height of 70 μm is ~20 μm. Figure 3.5 (d) shows semitransparent area plots comparing the total incident photon flux (green),

absorbed solar flux under normal incidence in tapered microwire arrays embedded in PDMS (blue), and absorption for the $4n^2$ light -trapping limit [57] in a 20 µm thick Si slab, after correcting for reflection from the PDMS/air interface (~3%) (red). The grey color in the plot indicates the overlap region of all the three photon flux plots. The total calculated photon flux absorbed at normal incidence was 99.5% of the limit for an equivalent thick Si slab. Each of the films, fabricated by embedding the microcone arrays in PDMS and peeling the microcones off of their substrate and placed on a nearly ideal Lambertian back reflector, showed absorption slightly below the $4n^2$ limit for most of the solar spectrum, and exceeded the limit at wavelengths near the Si band gap (1050 nm – 1100 nm).

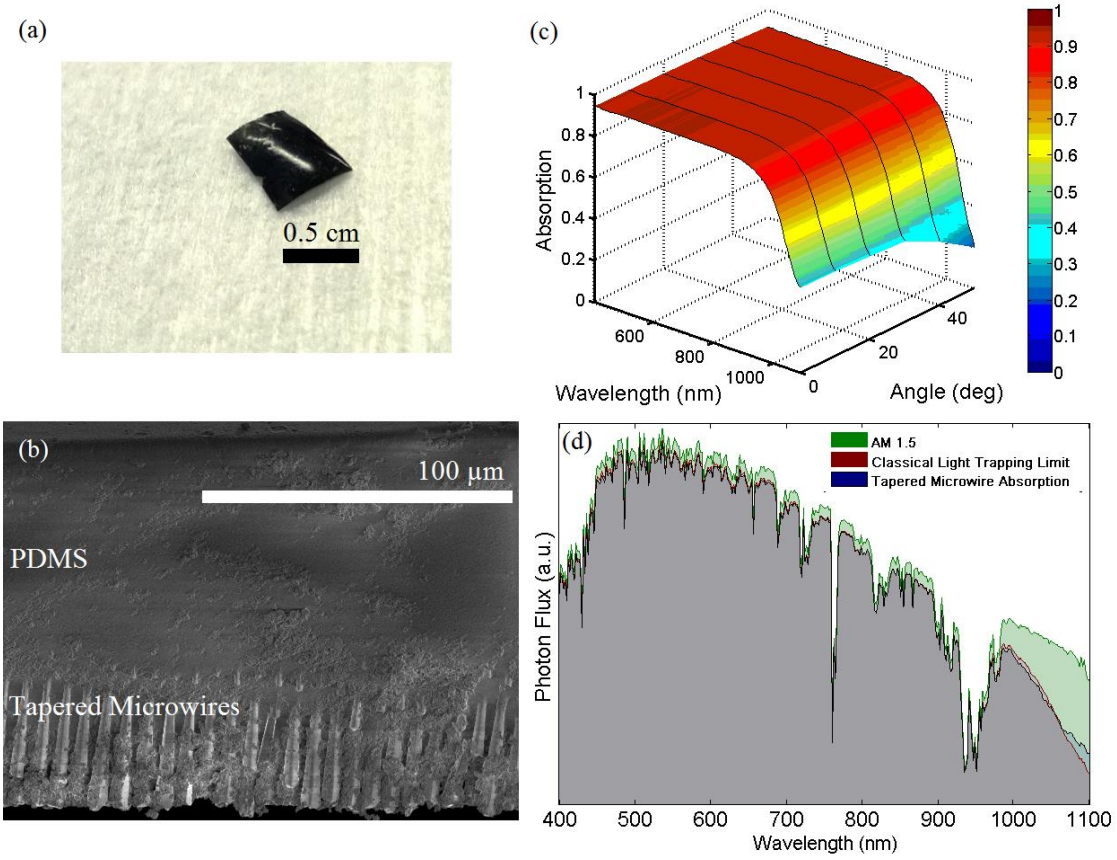

Figure 3.5*: (a) Optical photograph of the films with microcones embedded in PDMS, (b) cross section SEM of the film, (c) absorption measured in the film in the range 400nm – 1100nm while varying the angle of incidence from 0^0 to 50^o, and (d) semitransparent area plot for comparison of absorbed photon flux at normal incidence with classical light trapping limit absorption of a 20 µm thick slab*

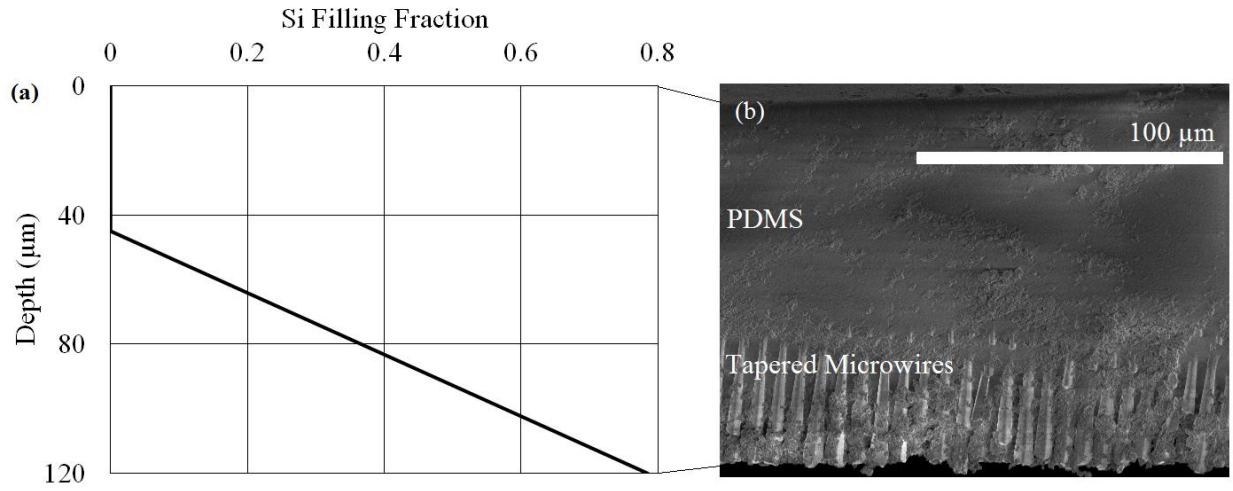

***Figure 3.6**: (a) Si fill fraction variation from the top of the peeled off PDMS films with tapered microwires embedded in it. (b) SEM cross section image of the films showing the tapered microwires popping out of PDMS at the bottom of the film.*

3.4 Wave Optic Simulations

The exceptionally low reflectivity of the arrays arises from the conical geometry. The fill fraction of the arrays at the light-incident interface is less than 0.01% and linearly increases extremely gradually along the extended length of the microcones to ~78% at their base. The remarkable optical characteristics – minimal reflection and high absorption-- of the Si microcone arrays cannot be completely explained by either effective medium concept or ray optic analysis especially at wavelengths near band gap of Si, and requires a wave-optical analysis for quantification. A previous theoretical study of Si microwire optical properties indicated that ray optical models are insufficient to explain the strong absorption observed experimentally in microwires with radii smaller than 4 μm. The microcones in this study have radii ranging from 50 nm to 3.5 μm. Therefore, we employed full wave simulations to accurately model the optical properties of the fabricated microcones [58].

From this, the measured absorption is seen in this case to arise from efficient coupling of incident light into waveguide modes in the cones. We employed a combination of full wave electromagnetic simulations and analytic waveguide analysis to develop an understanding of the array optical properties. The strong symmetry overlap of specific waveguide modes also contributes to the low reflectivity, and is discussed in more detail below. Bloch modes, which often result in reflection

bands,[59],[60],[61] play an insignificant role in these structures due to an inter cone spacing that is much larger than the optical wavelength. Consequently, each microcone acts as an independent optical antenna and waveguide, consistent with previous findings [62],[63],[64].

The high absorption arises from a combination of coupling into waveguide modes and the length of the microcones. Many groups have studied and demonstrated enhanced absorption in Si nanowire arrays due to coupling into waveguide modes with large extinction cross sections.[65],[66],[67],[68],[69] Owing to nanofabrication-imposed limitations to the achievable nanowire aspect ratio, the Si nanowire array absorption is typically much lower than that for optically thick planar Si absorbers, despite field enhancements due to the material volume required to achieve near-unity absorption in indirect bandgap materials [70]. Our microcone structures also capitalize on waveguide modes for optical absorption enhancement, while simultaneously incorporating long optical path lengths to achieve near-unity absorption. Efficient coupling into the optical waveguide modes of the Si microcone is the critical factor in the remarkable optical properties of these arrays.

Three-dimensional full field electromagnetic wave simulations of microcone arrays were performed to characterize the waveguide modes. Rigorous 3D full field electromagnetic wave FDTD simulations of microcone arrays were performed using a commercial software package, Lumerical FDTD. The arrays were constructed using the 3D rectangular simulation region with periodic boundary conditions along x and y axes to depict 7 μm square lattice of the arrays, and infinite boundary conditions rendered as perfectly matched layers (PML) along z axis. In the simulation region microcones had a top diameter of 50 nm, bottom diameter of 7 μm, and height of 75 μm. Palik material data provided by Lumerical was used for modelling the material as Si. Single wavelength infinite plane wave sources at four different wavelengths (400 nm, 600 nm, 800 nm, and 1000 nm) were used with a long pulse time of 50 fs to simulate steady state behavior. Generation rate in these structures was calculated by using the built in CW-generation (continuous wave generation) rate analysis group to obtain electron hole pair generation profiles under steady state illumination. Figure 3.7 displays carrier generation cross-sections for microcones at incident wavelengths of 400, 600, 800, and 1000 nm, respectively. Figure 3.7 (e)-(h) show complete cone cross sections on a logarithmic scale, marked with light blue squares indicating the bounds of Figure 3.7 (a)-(d), which focus on the upper portion of the cone and are shown in linear scale.

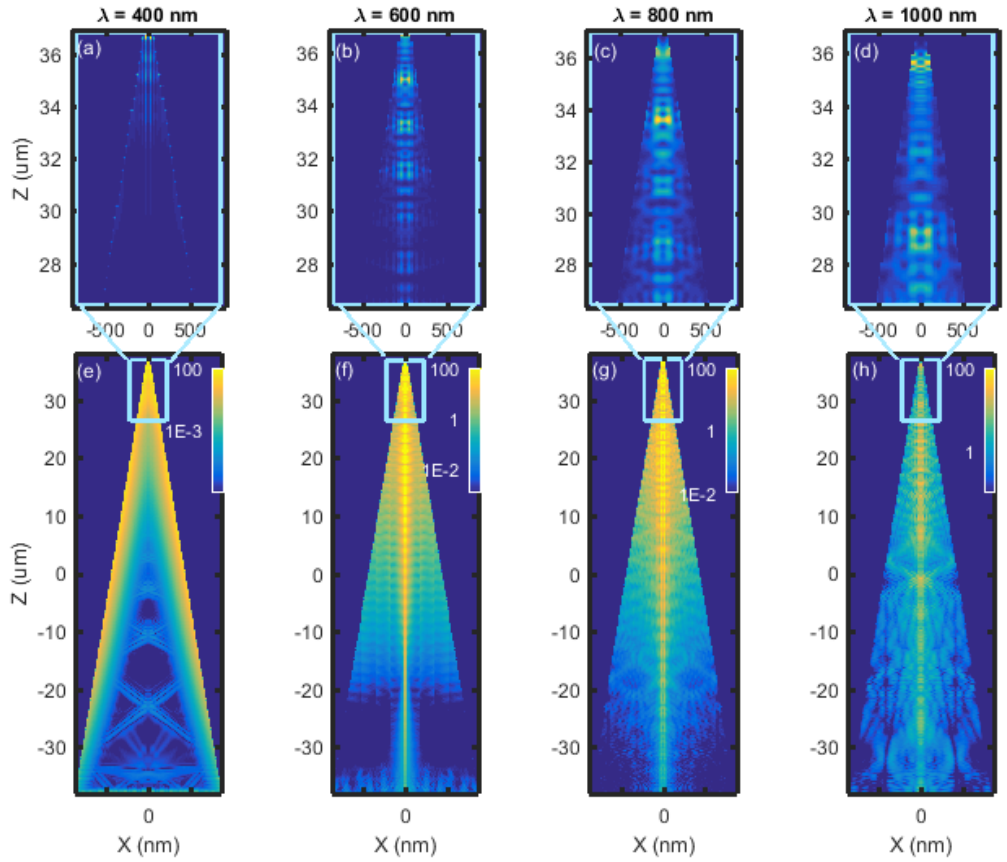

Figure 3.7*: Longitudinal cross sections of power absorption for Si microcones at 400 (a,e), 600 (b,f), 800 (c,g), and 1000 (d,h) nm wavelengths, respectively; (a-d) upper portion of microcone with linear intensity scale; (e-h) complete microcone with logarithmic intensity scale; light blue squares correspond to expanded cross sections in (a-d); different relative scales are used for each figure to highlight modes.*

All absorption profiles indicate light coupling into waveguide modes, but the modes are less obvious at λ = 400 nm (Figure 3.7 (a) and (e)), due to strong absorption above the direct gap of Si. Below the direct gap of Si, the waveguide characteristics become more apparent. Absorption occurs primarily in the microcone core, indicative of guided mode propagation in the cone, and exhibits semi-periodic longitudinal intensity oscillations that scale with incident wavelength; these longitudinal oscillations in field intensity are not representative of any longitudinal interference modes, but rather are indicative of the phase cycle of mode propagation. This distinction is critical because longitudinal interference modes would require long solar coherence lengths, whereas mode propagation does not.

Additionally, the existence of significant intensity near the lower end of the microcone in the λ = 1000 nm profile demonstrates long distance waveguide mode propagation to the bottom of the microcone, enabling near-unity absorption for wavelengths near the Si band edge. Simulations show that the reflection is < 1 % at wavelengths below 1000 nm agreeing with the measurements. Since carrier generation was observed to occur predominantly in the upper portion of the cones, the minor deviation from perfectly circular cone shape seen in Figure 3.2 at the base of the cones is not expected to give rise to a significant change in the optical properties relative to the circular cross sections assumed in our simulations.

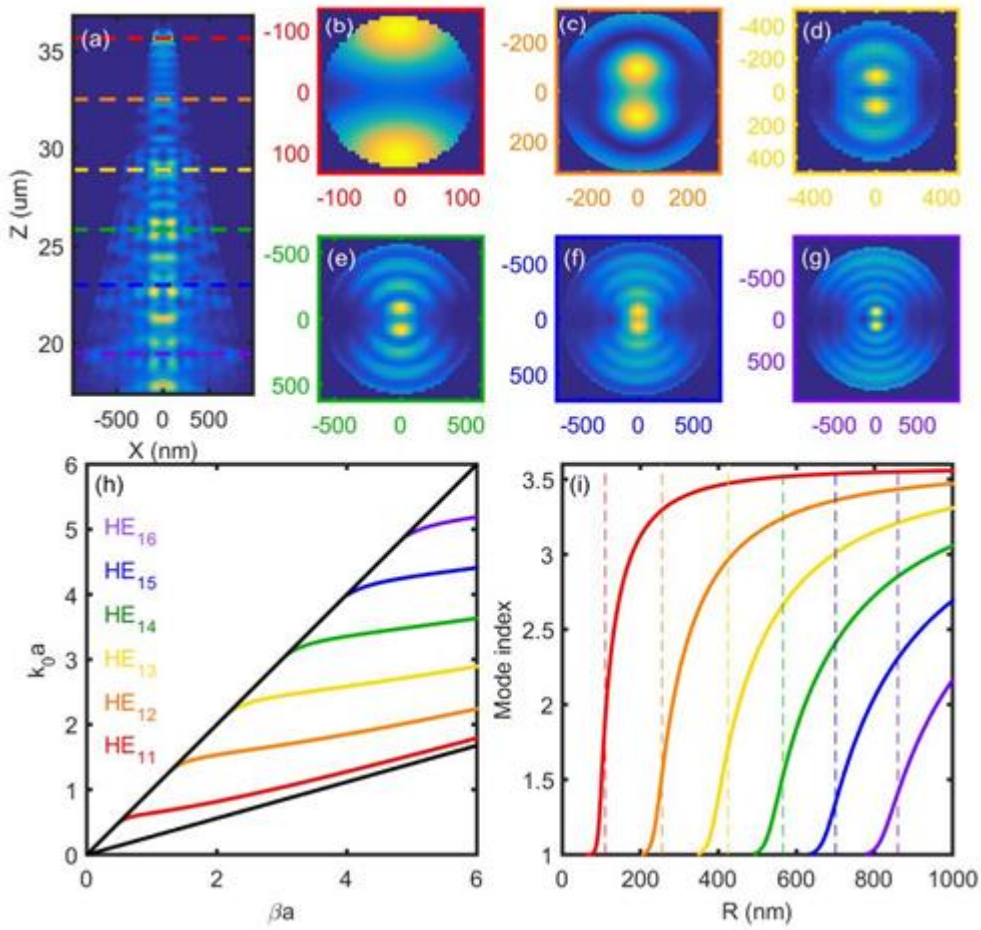

***Figure 3.8**: Detailed mode analysis of upper portion of a microcone at λ = 1000 nm; mode color key in (h) is applied throughout the figure; (a) longitudinal absorption cross section with dashed lines indicating radial cross sections; (b-g) radial cross section, exhibiting HE_{1n} modes; (h) traditional dispersion curves for HE_{1n} modes for n=3.577; (i) non-traditional dispersion curves, converted from (h) for λ = 1000nm.*

Detailed mode analysis reveals that light couples into the set of first azimuthal order waveguide modes, HE_{1n}, as illustrated for λ = 1000 nm illumination in Figure 3.8. As previously reported,[71],[72] efficient coupling occurs into this set of modes due to the strong overlap in symmetry between the incident plane wave and the in-plane mode field profiles. Figure 3.8 (a) displays a longitudinal cross section marked with horizontal dashed lines colored to indicate their correlation with the radial cross sections in Figure 3.8 (b)-(g); the radial cross sections correspond to the first six HE_{1n} modes, in ascending order. As expected, the first order HE_{11} mode appears at the top of the wire, and the higher order modes appear in sequence, as radius increases.

$$\left(\frac{1}{k_{cyl}^2}-\frac{1}{k_{out}^2}\right)^2\left(\frac{\beta m}{k_0 a}\right)^2=\left(\frac{\varepsilon_{r,cyl}\mu_{r,cyl}}{k_{cyl}}\frac{J_m'\left(k_{cyl}a\right)}{J_m\left(k_{cyl}a\right)}-\frac{\varepsilon_{r,out}\mu_{r,out}}{k_{out}}\frac{H_m'\left(k_{out}a\right)}{H_m\left(k_{out}a\right)}\right)\left(\frac{1}{k_{cyl}}\frac{J_m'\left(k_{cyl}a\right)}{J_m\left(k_{cyl}a\right)}-\frac{1}{k_{out}}\frac{H_m'\left(k_{out}a\right)}{H_m\left(k_{out}a\right)}\right) \quad (1)$$

The dispersion curves for these modes were calculated from the eigenvalue equation (Eqn. 1) for cylindrical dielectric waveguides,[73] where J_m and H_m are the cylindrical Bessel and Hankel functions of the mth order, k_0 is the free space wavevector, k_{cyl}(k_{out}) is the transverse wavevector inside(outside) the cylinder, β is the mode propagation constant, $\varepsilon_{r,cyl}$ ($\varepsilon_{r,out}$) and $\mu_{r,cyl}$($\mu_{r,out}$) are the relative dielectric permittivity and permeability inside(outside) the cylinder, and a is the cylinder radius. Figure 3.8 (h) and Figure 3.8 (i) show the dispersion curve for a Si waveguide (n=3.577), in its tradition form, k_0a(βa), and a non-traditional form, mode index vs. radius, respectively. The mode color key in Figure 3.8 (h) is consistent throughout the figure. The dashed lines on Figure 3.8 (i) indicate the radius of the mode cross sections in Figure 3.8 (b)-(g), revealing that the modes are most prominent between a mode index of 1 and 2. This moderate mode index is due to a tradeoff between ease of free space coupling and mode confinement mediated-absorption. Mode profiles, propagation constants and radius range are all consistent with analytic waveguide theory. These observations demonstrate the critical role of waveguide modes in the optical characteristics of the microcone arrays.

3.5 Photogenerated Carrier Lifetime Measurements

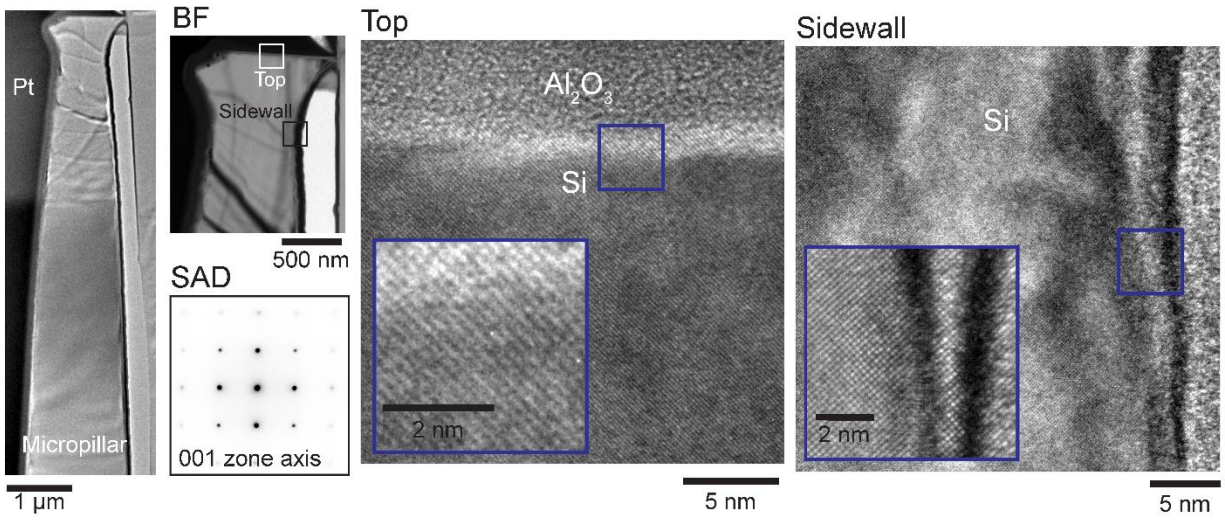

***Figure 3.9**: Transmission electron microscopy (TEM) study of a single etched microwire immediately after ICPRIE with the Al_2O_3 mask intact on top and with no cleaning except a solvent rinse is aligned to the 001 zone axis. A large area corresponding to the tip of a cone was studied (far left). Bright field images (BF) are devoid of contrast within the etched wire other than bend contours introduced during sample preparation, and selected area diffraction (SAD) shows a clean pattern. Higher resolution images at the top of the cone (center) shows no evidence of damage to the cone tip which was protected by the hard mask during growth. However, a high resolution imaging reveals a thin (~ 2-3 nm) region on the sidewalls (far right) which could correspond to damage introduced during the etching process. These data were collected at 300 kV in an FEI Technai TF30 TEM.*

In order to evaluate quality of etched microcones/microwires and estimate the maximum achievable V_{oc}, transmission electron microscopy (TEM) and lifetime measurements were performed. Etched microwires were removed from the host Si wafer by mechanical cleaving with a razor blade before being dispersed in isopropyl alcohol. The resulting solution was spun onto a Si wafer for 30 s at 2000 rpm. The wire-coated wafer was then coated with ~ 20 nm of Al_2O_3 with atomic layer deposition. Axial cross sections were made in a FEI Versa dual-beam focused ion beam instrument, extracted with an FEI EasyLift NanoManipulator and welded to an Omniprobe Cu liftout TEM grid before

thinning to electron transparency. Electron microscopy images of the sidewall shown in the Figure 3.9 shows minimal surface damage due to etching, and no lattice damage in the bulk, as expected from the low forward power (5W) and predominantly chemical nature of the dry etching process.

In order to estimate the recombination at the surface of etched microwires, cylinders of 3, 15 μm diameters and height 50, 70 μm respectively were etched by ICPRIE in high lifetime (~1 ms) intrinsic Si wafers. Standard RCA 1 and RCA 2 clean processes followed by 20s damage removal in 5.4M KOH solution at around 70^{o}C were performed on the etched samples. Microwires from these substrates were scraped off their substrates with a razor blade and were collected in a centrifuge tube. A further 10s etch in 3.6M KOH solution at room temperature is performed on these microwires to remove the back surface damage due to scraping, before neutralizing the etching solution to stop etching by addition of concentrated 5.8M HCl. The microwires were separated from the resulting solution by centrifuging the solution. The wires were rinsed three times in DI water to get rid of the solution. Various liquid passivation mechanisms including 3.6M HCl solution, 31.8M HF, 1.3M HF, and Iodine in Ethanol were added to the cleaned wires. Lifetime measurements of these wires were performed by a home built microwave detected photoconductivity decay (MW-PCD) tool with Nd:YaG laser illumination at 1064 nm as shown in Figure 2.10. Laser power was varied between 30-120 μJ. Pulse width of 5 ns and spot size of 3 mm diameter was used at 50 Hz frequency during measurements.

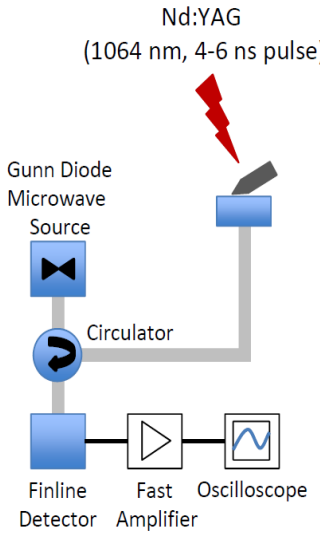

***Figure 3.10**: Schematic of home built microwave detected photoconductivity decay setup*

While it is most informative to measure the lifetime at different, known injection levels, it is difficult to know the exact injection level in this configuration. 1064 nm is weakly absorbing in silicon, and therefore significant attenuation in intensity is not expected as light is absorbed. It is likely that some distribution of injection levels exist due to their varying optical environments. The injection level, and therefore the most relevant recombination mechanism can be estimated by measuring the change in lifetime as a function of laser intensity. All samples showed an increase in lifetime as pulse energy was increased from 30 μJ to 120 μJ, characteristic of transition from low level injection to high level injection [74].

Table 3.1 compares the various surface passivation mechanisms under which the carrier lifetimes were measured in 15 μm diameter, and 70 μm long silicon microwires at a laser pulse energy of 240 μJ. Under 3.6 M HCl passivation a lifetime of 1.9 μs was measured in these microwires. Similar measurement for 3 μm diameter, and 50 μm long microwires measured carrier lifetimes of 0.67 μs. HCl is known to remove metallic impurities from silicon and therefore is used in processes such as RCA 2 cleaning. Therefore we hypothesize that HCl does a better job of removing the metallic impurities that contaminate the silicon microwires during the scraping off process using a metallic razor blade. Table 3.2 shows the estimated carrier lifetimes in the 3 μm and 15 μm diameter microwires under various surface recombination velocities assuming a bulk lifetime of 1 ms under low level injection conditions calculated from Synopsis Sentaurus TCAD simulations. The carrier lifetimes measured indicated that the surface recombination velocities at the surfaces were of the order of few hundreds of cm/s.

Passivation Mechanism	Carrier Lifetime (μs)
Iodine in Ethanol	0.6
1.3 M HF	0.4
31.8 M HF	0.7
3.6 M HCl	1.9

***Table 3.1** : Carrier lifetimes measured under various surface treatments*

Wire Geometry: Diameter (d μm) Height (h μm)	SRV (cm s^{-1})	Calculated Lifetime (μs)
d = 3 h = 50	50	4
	100	1.5
	500	0.75
d = 15 h = 70	20	16.5
	100	6
	500	1.5

Table 3.2*: Estimated lifetimes based on SRVs*

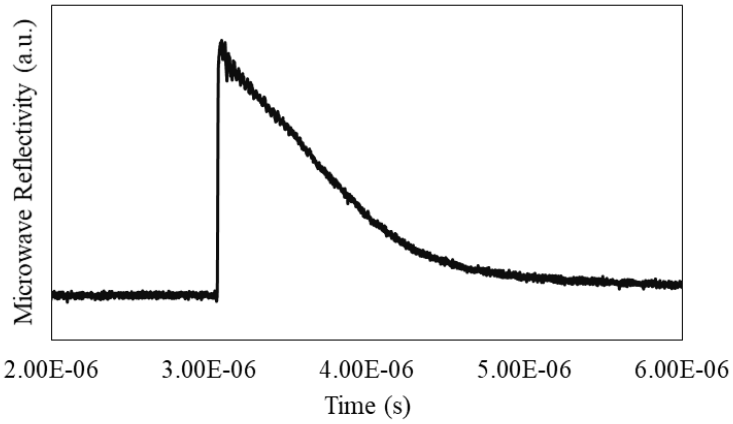

Figure 3.11*:Microwave reflectivity of ALD Al_2O_3 passivated microcone arrays with in situ back surface passivation using 5.8M HCl measured using the microwave photoconductivity setup with 0.75 μs carrier lifetime*

The carrier recombination lifetimes were measured for microcone arrays passivated by Al_2O_3 coated-by atomic layer deposition (ALD) [37, 75]. Al_2O_3 was deposition on Si by atomic layer deposition using Trimethylaluminum and water as precursors at 150^{o}C after standard cleaning procedure. The precursors were pulsed for 15 ms at 20 s intervals for 200 cycles. The Si samples then annealed at 400^{o}C for 10 minutes under nitrogen flow of 3 lpm. Al_2O_3 passivated tapered microwire arrays were embedded in PDMS and peeled from their respective substrates using a razor blade. During the measurements, the fractured back surfaces of the peeled microwires were passivated *in situ* using 5.8M HCl, after a 20s damage removal etch in 3.6M KOH at room temperature. All the lifetime measurements resulted in continuously increasing lifetimes as a function of intensity, indicating that

measurements were done at the onset of high injection level [76]. Lifetimes of 0.75 µs were measured in these arrays with 240 µJ pulses as shown in Figure 3.11.

An analytical model was implemented to estimate surface recombination velocity (SRV), implied V_{oc}, and the corresponding maximum limiting efficiency achievable from the carrier lifetime measurements. The model was implemented in Microsoft Excel, using VBA to iteratively solve the transcendental equations for steady state carrier concentration. Equivalent planar thickness, surface area, total absorption, surface recombination velocity, radiative recombination coefficient, Shockley-Reed-Hall coefficients [77], and auger recombination coefficients[78] in the bulk were input parameters. This model gives the absolute theoretical maximum limiting V_{oc}, and efficiency that can be achieved in principle from the microcone light trapping structures with the measured lifetimes. The average steady state excess carrier concentration was obtained by solving for equivalence of the total generation rate and sum of all recombination rates due to the four recombination mechanisms considered. In this model we ignored the effects of resistances and assumed a narrow selective contact, therefore the change in quasi fermi levels in the bulk of Si is very small. The quasi fermi level separation and maximum V_{oc} achievable are obtained from equation 2. To estimate the total carrier generation, an internal quantum efficiency of 100 % was assumed, and the total photon flux absorbed was calculated from the measured absorption in tapered microwire arrays under AM 1.5 spectrum. Because the etching process was predominantly chemical and no bulk damage was observed in TEM analysis, the bulk lifetime was assumed to be 1 ms (same as the lifetime measured in the starting wafer in which the structures were etched into). Finally, an efficiency was extracted using the total generation as the J_{sc} and calculating a fill factor using the empirical model for a device without series resistance or shunting developed by M.A. Green [79]. In this model an intrinsic doping density (n_i) of 9.7 x 10^9 cm^{-3}, donor doping density (N_d) of 10^{17} cm^{-3}, and radiative recombination coefficient (B_{rad}) of 4.7 x 10^{15} cm^3s^{-1} were used. This model provides an estimate for the absolute maximum achievable efficiency. In realistic photovoltaic devices, resistances are expected to reduce the efficiencies relative to those calculated via this model.

$$V_{OC} = E_{fn} - E_{fp} = \frac{kT}{q}\ln\left(\frac{(N_A + \Delta n)\Delta n}{n_i^2}\right) \qquad (2)$$

The SRV achieved was estimated to be 150 cm s^{-1}, with the corresponding implied V_{oc} to be 0.655 V, and the maximum efficiency achievable to be 22.2 %. The microcone arrays are surface

recombination limited and a further decrease in SRV to 5 cm s^{-1} is shown to enhance the lifetime to > 15 μs, and the maximum limiting efficiency to > 25%.

3.6 Conclusion

In conclusion, the microcone arrays fabricated in this work demonstrate superior light trapping properties with < 1 % angular averaged reflection, and absorption reaching the $4n^2$ light trapping limit due to enhanced coupling of incident light into the waveguide modes. The high absorption arises from a combination of coupling into waveguide modes and overall length of the microcones, resulting in absorption that approaches to the ray optic light trapping limit over most of the solar spectrum and absorption above the ray optic limit at wavelengths near the Si energy band gap [80]·[81]. These microcones show no bulk damage and minimal surface damage that can be removed by surface cleaning after fabrication. We measured carrier lifetime in these microstructures by microwave detected photoconductivity measurement, and measured lifetimes of 0.75 μs for wires under ALD deposited 20 nm thick Al_2O_3 sidewall passivation with 5.8 M HCl back surface passivation. In this work the performance of the arrays is limited by surface recombination and therefore further improvement in surface passivation methods to these arrays can push the performance of these arrays to reach V_{oc} > 0.7 V and maximum possible efficiency > 25%. The efficiencies estimated by our model provide the absolute maximum possible limiting value that are in principle achievable given the material volume and surface area of the fabricated structure and the observed optical properties. The real world device architectures we envision utilizing these microcone arrays include all back contact solar cells[37, 43, 75, 82] similar to previous demonstrations with an ultrathin Si substrate [83] or as a flexible solar cell with a conventional back contact and a transparent front contact [56], the effect of resistances in the structures and selective contacts are expected to reduce the estimated efficiency further. In this study, ICPRIE was chosen as the fabrication technique because it offers significant optoelectronic performance advantages--the electronic quality of the bulk wafer is preserved, and the fine control over the shape of etched structures enables optimal optical design. Due to the high surface area and superior light trapping these microcones are also excellent candidates for applications in photoelectrochemical cells and enhancing electrode efficiencies [84-88].

Chapter 4

Photoelectrochemical Profiling Photoinduced Carrier Generation in Silicon Microwires

4.1 Introduction

Semiconductor mesostructures have been studied extensively due to their unique band gap energies, absorption and reflectance properties, charge-transport pathways, and increased surface area, relative to their planar counterparts.[89-92] The ability to tailor such properties has made mesostructures attractive architectures for applications in areas including photonics[93-95], photovoltaics[96-99], electronics[100, 101], catalysis[102-104], and sensing[105, 106]. Mesostructured semiconducting wire arrays composed of elemental, binary compounds (e.g. group III-V, II-VI, IV-VI) and ternary compounds have been synthesized.[92, 107-114] The macroscopic optoelectronic and electrochemical properties of such wire arrays have been experimentally characterized[115-119], but nanoscale analyses that aim to provide a microscopic understanding of these properties have been mostly limited to theoretical and computational methodologies.[120-123]

The optical excitation of photoactive semiconductor substrates immersed in a metal-ion solution can provide the driving force for deposition of a metal.[124] Photoelectrochemical metal deposition has been used to generate arbitrarily patterned metallic deposits on a semiconductor surface by use of a photomask or by use of scanning laser illumination.[125-129] The localized illumination results in the spatially confined generation of mobile charge-carriers that are transported toward the solid/solution interface, and subsequently drive localized electrochemical deposition. Herein, we demonstrate the use of such a photoelectrochemical deposition process to physically record the localization of carrier generation in three-dimensional semiconductor mesostructures under conformal illumination. Unlike planar materials, such structures display significant, inherent spatially anisotropic and complex, light absorption in three dimensions.[122, 123] Si microwire arrays can be grown with a high degree of fidelity and control; provide superior optical absorbance

on a per unit mass basis than planar Si; and have shown potential for use in photovoltaic, fuel-forming photoelectrochemical, and sensing applications.[88, 130-133] In this work, Au was photoelectrodeposited onto arrays of cylindrical or tapered Si microwires, using a series of narrowband light sources providing excitation at a variety of wavelengths. The localization of the Au deposition was examined by scanning-electron microscopy (SEM). Computer modeling of carrier generation in the same structures was performed to correlate the localization of the deposition with the expected spatial distribution of the carrier generation in the material.

4.2 Experimental Procedure

S1813 positive photoresist was spin coated at 4000 rpm onto the top of Si wafers. The wafers were then heated on a hotplate at 115 ºC for 1 min. The photoresist was then exposed using UV illumination through a square lattice mask consisting of holes with a 3 μm diameter and a 7 μm pitch. The photoresist was developed using MF-319 developer and the wafers were baked for 10 min at 115 ºC. A 200 nm thick Al_2O_3 mask was then deposited onto the patterned wafer using electron-beam evaporation. PG-remover was used to liftoff the photoresist. After the liftoff, Fomblin oil was applied to the back of the wafers to act as a thermal contact material, and the wafers were loaded into the etching chamber. Wires were etched using a cryogenic inductively coupled plasma reactive ion etching process (ICP-RIE) with an Oxford DRIE 100 ICP-RIE system. Etching was performed at low capacitive coupled power of 5 W to reduce damage due to the momentum of the ions. A high inductively coupled power of 900 W was used to increase the number of ions in the plasma to achieve high rates of chemical etching. The chamber was maintained at -120 ºC and a pressure of 10 mTorr during the etching process. Etching was performed using SF_6 : O_2 ratios ranging from 70 sccm : 5.5 sccm to 70 sccm : 8 sccm for 30 min. Variation of the O_2 concentration in the plasma enabled control over the wire taper. After etching, the wafers were dipped in buffered HF to chemically remove the Al_2O_3 mask.

Si microwire arrays were cut into ~ 1 cm x 1 cm sections. Immediately before deposition, each section was rinsed with CH_3OH, followed by H_2O, and then immersed in buffered HF(aq) for ~ 60 s to remove any surficial SiO_x from the Si. The sample was then rinsed with H_2O and dried with a stream of N_2(g). A Ga/In eutectic was scratched into the back side of each section using a carbide

scribe, and the section was mounted on a ~ 2 cm x 2 cm Ti plate using Cu tape. This assembly was then sealed with a Ti backplate into a single compartment O-ring compression that confined the contact region between the solution and the Si microwire array section to a circular area of 0.1 cm^2. The cell was equipped with a pyrex window to enable illumination during deposition. A three-electrode configuration was utilized with a graphite-rod counter electrode (99.999 %, Sigma-Aldrich) and a Ag/AgCl reference electrode (3 M KCl, Bioanalytical Systems). Au was deposited from an aqueous solution of 0.010 M $HAuCl_4$ and 0.100 M KCl. All depositions were performed using a Princeton Applied Research Model 273 potentiostat. Depositions were carried out at room temperature by biasing the illuminated microwire array potentiostatically at -1.25 V vs. Ag/AgCl until an integrated charge density of 0.10 mC cm^{-2} had been passed. The linear sweep voltammogram in Figure 3.1 for p-type Si microwires shows that at -1.25 V the photocurrent is > 4 times the dark current.

Illumination for the photoelectrochemical depositions was provided by narrowband diode (LED) sources (Thorlabs) with respective intensity-weighted λ_{avg} values and spectral bandwidths (FWHM) of 461 and 29 nm (M470L2), 516 and 30 nm (M505L3), 630 and 18 nm (M625L3), and 940 and 30 nm (M940L2), respectively. The output of each diode source was collected and collimated with an aspheric condenser lens (Ø30 mm, f = 26.5 mm). The light intensity incident on the electrode was measured by placing a calibrated Si photodiode (Thorlabs FDS10X10), in the photoelectrochemical cell with the electrolyte, at the location of the electrode, and measuring the steady-state current response of the Si photodiode. Depositions that utilized the diode with λ_{avg} = 461 nm as the illumination source were performed with a light intensity of 77 mW cm^{-2} at the electrode. Depositions using the diodes with λ_{avg} = 516, 630, and 940 nm, were performed with intensities of 64, 50, and 33 mW cm^{-2}, respectively. Scanning-electron micrographs (SEMs) were obtained with a FEI Nova NanoSEM 450 at an accelerating voltage of 5.00 kV and working distance of 5.00 mm using an Everhart-Thornley secondary electron detector.

Photocarrier generation profiles in Si wire arrays under steady-state illumination with unpolarized light were simulated using three-dimensional full wave electromagnetic simulations via a finite-difference time domain (FDTD) method. Modeling was performed using the FDTD Solutions software package (Lumerical). Si microwire arrays were simulated using a single three-dimensional unit cell with periodic boundary conditions along the x and y axes to depict a 7 μm square lattice

similar to the fabricated arrays, in conjunction with infinite boundary conditions rendered as perfectly matched layers (PML) along the z axis. Idealized microwire arrays corresponding to the four different fabricated shapes were constructed in the 3D simulation region by approximating the tapered microwires as truncated cones or multiple sections of truncated cones. The absorption was simulated under polarized illumination and then the CW-generation rate analysis group in the FDTD Solutions software was used to derive the generation rate per unit volume. The generation rate under unpolarized illumination was obtained by averaging the generation rate data with itself by interchanging the x- and y-axes as permitted by the square symmetry of the wire lattice.

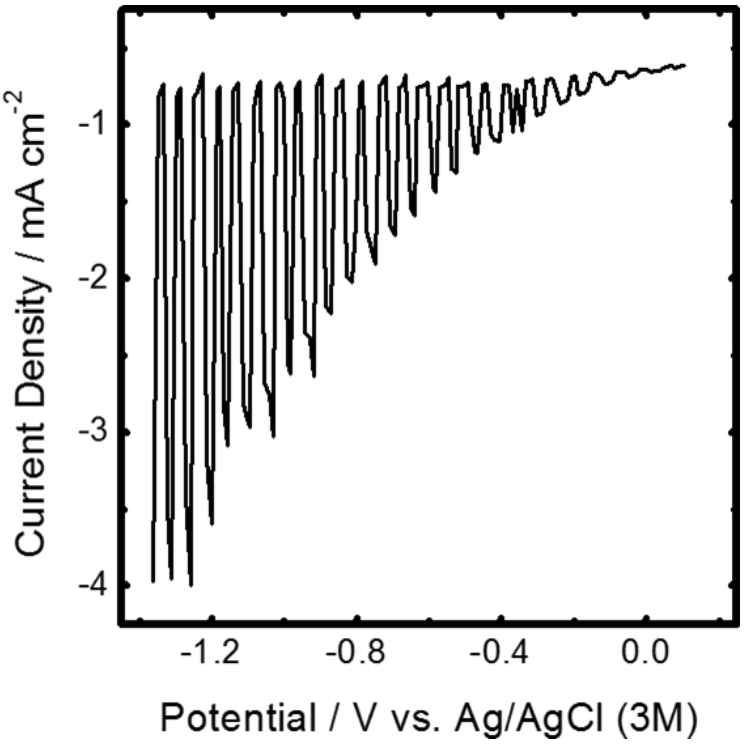

***Figure 4.1**: Linear sweep voltammogram (at a scan rate of 50 mV s^{-1}) obtained with a p-Si microwire array with a ~ 3 µm wire diameter, 7 µm wire pitch, and 30 µm wire height in an aqueous solution of 0.010 M $HAuCl_4$ and 0.100 M KCl under chopped illumination with a LED source having λ_{avg} = 461 nm and an intensity of 77 mW cm^{-2}.*

4.3 Photoelectochemical Deposition Profiles

Figure 4.2 (a) presents a cross-sectional scanning-electron micrograph (SEM) of a Si microwire array onto which Au was photoelectrodeposited using a LED with an intensity-weighted average wavelength, λ_{avg}, of 461 nm. The Au plating was radially symmetric, but enhanced deposition was observed at the tips of the wires, with the deposition diminishing rapidly along the axial dimension. Figures 4.2 (b)-(d) present analogous SEMs for depositions using LEDs having λ_{avg} values of 516, 630, and 940 nm, respectively. Increasing λ_{avg} decreased the axial deposition gradient, with conformal deposition being approached for λ_{avg} = 940 nm. In contrast, deposition of Au proceeded conformally onto n-type Si microwire arrays that had nominally equivalent morphologies to the p-type Si microwire arrays.

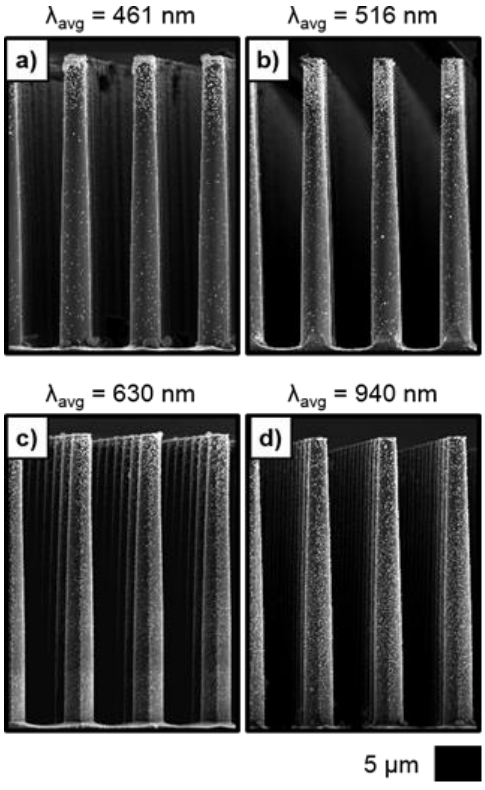

Figure 4.2*: (a−d) Representative SEMs of p-Si microwire arrays with a ~ 3 µm wire diameter, 7 µm wire pitch, and 30 µm wire height in a square lattice, upon which Au was photoelectrodeposited from a HAuCl4 solution with a charge density of 0.10 C cm-2 using narrow band LED illumination having λ_{avg} as indicated.*

Figure 4.3 (a)-(d) present representative cross-sectional SEMs of n-type arrays analogous to those presented for the p-type arrays in Figure 4.2 (a)-(d). Such behavior supports a notion that the anisotropic deposition observed on the p-type Si microwire arrays is directed by light absorption and photocarrier generation and transport, as opposed to solution-based transport limitations in the void volume of the Si microwire array. Electrodeposition at a p-type semiconductor interface using a sufficiently cathodic bias at room temperature without illumination is ineffective due to a scarcity of mobile electrons (minority carriers) in the material. Light absorption in p-type materials results in the generation of mobile electrons which can approach the interface and drive electrochemical reduction of a solution species. Thus, anisotropic light absorption may result in anisotropic deposition at the interface of a p-type material. In contrast, similar cathodic deposition at an n-type semiconductor interface does not require illumination to proceed at significant rates due to the presence of mobile electrons (majority carriers) in the material.

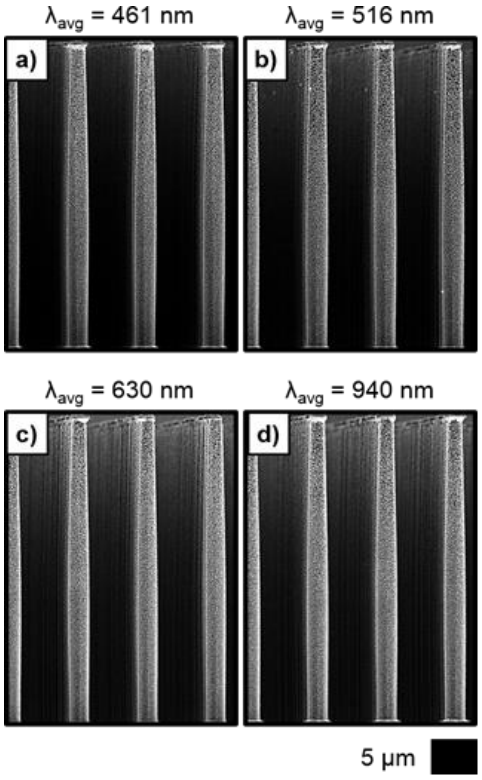

Figure 4.3*: (a−d) Representative SEMs of n-Si microwire arrays with with ~ 3 μm wire diameter, 7 μm wire pitch, and 30 μm wire height in a square lattice, upon which Au was photoelectrodeposited from a* $HAuCl_4$ *solution with a charge density of 0.10 C* cm^{-2} *using narrowband LED illumination having* λ_{avg} *as indicated.*

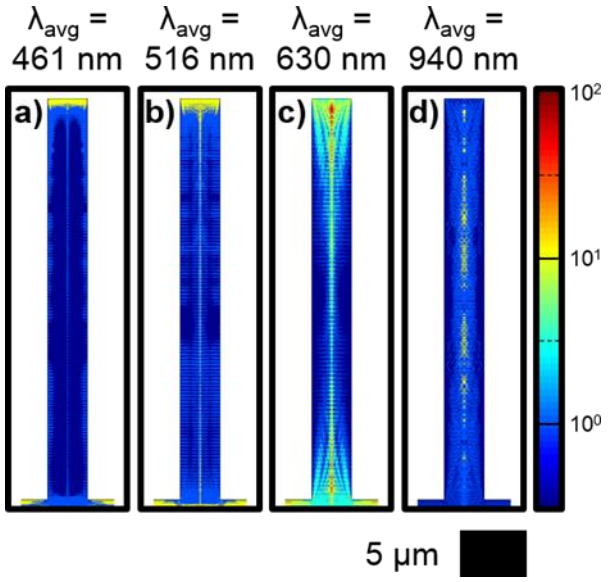

Figure 4.4*: (a−d) Simulated relative photocarrier generation rates in Si microwires with a 3 µm wire diameter and 30 µm wire height in a square lattice with a 7 µm wire pitch under narrowband illumination with spectral profiles having λavg as indicated.*

Figure 4.4 (a) depicts a two-dimensional representation (side-view) of the simulated photocarrier generation rates in a microwire under simulated illumination with λ_{avg} = 461 nm. The simulated generation in a well-defined, narrow region near the tip of the wire was at least an order of magnitude higher than in any other volume of the wire, including that directly below in the axial dimension. The photoelectrodeposition of Au at this wavelength (Figure 4.2 (a)) mirrored this localization in that the majority of the Au plated near the tip of the wire. Figure 4.4 (b)-(d) display representations of the photocarrier generation rates analogous to that presented in Figure 4.4 (a) but with values of λ_{avg} of 516, 630, and 940 nm, respectively. At these longer wavelengths, the carrier generation profiles displayed waveguide characteristics that are more readily apparent than for λ_{avg} = 461 nm, due to the high Si absorption coefficient at this wavelength. Waveguide behavior was observed despite micron-scale wire dimensions, consistent with previous reports on semiconductor nanowire absorption.[89, 134] For λ_{avg} = 516 nm, as with λ_{avg} = 461 nm, generation near the tip of the wire was generally at least an order of magnitude higher than at other axial locations in the microwire. For λ_{avg} = 516 nm, the region of high generation near the tip was thicker, and generation throughout the rest of the volume was mostly equivalent or higher, than the profile calculated for λ_{avg} = 461 nm. The localization of carrier generation for λ_{avg} = 516 nm was also similar to that observed experimentally for Au photoelectrodeposition, as shown in Figure 4.2 (b), where the plating was

concentrated axially in a region near the tip of the wire, but with diminished axial anisotropy relative to the deposition under λ_{avg} = 461 nm illumination. For λ_{avg} = 630 nm, the carrier generation profile was significantly more isotropic than for the shorter wavelength cases. However, the total generation in the ~ 5 μm axial sections at the top and bottom of the wire was greater than that in the center of the wire. This calculated generation profile matched the photoelectrodeposition profile observed experimentally (Figure 4.2 (c)), wherein significant Au plating was observed along the entire length of the wires, but with somewhat greater density at the tops and bottoms. For λ_{avg} = 940 nm, the calculated carrier generation was more uniform in the axial dimension than for λ_{avg} = 630 nm. The total generation was somewhat lower in the top and bottom ~ 5 μm of the wire relative to the generation in the center. The Au plating (Figure 4.2 (d)) mirrored this observation, with generally conformal deposition that was nevertheless lower at the very top and bottom relative to the center. Thus, the localization of photocarrier generation consistently matched the localization of the photoelectrodeposited Au, indicating that the cathodic metal plating is directed by carrier generation in the p-type material under the conditions utilized in this work. Such a phenomenon indicates that the micrographs of the metal deposition provide a spatially resolved image of the relative photocarrier-generation rates in structured semiconductors, provided that carrier transport occurs over sufficiently short distances to maintain the integrity of the linkage between the locations of volumetric carrier generation and the minority-carrier flux that produces surface-based metal deposition.

To examine the capability of the photoelectrodeposition process to profile photocarrier generation in arbitrary mesostructured semiconductor arrays, several p-Si tapered microwire arrays were evaluated. As with the cylindrical microwires investigated herein, each tapered wire array consisted of structures that were ~30 μm in height on a 7 μm pitch in a square lattice. As with the cylindrical wires, the tapered wires had a diameter of ~ 3 μm at the tips of the wires. The tapered wires had however a ratio of their base diameter to tip diameter, ρ, of 1.4, 1.6 or 2.3 (ρ = 1 for cylindrical wires). For wires with ρ = 1.4 and 1.6, the wire diameter tapered linearly from tip to base, whereas for wires with ρ = 2.3, the diameter tapered nonlinearly, producing a bottle-like shape. Figure 4.5 (a)-(c) depicts two-dimensional representations (side-view) of the simulated photocarrier generation rates in tapered microwires with ρ = 1.4, 1.6, and 2.3, respectively, under simulated illumination with λ_{avg} = 461 nm. In each case, the simulations indicated the presence of a narrow, well-defined

region at the very tip of the wires where the generation was approximately an order of magnitude higher than in any other region in the microwire volume, as observed for the cylindrical wire at this wavelength (Figure 3(a)). For ρ = 1.6, a radially thin region of elevated generation, extending 10 μm down from the tip in the axial dimension, was observed in the radial center of the wire. This behavior was however not observed for other values of ρ at this wavelength. For ρ = 2.3, the generation at the wire sidewalls was enhanced compared to the other structures, in manner consistent with increased collection of normal incidence photons due to the significant taper.

Figure 4.5 (d)-(f), (g)-(i), and (j)-(l), present data analogous to that in Figure 4.5 (a)-(c) but using simulated illumination with λ_{avg} values of 516, 630, and 940 nm, respectively. As with the case of the cylindrical wires, at these wavelengths, enhanced coupling to the waveguide mode was observed in the generation profiles. For λ_{avg} = 516 nm, and for wires with every value of ρ, the simulations each exhibited an axially well-defined, radially thick, region of high generation near the top of the wire, with a radially thin region of similarly high generation extending for several μm directly below through the radial center of the wire. Such results were consistent with the cylindrical case (Figure 4.4 (b)). However, for ρ = 1.4, the region of radially thin high generation extending below the tip was more pronounced and extended > 5 μm down the axial dimension. For ρ = 1.6, this same region extended approximately midway down the axial dimension of the wire, and a second, similarly shaped, high generation region was observed in the bottom quarter of the wire. For ρ = 2.3, the region of high generation extending below the tip was axially shorter than observed for the other shapes, but an isolated, radially thin region of high generation, < 5 μm long in the axial dimension, was observed ~10 μm from the top of the wire. Enhanced generation at the sidewalls was also observed for ρ = 2.3 relative to the other shapes, consistent with the observations for λ_{avg} = 461 nm. For λ_{avg} = 630 nm, the simulated generation in the tapered wires was generally described by a region of radially thick high generation near the tips of the wires, with similarly high generation in a radially thin region at the wire center throughout the entire axial length. The region of radially thick high generation near the tips was longer in the axial dimension for all values of ρ with λ_{avg} = 630 nm than with λ_{avg} = 461 or 516 nm. However, the axial length of this region decreased as ρ increased. For ρ = 1.4, less generation in the second quarter from the top of the wire, and additional generation in the bottom quarter, was observed relative to the wires with greater ρ values. For λ_{avg} = 940 nm, a significant concentration of generation in the wire tip relative to the rest of the microwire volume was not

observed for any value of ρ. Rather, the carrier generation was generally consistent in the axial dimension, with highest generation concentrated in the center of the wire volume. However, as ρ increased, the generation did appear to decrease somewhat in the bottom half of the wire.

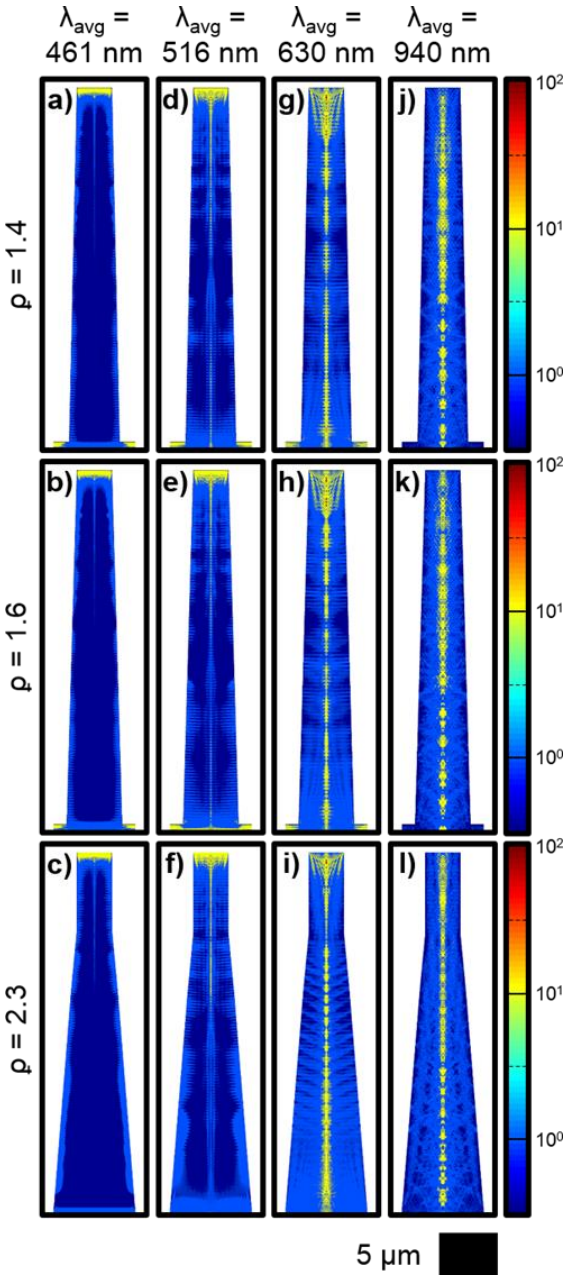

Figure 4.5*: (a−l) Simulated relative photocarrier generation rates in tapered Si microwires with a 3 μm wire top diameter and 30 μm wire height in a square lattice with a 7 μm wire pitch under narrowband illumination with spectral profiles having λavg as indicated*

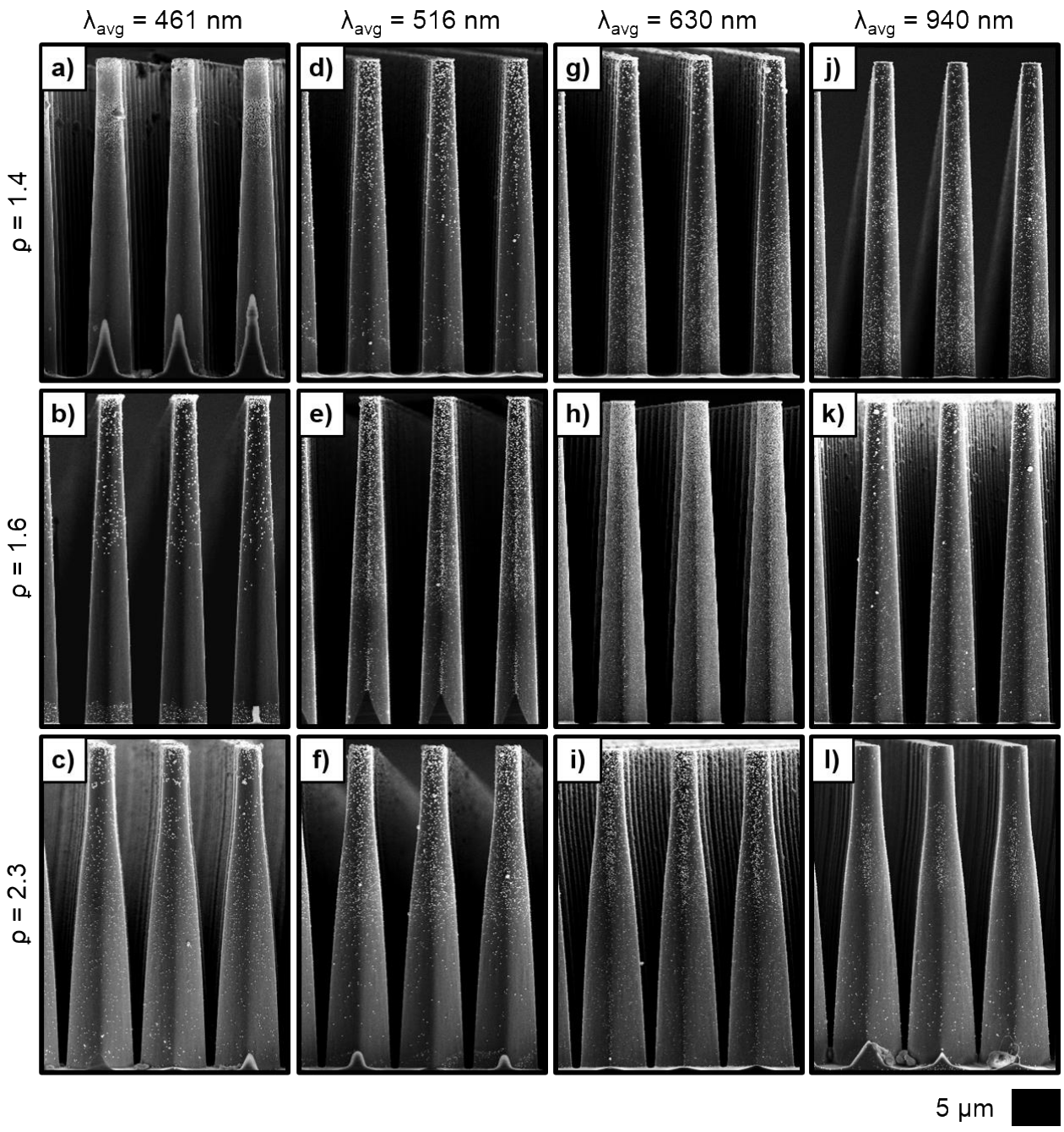

Figure 4.6*: (a−l) Representative SEMs of tapered p-Si microwire arrays with with ~ 3 µm wire top diameter, 7 µm wire pitch, and 30 µm wire height in a square lattice, upon which Au was photoelectrodeposited from a* $HAuCl_4$ *solution with a charge density of 0.10 C* cm^{-2} *using narrowband LED illumination having* λ_{avg} *as indicated. The ratio of the wire diameter at the base to that at the top (ρ) is indicated.*

Figure 4.6 presents experimental data complementary to the modeling data shown Figure 3.5, and is arranged in an analogous fashion. Specifically, Figure 4.6 (a)-(l) present cross-sectional SEMs of tapered p-Si microwire arrays with values of ρ = 1.4, 1.6 and 2.3, wherein Au was photoelectrodeposited with LEDs having λ_{avg} values of 461, 516, 630 and 940 nm, respectively, in the same manner as for the cylindrical wires (Figure 4.2). At every value of ρ, photoelectrodeposition with λ_{avg} = 461 nm illumination resulted in very dense Au plating at the very tip of the wires, consistent with the well-defined, narrow high-generation region indicated by the simulations in this volume of the wires (Figure 4.5 (a)-(c)) and with the behavior observed for the cylindrical case (Figure 4.2 (a)). For ρ = 1.6, photoelectrodeposition was also observed below the tip in the top half of the wires, consistent with elevated generation observed in the center and near the sidewalls in this volume of the wire via simulation (Figure 4.5 (b)). Similarly, for ρ = 2.3, sparse deposition was observed over the full axial dimension below the tip, consistent with the simulated prediction of elevated sidewall generation (Figure 4.5 (c)). Photoelectrochemical Au plating with λ_{avg} = 516 nm illumination on wires with ρ = 1.4 resulted in a gradient of deposition in the top half of the wire, wherein dense plating near the tip transitioned to sparse near the axial midpoint. For ρ = 1.6, significant deposition was observed from the top of the wire down to the axial midpoint and also in the axial bottom quarter. This result is consistent with the simulations (Figure 4.5 (d)-(e)), which indicated significantly enhanced generation rates in the same axial segments for which Au plating was observed. For ρ = 2.3, heavy plating was observed near the top of the wire, with substantial, but less dense, deposition in axial top half and sparse deposition in the bottom half. The relatively higher deposition in the top half of this structure is consistent with the prediction of generation concentration in this volume (Figure 4.5 (f)). Utilization of λ_{avg} = 630 nm illumination for deposition on wires with ρ = 1.4 resulted in significant deposition over the axial top quarter and bottom half of the wires, and sparser deposition over the second quarter. Deposition with λ_{avg} = 630 nm illumination on wires with ρ = 1.6 and ρ = 2.3 resulted in a gradient of Au plating, with significant deposition at tops of the wires and sparse deposition near the bottoms. These results are consistent with the concentration of generation along the axial dimension of the wires, as predicted by the simulations (Figure 4.5 (g)-(i)). Deposition with λ_{avg} = 940 nm illumination on wires with ρ = 1.4 resulted in relatively conformal plating. This conformality matched the lack of axial generation concentration indicated by the modeling (Figure 4.5 (j)). Results for deposition with λ_{avg} = 940 nm illumination on wires with ρ = 1.6 and 2.3 were similar, but with sparser deposition in the axial bottom halves of the wires. The

simulations predict a similar amount of total generation in these structures as for those with $\rho = 1.4$, but because the spatial volume is larger, the generation concentration is lower, consistent with the experimental observations.

4.4 Potential Applications

The collective data suggest that the spatially varying relative charge-carrier generation rates in a p-type semiconductor mesostructure under illumination can be physically recorded via cathodic photoelectrodeposition of a metal. For each p-Si microwire array and illumination spectrum investigated, the localization of Au deposited photoelectrochemically on the surface directly correlated with the relative concentration of carrier generation in the adjacent volume of the structure, as determined by computer simulation. In this work, computational assessment of the spatial dependence of charge-carrier generation was in part enabled by the high degree of uniformity and symmetry in the wire arrays. Each wire was considered as an identical element in a semi-infinite square lattice, and periodic boundary conditions were utilized to simulate a macroscopic array by considering only a microscale volume. Analysis of mesostructures without significant uniformity and order thus could be computationally intractable, but still carried out rapidly via the photoelectrochemical profiling technique described herein. This method may be of particular interest for interrogation of materials generated by low temperature, wet-chemical and maskless techniques.[135-140] In this work, Si was utilized for demonstration, but since the imaging relies only on the light absorption and charge separation abilities intrinsic to semiconductors, the method should be readily generalizable to a wide class of materials. Similarly, Au was utilized as the marker material, but any metal that can be electrochemically deposited in a potential window compatible with the semiconductor may also be utilized. Additionally, while in this work cathodic deposition was used to record generation on a p-type material, n-type materials may be similarly treated using oxidative deposition to apply the marker or even possibly by anodization of the material itself.[141, 142] Anodic photoelectrochemical etching of semiconductor surfaces using illumination with spatially varying intensity has been used to generate microlenses, diffraction gratings, and transformation optics.[143-145] Moreover, the potential to direct spatially localized deposition on an array of semiconductor materials and morphologies suggests that photoelectrodeposition may be used as a template-free technique to selectively decorate semiconductor surfaces. This strategy could

utilize conformal illumination without a photomask and thus potentially generate features with sizes unconstrained by the optical diffraction limit. The deposition anisotropy could then be controlled by varying the excitation spectra to tune the spatial concentration of carrier generation in the structures.[146] Such a methodology may be utilized to place reflector materials for photovoltaic applications, catalysts for photoelectrochemical fuel generation systems, and conductive contacts for microelectronics [70, 147-151].

In summary, photoelectrochemical deposition of Au onto cylindrical p-Si microwire arrays resulted in spatially anisotropic metal plating at the microwire surface, wherein the localization of the plating was a function of the illumination wavelength. The same deposition process was repeated with n-Si wire arrays, and conformal deposition was observed regardless of wavelength. The spatial distribution of the photoinduced charge-carrier generation rates in the wires, as derived from computer simulations using a FDTD method, correlated well with the localization of the metal deposition observed experimentally. Analogous simulations of the spatially resolved photocarrier generation rates in a series of related p-Si microwire arrays with tapered (non-cylindrical) wires was also performed. Photoelectrodeposition was then performed on wires arrays with equivalent morphologies to those simulated, and the metal plating at the wire surfaces was observed to be a function of carrier generation concentration in the adjacent wire volume. The photoelectrodeposition of metals on semiconductor mesostructures thus appears to be of use for profiling charge-carrier generation in such structures. Additionally, the technique appears to be of potential use for maskless, directed deposition of materials with subwavelength features.

Chapter 5

Silicon Microcone Photocathodes

5.1 Status of Silicon Photocathodes

Microstructured photoelectrodes have several advantages relative to planar electrodes, including the ability to optimize light absorption and carrier collection in impure, inexpensive semiconductors grown by scalable methods, as well as the ability to support high loadings of electrocatalysts without deleterious absorption of incident photons [88, 152]. The use of such microstructured materials with appropriately integrated electrocatalysts in flexible, ionically conductive, membrane-embedded devices allows for a fully integrated system for water splitting [153, 154], HI splitting [84, 155], photoelectrochemical CO_2 reduction [156, 157], or N_2 fixation [158, 159]. Electrocatalysts are generally deposited on the light-incident side of the photoelectrode, shadowing the underlying semiconductor and thereby reducing the light-limited current density. The optimal catalyst loading is therefore determined by the balance between catalyst activity and optical losses due to reflection and parasitic absorption [160-162].

Bare, planar Si photocathodes exhibit light-limited photocurrent densities $|J_{ph}| < 29$ mA cm^{-2}, due to front-surface reflection optical losses [163]. J_{ph} can approach closer to theoretical maximum of ~ 44 mA cm^{-2} for Si under 100 mW cm^{-2} of Air Mass 1.5 illumination [164] with the use of an antireflective coatings, combined with surface texturing such as micropyramids (μ-pyramids) by anisotropic wet-chemical etching or high-aspect-ratio structuring of the Si [31, 32, 52, 54]. Antireflective coatings such as SiO_2, Si_3N_4, or Al_2O_3, as commonly used in photovoltaic devices are not catalytically not active and are therefore not ideal for photoelectrode systems [165]. Most of the highly active catalysts reflect and parasitically absorb light in the solar spectrum. These optical losses by the catalyst can be reduced by decreasing the catalyst loading to increase transmissivity [161]; by developing transparent and antireflective catalysts [166, 167]; by depositing the catalyst as islands rather than as a continuous film [168]; and/or by strategically placing the catalyst out of the path of incident light on three-dimensionally structured Si substrates [169]. The ideal electrode

microstructure would simultaneously minimize reflection and absorption losses in the catalyst while optimizing the catalyst loading to reduce the overpotential required to convert photogenerated charge carriers into fuel.

H_2-evolving Si photocathodes have been made using surface texturing such as μ-pyramids [167, 170], nanowires [171-180], and microwires (μ-wires) [160-162, 169, 176-181]. Light-limited current densities as high as $|J_{ph}| = 43$ mA cm^{-2} have been reported for Si μpyramids coated with a highly transparent and potentially antireflective MoS_xCl_y catalyst grown by chemical-vapor deposition [167]. A photocurrent density at the reversible hydrogen electrode potential (RHE), J_{RHE} = -37.5 mA cm^{-2}, was obtained using a transparent $NiCoSe_x$ catalyst deposited via light-assisted electrodeposition onto Si nanowire array photocathodes [179]. For Si microwires (μ-wires), J_{RHE} = -35.5 mA cm^{-2} was obtained by optimizing both the coverage of an electrodeposited Ni-Mo catalyst on the μ-wires and the pitch of the μ-wires [162]. Replacing the catalyst in these structures with thin Pt (~ 5 nm or less), which is widely used because of its high activity and stability in corrosive environments, leads to substantial optical absorption and reflection losses, and thus resulting in a decrease of 5–7 mA cm^{-2} in J_{RHE} [162, 167, 179].

Polymer-embedded Si μ-wires with an antireflective Si_3N_4 coating and scattering particles can absorb up to 84.4% of incident radiation at normal incidence, which is above the light trapping limit [20] for an equivalently thick Si substrate [182]. However, widely spaced Si μ-wires on a Si substrate reflect >30 % of normal-incident light due to the flat tops of the μ-wires. In contrast, tapering the cylindrical shape of Si μ-wires into Si microcones (μ-cones) with a tip curvature of 25 nm enhanced the absorption of Si to > 90% at normal incidence, equivalent to 99.5% of the classical broadband light-trapping limit, with above-the-limit absorption observed at longer wavelengths [31, 32]. Such Si μ-cones reflect only ~1% of normal-incident light, which is comparable to reflection from black silicon substrates [52-54]. This is due to the coupling of broad-band light to multiple available waveguide modes whose resonance exists at various radii provided by the conical geometry [31, 183, 184]. The high surface area for catalyst loading provided by the μ-cone geometry makes Si μ-cones an attractive architecture for Si photocathodes in hydrogen-producing systems. Herein we investigate the H_2-evolution performance of Si μ-cone array photocathodes coupled with either a highly active but opaque Pt catalyst or with Co-P as an example of a highly optically absorbing electrocatalyst comprised of earth-abundant elements.

5.2 Homojunction Si photocathodes with sputtered Pt catalyst

Czochralski-grown p-type Si wafers with orientation <100> and with a resistivity of 0.6-0.8 ohm-cm (Addison Engineering, Inc.) were photolithographically patterned with a square grid of Al_2O_3 circles that were 3 μm in diameter with a 7 μm pitch. The Al_2O_3 was deposited to a thickness of 200 nm via electron-beam evaporation. The μ-cones were etched from the masked p-Si wafer using an Oxford Dielectric System 100 ICP/RIE following a procedure described previously [185]. A capacitive coupled power of 7 W, and an inductively coupled power of 900 W, was used for etching. Etching was performed in three steps, in which the ratio of SF_6 to O_2 gas was varied stepwise from 70 sccm : 6 sccm to 70 sccm : 7 sccm by increasing the rate of O_2 flow by 0.5 sccm every 30 min. The chamber temperature and pressure were maintained at -130 ^oC and 10 mTorr, respectively. After etching, samples were cleaned via a modified RCA standard clean 1 (5:1:1 H_2O:NH_4OH:H_2O_2 at 70 °C) followed by an RCA standard clean 2 (6:1:1 H_2O:HCl:H_2O_2 at 70 °C). The samples were dipped in HF in between the cleaning steps, which also resulted in removal of the Al_2O_3 etch mask.

After cleaning, the samples were dipped in 10% HF(aq) for 1 min before thermal P diffusion using a Saint-Gobain PH-900 PDS diffusion-doping source at 850 ^oC for 15 min under N_2 ambient, to yield an n^+p homojunction. To reduce thermal stresses, the samples were inserted into, and removed from, the doping furnace over the course of one minute. The Si μ-cones were then heated to 150 ^oC on a hot plate, and mounting wax (Quickstick 135, South Bay Tech) was melted into the array as a mask. Excess wax was removed by reactive-ion etching using an O_2 plasma at a forward power of 400 W and 300 mTorr operating pressure. The wax was etched until 6-9 μm of the tips of the μ-cones were exposed. The samples were then dipped in 10% HF for ~1 min to remove the native oxide over the Si μ-cones, and Pt was sputtered onto the samples. The samples were then immersed in acetone and sonicated for 15 min to completely remove the wax, resulting in Si μ-cones with Pt selectively deposited over the tips of the μ-cones.

Figure 5.1 (a-f) schematically shows the fabrication process for the n^+p-Si μ-cone array photocathodes, with the tips of the μ-cones supporting a Pt catalyst (n^+p-Si/Pt μ-cones) for the hydrogen evolution reaction (HER). Figure 5.1 (g) shows a scanning-electron micrograph (SEM) of a cross section of an as-prepared n^+p-Si/Pt μ-cone-array photocathode with Pt covering 6-9 μm at the tips of the μ-cones.

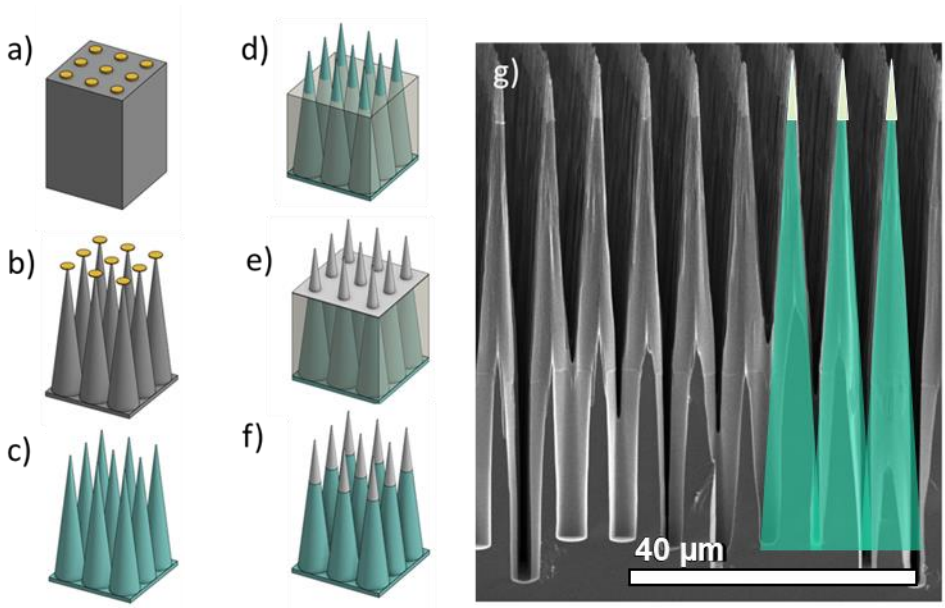

Figure 5.1*:Schematic for the fabrication of n+p-Si μ□cone array photocathodes with Pt selectively loaded on the tips of the μ-cones. (a) Aluminum oxide mask (yellow) patterned on p-type silicon (gray). (b) Controlled undercutting of the etch mask leads to aspect-ratio cones. (c) Removal of the etch mask followed by formation of an n^+-emitter layer (green) via phosphorus doping. (d) Infilling with wax (transparent gray) followed by directional O_2 etching to expose tips. (e) Uniform deposition of Pt via sputtering. (f) Removal of the wax with acetone leaves Pt only at the cone tips. (g) Scanning-electron micrograph of n^+p-Si μ-cone photocathodes with Pt selectively deposited on the tips of the μ-cones.*

To make bottom-facing electrodes, In-Ga (Alfa Aesar) was scratched into the back sides of Si μ-cone chips, and a Cu-Sn wire was affixed to the In-Ga using Ag paint having a grain size < 1.0 μm (PELCO, Ted Pella) as an adhesive. The Cu-Sn wire was fed through 6 mm diameter borosilicate glass tubing, and the electronically contacted chips were sealed onto the end of the tubing using an opaque, insulating epoxy (Hysol 9460) that was allowed to cure at room temperature for at least 12 h or at 80 °C for 6 h. The performance of photocathodes for photoelectrochemical hydrogen evolution was measured in H_2-purged 0.50 M H_2SO_4(aq) (TraceMetals grade, Fisher) under 100 mW cm^{-2} of simulated AM1.5 illumination produced by a filtered Hg (Xe) lamp powered at 290 W. A Biologic SP-200 was used for the potentiostat in a three-electrode configuration. A Ag/AgCl (Saturated KCl) reference electrode was calibrated against the reversible hydrogen-evolution

potential, RHE, using a platinum-black electrode, and a graphite rod behind a porous glass frit served as the counter electrode. Current density vs potential, *J-E*, data was obtained by sweeping the potential at 50 mV s^{-1} from open circuit to -0.2 V vs RHE. The electrolyte was stirred rapidly with a magnetic stir bar to remove hydrogen bubbles from the surface of the device.

Figure 5.2 compares the current density vs potential (*J-E)* behavior under 100 mW cm^{-2} of simulated AM 1.5 illumination for varied thicknesses of Pt deposited onto as-fabricated n^+p-Si/Pt μ-cone array photocathodes, planar n^+p-Si/Pt photocathodes, and pyramidally-textured n^+p-Si/Pt photocathodes (μ-pyramid), when operated in contact with H_2-saturated 0.50 M H_2SO_4(aq). Of the three photocathode geometries, the μ-cone array exhibited the highest light-limited photocurrent density $|J_{ph}|$ (at large negative biases, < -1.5 V versus RHE). As expected, the overpotential required for the HER decreased as Pt was added to the photocathodes. For the planar and μ-pyramid geometries, increasing the thickness of the Pt resulted in improvements to the fill factors (*ff*) of the *J-E* characteristic; however, increasing the thickness of the Pt catalyst beyond 2 nm resulted in reductions to $|J_{ph}|$ due to optical absorption and reflection losses associated with the Pt layer. For the planar and μ-pyramid geometries, $-J_{RHE}$ decreased to < 10 mA cm^{-2} when the thickness of the Pt layer reached 8 nm or 16 nm, respectively. However, Si μ-cone array photocathodes with 8 nm of Pt yielded a $-J_{RHE}$ = 33 ± 2 mA cm^{-2}, only ~6% less than $-J_{ph}$ = -35.0 mA cm^{-2} observed for bare np^+-Si μ-cone photocathode arrays (Figure 5.2 (c)). For n^+p-Si/Pt μ-cone array photocathodes with 8 nm of Pt, the voltage required to drive the HER at a rate corresponding to a current density of -10 mA cm^{-2}, V_{-10}, was -70 mV relative to the open-circuit potential (E_{oc}). Doubling the thickness of the Pt layer, from 8 nm to 16 nm, on the tips of the μ-cones resulted in a slight decrease in - J_{RHE}, to 31 ± 3 mA cm^{-2}, but did not change V_{-10}. The values of V_{-10} for planar Si and μ-pyramidal Si photocathodes were 87 mV, and 80 mV respectively, were slightly higher than those observed for Si μ-cone arrays with at least 8 nm thick Pt, despite complete coverage of their surface with 4 nm of Pt. Further increases to the thickness of the Pt, to 8 nm on planar Si, and 16 nm on μ-pyramidal arrays, led to improved fill factors but resulted in $-J_{ph}$< 10 mA cm^{-2}. Despite the Pt catalyst covering just ~2% of the total microstructured Si μ-cone surface area, the μ-cone geometry maintained a relatively low overpotential while simultaneously maintaining $-J_{ph}$ that is higher than that can be achieved by bare planar or random μ-pyramidal textured Si photocathodes.

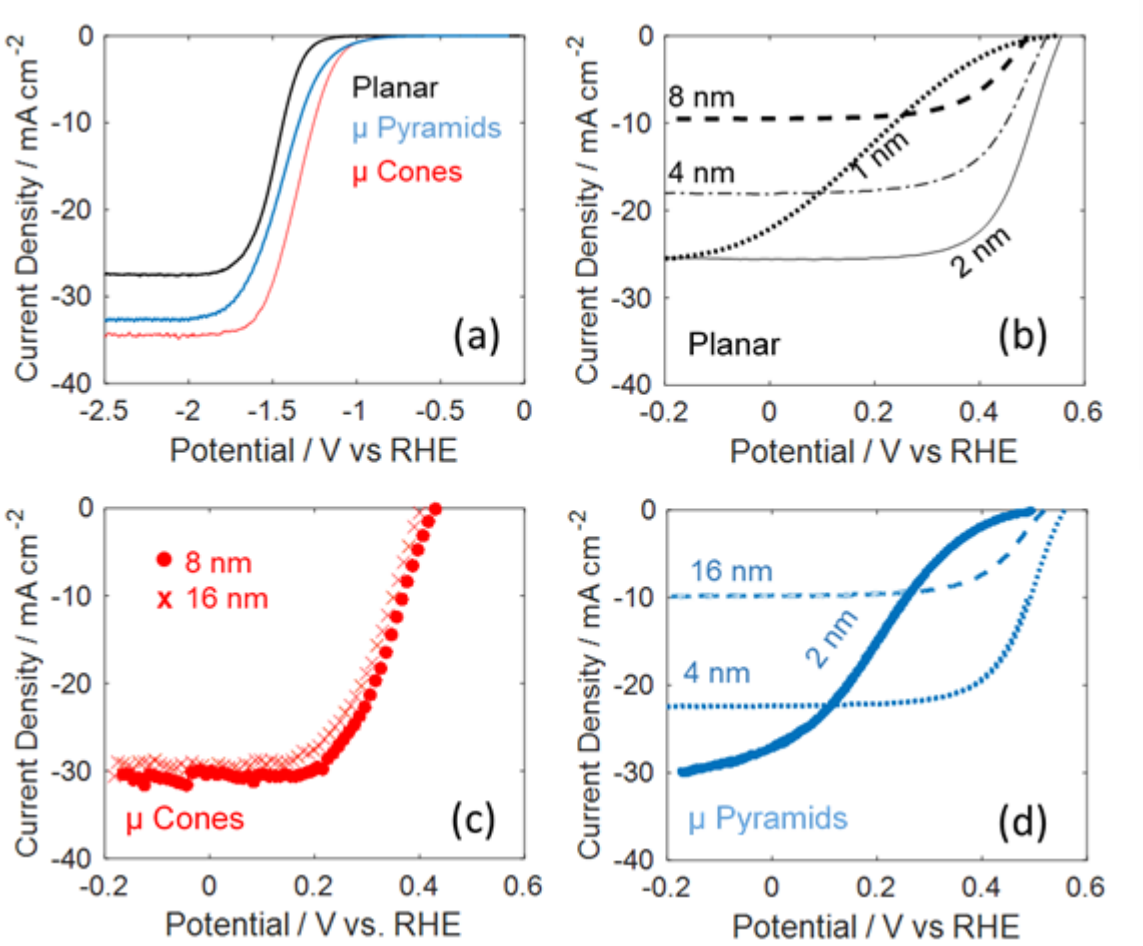

***Figure 5.2**: Effect of Pt loading on the J-E behavior of n^+p-Si photocathodes with planar, μ-pyramid, and μ-cone array morphologies, as measured in contact with H_2-saturated 0.50 M H_2SO_4(aq) while illuminated by 100 mW cm^{-2} of simulated Air Mass (AM) 1.5 illumination. (a) J-E performance of bare (no Pt) n^+p-Si photocathodes with planar (black), μ-pyramid (blue), and μ-cone (red) morphologies. Representative J-E behavior for n^+p-Si/Pt photocathodes with varied Pt loadings for the (b) planar, (c) μ-cone, and (d) μ-pyramid morphologies.*

The ideal regenerative cell efficiency (η_{IRC}) [186] for n^+p-Si/Pt μ-cone photocathodes with 8 nm of Pt was 5.8 ± 1.1 %, with a champion device yielded η_{IRC} = 6.9%. The η_{IRC} for n^+p-Si/Pt μ-cone photocathodes with 16 nm Pt was 5.6 ± 1.1 %, with a champion device yielded η_{IRC} = 7.4% (Figure 5.3). The use of an n^+p-Si homojunction with 8 nm or with 16 nm of Pt on Si μ-cones resulted in an open circuit voltage (E_{oc}) of 416 ± 15 mV and 402 ± 22 mV respectively vs RHE and allowed light-limited photocurrent densities to be produced at potentials > 0 V vs RHE. The E_{oc} values for the

champion device were 431 mV and 442 mV, for 8 nm and 16 nm Pt films, respectively. The primary difference between the performance of champion devices and average devices thus arose from the higher photovoltages of champion devices relative to average photocathodes as fabricated. The planar and μ-pyramid photocathodes showed higher photovoltages than the μ-cone photocathodes (Figure 5.2), even though all the photocathodes were diffusion doped by a nominally identical process. SEM images indicated that the Si μ-cone arrays had an ~12.5-fold increase in junction area compared to a planar Si electrode, leading to an expected decrease in E_{oc} of ~65 mV assuming a diode quality factor of 1.0 [187]. Diffusion-doped, etched Si μ-wire based photocathodes for HER have been reported to exhibit E_{oc} up to 480 mV [161]. The observed E_{oc} of 440 mV for the champion photocathodes thus suggests that further optimization in diffusion doping could increase further the η_{IRC} of the Si μ-cone arrays.

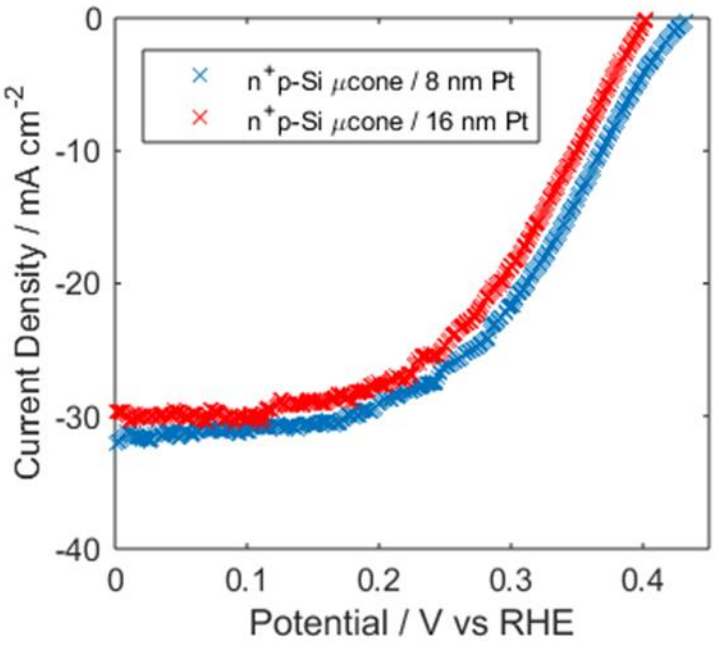

***Figure 5.3**: Performance of champion n^+p-Si/Pt μ-cone photocathodes with 8 nm or 16 nm thick Pt loaded on the tips of the μ-cones. The photocathodes were tested in H_2-saturated 0.50 M H_2SO_4(aq) under 100 mW cm^{-2} of simulated AM1.5 illumination, with rapid stirring of the electrolyte to remove bubbles from the electrode surface.*

When Pt was deposited to a thickness > 4 nm, n^+p-Si/Pt photocathodes were stable under air exposure for a few days between fabrication and testing. These electrodes also reversibly passed anodic current, indicating that the Pt layer protected the Si from forming an insulating interfacial oxide layer. After pauses at open circuit, photocathodes with 2-4 nm of Pt exhibited a decrease in η_{IRC} with successive scans, due to a decrease in the fill factor. In contrast, n^+p-Si/Pt μ-cone array photocathodes loaded with 16 nm of Pt did not show a decrease in fill factor with successive scans (Figure 5.4). Even though the catalytic overpotential was not changed by increasing the thickness of Pt beyond 4 nm for n^+p-Si/Pt photocathodes with planar or μ-pyramid geometries, the increased thickness of the Pt layer thus beneficially improved the stability of these electrodes. The increased Pt thickness needed for stability decreased the amount of light transmitted into the Si and limited the photocurrent densities obtainable from n^+p-Si/Pt planar and μ-pyramid photocathodes. In contrast, little or no loss of J_{ph} or fill factor accompanied the increase in Pt thickness (16 nm) required for stable performance of the n^+p-Si/Pt μ-cone array photocathodes.

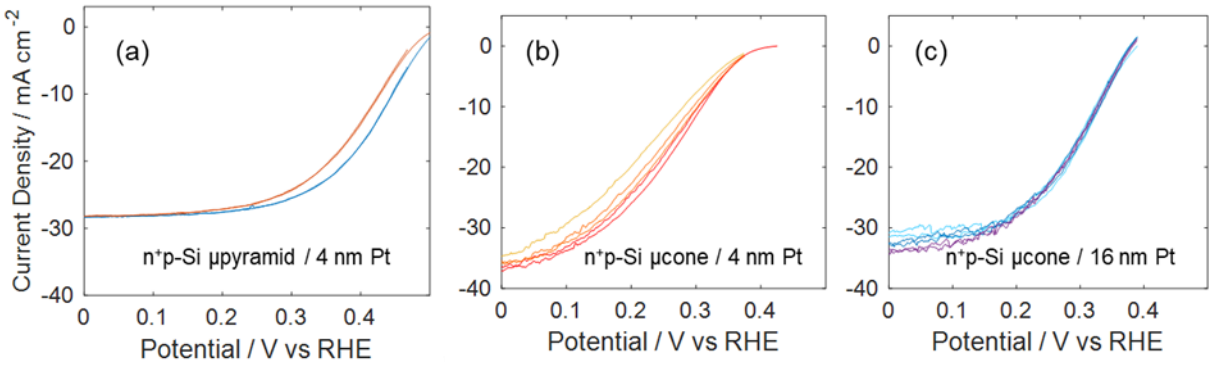

Figure 5.4*: Stability of n^+p-Si/Pt photocathodes operated in contact with H_2-saturated 0.5 M H_2SO_4(aq) while under 100 mW cm^{-2} of simulated AM1.5 illumination. For n^+p-Si/Pt μ-pyramid photocathodes with (a) 4 nm of Pt, a decrease in fill factor was observed after the first potential scan. For n^+p-Si/Pt μ-cones, devices with (c) 4 nm of Pt on the μ-cone tips showed a decrease in fill factor with successive scans, whereas devices with (d) 16 nm of Pt did not show an improvement in J_{ph} and no decay in fill factor with successive scans.*

5.3 Heterojunction Si photocathodes with electrodeposited Co-P catalyst

Co-P, an earth abundant, active HER electrocatalyst, was used to explore the compatibility of Si μ-cone arrays with catalysts other than noble metals such as Pt. On p-type Si, Co-P produces a photovoltage in the absence of a homojunction [188]. p-Si μ-cone arrays were fabricated via the above etching and cleaning procedures but were not doped with an n^+ emitter layer. Bottom-facing electrodes were made from the p-Si μ-cones as described in the previous section, and Co/Co-P was photoelectrochemically deposited onto the surface of the p-Si μ-cones using illumination from a narrowband LED (Thorlabs) with an intensity-averaged wavelength of 625 nm until a charge density of 400 mC cm^{-2} was passed. The light intensity at the surface of the sample was ~200 mW cm^{-2}. The Co/Co-P plating bath has been described elsewhere [189, 190], and was purged vigorously with Ar(g) prior to and during the deposition, with a gas stream in close proximity to the sample to drive local convection.

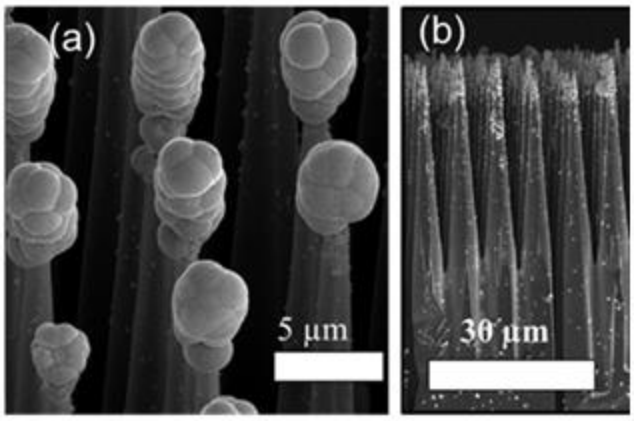

Figure 5.5*: (a) Scanning-electron micrograph (SEM) of as deposited Co/Co-P photoelectrodeposited onto the tips of p-Si μ-cones. The Co/Co-P loading, as determined by the charge density passed during the photoelectrodeposition, was 400 mC* cm^{-2}*. (b) SEM image of a cross section of a p-Si/Co-P μ-cone array after removal of excess Co by potential cycling in 0.50 M* H_2SO_4 *(aq).*

The bare p-Si μ-cone arrays predominantly absorbed light at 625 nm at the tips of the μ-cones [31]. Due to deposition at mass-transport-limited current densities, photoelectrodeposition of the Co/Co-P film occurred preferentially at the tips of the Si μ-cones, producing clumps > 1 μm in diameter, shadowing the underlying array (Figure 5.5 (a)). To obtain an active Co-P catalyst, excess Co was removed by extended potential cycling in contact with 0.50 M H_2SO_4(aq) while under 100 mW cm^{-2} of simulated AM1.5 solar illumination [188]. Potential cycling resulted in a restructuring of the catalyst film into nanoscale islands that were located predominantly at the tips of the μ-cones (Figure 5.5 (b)).

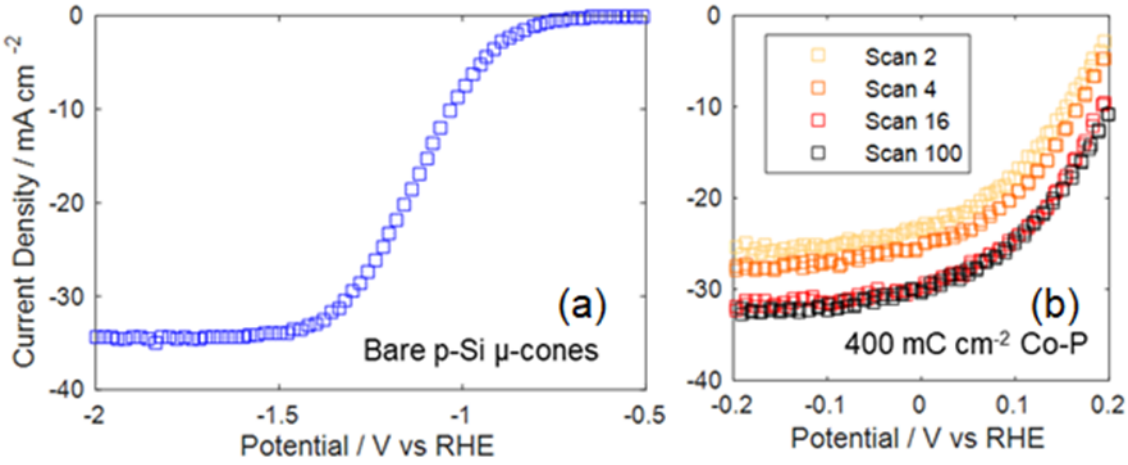

***Figure 5.6**: Evolution of the J-E behavior of a photocathode consisting of a p-Si/Co-P μ-cone array, when immersed in H_2-saturated 0.50 M H_2SO_4(aq) and illuminated with 100 mW cm^{-2} of simulated AM 1.5 illumination with rapid stirring, compared to the same p-Si μ-cone array photocathode prior to catalyst deposition (a). (b) Effects of extended potential cycling in contact with 0.50 M H_2SO_4(aq) under 1-sun illumination on the J-E behavior of a p-Si μ-cone array photocathode loaded with Co/CoP after 2, 4, 16, and 100 scans from -0.376 V to +0.224 V vs RHE at 50 mV s^{-1}. The first and last scans were recorded after 20 s and 40 min, respectively.*

Figure 5.6 shows the *J-E* behavior of an illuminated bare p-Si μ-cone array photocathode, as well as the evolution of the *J-E* behavior of a p-Si/Co-P μ-cone array photocathode operated in contact with 0.50 M H_2SO_4(aq). Both J_{ph} and E_{oc} of the p-Si/Co-P μ-cone array photocathode improved with cycling and began to stabilize after ~ 16 voltammetric *J-E* cycles. Deposition of Co-P on planar, μ-pyramid, or μ-wire Si photocathodes yielded $-J_{ph}$ of 15 mA cm^{-2}, 20 mA cm^{-2}, and 25 mA cm^{-2}

respectively [188], whereas p-type Si μ-cone/Co-P photocathodes exhibited $-J_{ph}$ = 32 ± 2 mA cm^{-2}. Compared to bare p-type Si μ-cone array photocathodes, the deposition of Co-P on the Si μ-cone tips resulted in an average decrease in $-J_{ph}$ of 3 mA cm^{-2}. Si μ-cone array photocathodes exhibited $-J_{sc}$ = 29 ± 2 mA cm^{-2} compared to $-J_{sc}$ = 13 mA cm^{-2}, 18 mA cm^{-2}, and 22 mA cm^{-2} from planar, μ-pyramidal, and μ-wire array Si photocathodes, respectively [188], demonstrating the superior light trapping properties of the Si μ-cone morphology when coupled with the Co-P HER catalyst.

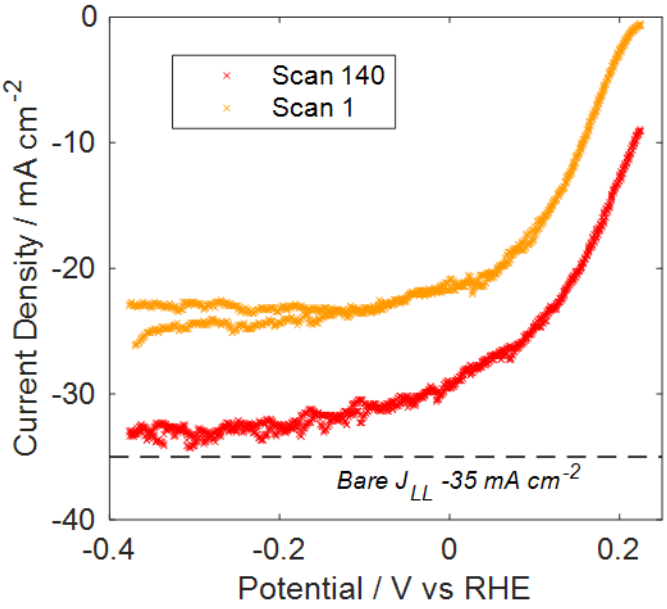

***Figure 5.7**: Performance of champion n$^+$p-Si/CoP μ-cone photocathodes with 400 mC cm^{-2} Co-P deposited photoelectrochemically. The device was cycled from the initial open circuit potential to -0.376 V vs RHE in H_2-saturated 0.50 M H_2SO_4 (aq) under 100 mW cm^{-2} of simulated AM 1.5 illumination, with rapid stirring of the electrolyte to remove bubbles from the electrode surface.*

The E_{oc} for the p-Si/Co-P μ-cone array photocathodes was 331 ± 50 mV vs RHE, and the highest observed E_{oc} for the p-Si/Co-P μ-cone photocathodes was 384 mV vs RHE. The p-Si/Co-P μ-cone array photocathodes did not require a diffusion-doped homojunction but yielded lower E_{oc} values than the n$^+$p-Si/Pt μ-cone array photoelectrodes. The p-Si/Co-P μ-cone array photocathodes reached a benchmark solar-to-fuel current density of -10 mA cm^{-2} at +197 ± 20 mV vs RHE. A champion device achieved the benchmark current density at +220 mV versus RHE, with η_{IRC} = 3.1% (Figure

5.7). This efficiency is comparable to the value obtained from the Si μ-wire morphology and is higher than the values reported for planar and μ-pyramid Si photocathodes (Table 4.1) [188].

Device Type	J_{sc} *(mA cm^{-2})*	J_{ph} *(mA cm^{-2})*	E_{oc} *(mV)*	η_{IRC} *(%)*	η_{IRC}* *(%)*
n^+p-Si μ–cones, 8 nm Pt	-33 ± 2	-34 ± 3	416 ± 15	5.8 ± 1.1	6.9
n^+p-Si μ–cones, 16 nm Pt	-31 ± 3	-32 ± 3	402 ± 22	5.6 ± 1.1	7.4
n^+p-Si Planar 4nm Pt	-17 ± 1	-17 ± 1	539 ± 9	5.4 ± 0.4	5.7
n^+p-Si μ-pyramids, 4 nm Pt	-24 ± 3	-24 ± 3	533 ± 18	6.9 ± 1.4	8.0
n^+p-Si μ-pyramids, 16 nm Pt	-9.1 ± 1.5	-9.1 ± 1.5	519 ± 10	2.8 ± 0.4	3.0
p-Si μ–cones, Co-P	-29 ± 2	-32 ± 2	331 ± 50	2.7 ± 0.3	3.1
*p-Si μ-pyramids, Co-P***	-18 ± 1	-20	286 ± 11	-	-
*p-Si planar, Co-P***	-13 ± 1	-15	265 ± 26	0.82 ± 1.3	0.98
*p-Si μ-wires, Co-P***	-22 ± 2	-25	342 ± 24	2.4 ± 0.1	2.5
p-Si μ-cones, Bare	-	-35	-	-	-
p-Si μ-pyramid, Bare	-	-31	-	-	-
p-Si planar, Bare	-	-28	-	-	-

***Table 5.1**: Summary of performance metrics for planar, μ-pyramid, and μ-cone array photocathodes measured in contact with H_2-saturated 0.50 M H_2SO_4 (aq). Average values and standard deviations (in parentheses) were calculated from measurements of at least 5 separate μ-cone arrays, and from at least 3 separate photoelectrodes for planar or μ-pyramid morphologies. The light-limited current density, J_{ph}, was measured at -200 mV vs RHE; the current density at the formal potential of the H^+/H_2 redox system, J_{RHE}, was measured at 0 V vs RHE. E_{oc} is reported relative to RHE. * indicates performance of champion devices, and ** indicates values from a previous study [188].*

Figure 5.8 compares the reflectance in the wavelength range of 400 nm - 1100 nm for bare Si μ-cone array, a Si μ-cone array with 8 nm or 16 nm of Pt selectively deposited at the tips of the μ-cones, and a p-Si/Co-P μ-cone array electrode. No substantial change was observed in reflectance between n^+p-Si μ-cone arrays with and without a Pt coating, indicating that the incident light that is typically reflected from planar or μ-pyramid Si surfaces was redirected into the Si substrate due to the conical geometry. This behavior is similar to that observed previously in triangular transparent contacts over

solar cells [185, 191, 192]. The reflectance from the p-Si/Co-P μ-cone array was 5% higher than the reflectance from the n^+p-Si/Pt μ-cone array because the Co-P islands were rough compared to the sputtered Pt coating, allowing relatively higher outward scattering of light from the Co-P islands on the tips of the μ-cones. Although p-Si/Co-P μ-cones exhibited higher reflectance than the Pt-loaded μ-cones, the average J_{ph} was the same (-32 mA cm^{-2}) for p-Si/Co-P μ-cone arrays and n^+p-Si/Pt μ-cone arrays with 16 nm of Pt, indicating that 16 nm of Pt has a higher parasitic absorption than to Co-P in the 400 nm – 1100 nm wavelength range. Hence even after deposition of the catalyst, the Si μ-cone arrays had superior light trapping properties relative to bare Si pyramid structures.

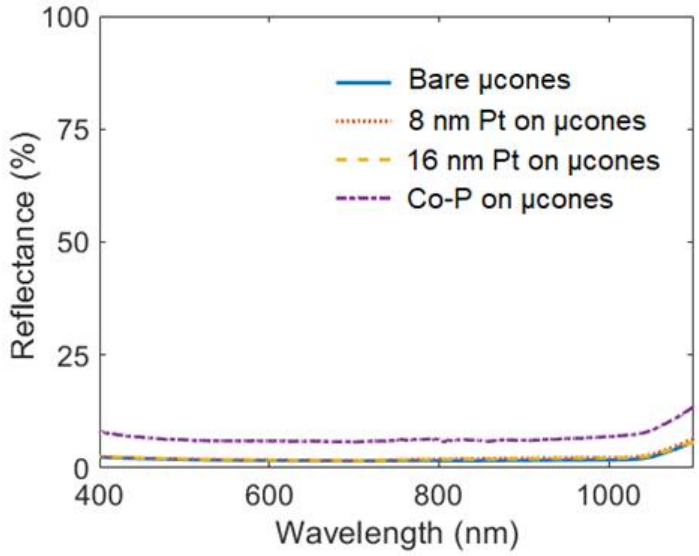

Figure 5.8*: Reflectance measurement of bare Si μ-cone arrays, Si μ-cone arrays with 8 and 16 nm of Pt or Co-P on their tips, as measured using a Cary 5000 UV-Vis-NIR with an integrating sphere.*

p-Si μ-cones were embedded in PDMS by spin coating a 10:10:1 solution of toluene, PDMS elastomer, and curing agent (Dow Sylgard™ 184) at 3000 rpm leaving the top ~15 μm of the μ-cones exposed. The samples were cured on a hot plate at 150 °C for ~ 30 min. The μ-cones were peeled off their substrate using a razor blade. The flexible polymer membrane was held on its edges sandwiched between Kapton tape and a glass slide, with the back side of the μ-cones facing up. The thickness of the tape ensured that the tips of the μ-cones were not damaged. 500 nm of Au was deposited onto the backs of the μ-cones via electron-beam evaporation. Electrodes were made using these flexible substrates with Ag ink connecting the Au back contact to a Cu-Sn wire that was fed

through 6 mm diameter borosilicate glass tubing. The electrodes were then sealed using an opaque, insulating epoxy (Hysol 9460) that was allowed to cure at room temperature for at least 12 h or at 80 °C for 6 h. Co-P was electrodeposited under similar conditions as used for the on-substrate samples.

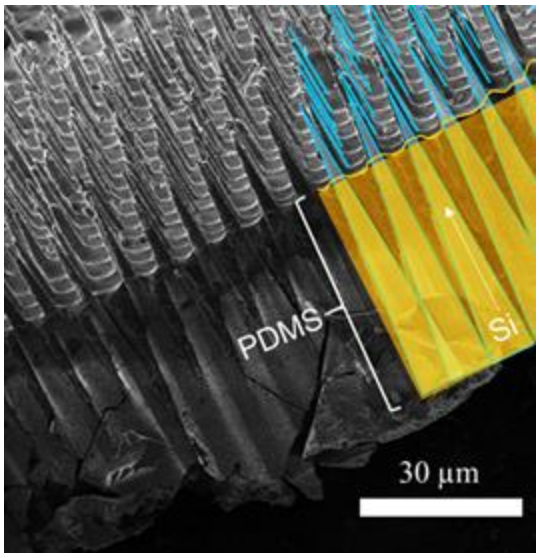

Figure 5.9*: SEM of polymer embedded Si µ-cones removed from substrate, after deposition of Co-P and potential cycling in 0.50 M H_2SO_4(aq).*

Figure 5.9 shows an SEM image of Si µ-cone arrays in PDMS with ~ 15 µm of the tips exposed, with the freestanding, polymer-embedded µ-cones arrays decorated with Co-P using the same procedure as described for the on-substrate p-type Si µ-cones. Free-standing devices were tested as photocathodes in 0.50 M H_2SO_4 (aq), to evaluate the performance of µ-cones in a membrane-embedded photocathode for hydrogen generation. Figure 5.10 presents representative *J-E* data in 0.50 M H_2SO_4 (aq) under 100 mW cm^{-2} of simulated AM1.5 illumination. These devices demonstrated an E_{oc} = 150 ± 36 mV and a J_{sc} = -0.94 ± 0.32 mA cm^{-2}, with a champion device demonstrating a J_{sc} = -1.41 mA cm^{-2}. At -200 mV vs RHE, free-standing Si µ-cones achieved J_{ph} = -6.5 mA cm^{-2} and the champion device exhibited J_{ph} = -8.1 mA cm^{-2} and remained active for 3 h of testing. The photoactivity indicates that many of the individual p-type Si µ-cones were successfully contacted with electrolyte during the Co-P catalyst deposition, and also while being tested as photocathodes. The photocurrent density was higher than previous demonstrations with Si µ-wires

embedded in polymer membranes [56, 84, 160]. Further optimization of the placement of catalysts to reflect the local carrier generation rate could be achieved using light-guided deposition of catalysts [69].

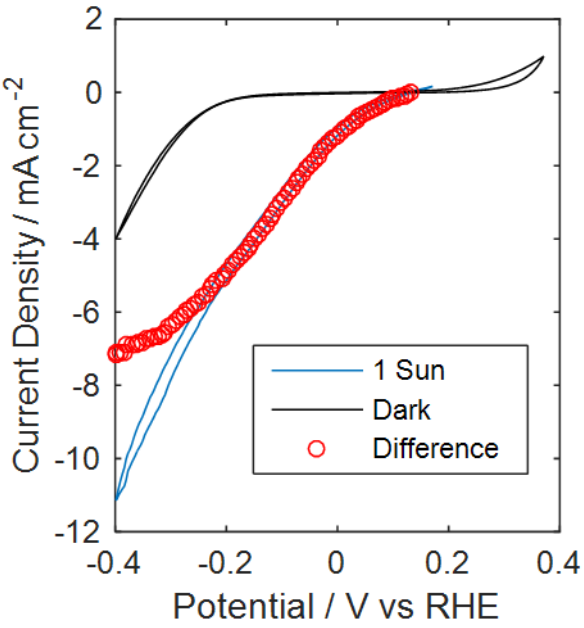

***Figure 5.10**: Representative J-E behavior of PDMS-embedded Si μ-cone array photocathodes decorated with Co-P and tested in 0.50 M H_2SO_4(aq) under 100 mW cm^{-2} of simulated AM1.5*

The p-Si μ-cones/Co-P photocathodes do not require formation of a homojunction or emitter layer. Use of surface passivation and/or a homojunction on the Si μ-cone arrays could thus improve the efficiency while retaining the benefit of high light absorption in Si μ-cones. Si μ-cones with < 100 cm/s surface passivation can in principle produce E_{oc} > 650 mV [31, 32] and membrane-embedded μ-cones absorb > 90% of the light relative to their on-substrate counterpart. Polymer-embedded Si μ-cone arrays could thus produce $-J_{ph}$ > 25 mA cm^{-2}. Under standard conditions, HI splitting requires a minimum voltage of ~ 0.53 V, so utilizing a highly active catalyst such as Pt for the HER, along with improving the current collection, could lead to, flexible membrane-embedded photocathodes for HI splitting potentially reaching η_{IRC} > 10%. Electrodes in this work had a nominally equal density of μ-cones per unit area as that used in prior studies of μ-wires [7, 8, 38, and 39]. Future studies should investigate whether the light-scattering ability of μ-cones allows devices with reduced filling fractions to achieve comparable current densities, thereby relaxing the required ion current

density through the membrane. Future water-splitting photoelectrodes utilizing Si μ-cones could be implemented as a tandem junction with a wider band gap material deposited on the tips of the cones, in a similar fashion to previous studies that used a "Q-tip" design on Si microwire arrays [193, 194]. The improved light trapping in μ-cones can thus be beneficial in designing the current-matched top junction of a full fuel-forming photoelectrode system.

5.4 Conclusion

High photocurrent densities were exhibited by n^+p-Si/Pt and p-Si/Co-P μ-cone array photocathodes when either Pt or Co-P hydrogen-evolution catalysts were deposited over tips of the μ-cones. N^+p-Si/Pt μ-cone array photocathodes yielded an average η_{IRC} of 5.7%, and champion n^+p-Si/Pt μ-cone devices yielded η_{IRC} = 7.4%. Thick (~16 nm) Pt and Co-P layer deposited onto Si μ-cone arrays produced only a 6% reduction in photocurrent density compared to bare photocathodes having the same morphology and microstructure. However, the Si μ-cone arrays exhibited photovoltages that were lower by > 100 mV than the photovoltages obtained on planar or μ-pyramidally textured Si photocathodes. The photovoltage of the Si μ-cone arrays may be improved by optimizing the homojunction doping distribution. Greater than 90% of the incident light is absorbed in the μ-cones, as opposed to by the p-Si substrate at the base of the μ-cones [31, 32], so removal of the μ-cones from the substrate will result in confinement of light in an effectively thin silicon that will allow higher photovoltages to be achieved from the μ-cone arrays provided that surface recombination can be minimized [185]. The p-Si/Co-P devices showed an average open-circuit voltage of 331 mV vs RHE without an emitter, which, in combination with the high photocurrent densities of J_{ph} = -32 mA cm^{-2}, resulted in η_{IRC} = 3.1%. Si μ-cones were also embedded in a flexible polymeric membrane, allowing for high catalyst loadings with minimal losses in photocurrent due to catalyst obscuration in such systems.

Chapter 6
Broadband Light Transmission Using Dielectric Nanocones

6.1 Introduction

A universal strategy for designing ‘perfect’ antireflection coatings for an arbitrary broadband spectral range is highly desirable in many opto-electronic systems. Maximizing the broadband absorption is a fundamental requirement for high efficiency solar energy conversion devices like photovoltaics (PVs)[195-199], and photoelectrochemical cells (PECs)[87, 200, 201]. Many light trapping strategies such as anti-reflection coatings (ARCs)[19], surface texturing[54, 202-204], and high index light trapping structures[18, 205] were previously utilized for improving absorption in solar cells. In all the above cases solar cells require front metal contacts which induce shading losses[206]. All back contact design[23, 207] was previously utilized to prevent contact shading losses in crystalline Si solar cells, but such a design is not applicable to multi-junction solar cells that are typically utilized in space[208], and high efficiency photoelectrochemical cells (PECs) for solar fuels[209-211]. In PECs, light blocking metal catalysts are often employed over light absorbing semiconducting materials to overcome the kinetic barrier and overpotential losses to produce fuels at high efficiencies. Therefore, a general-purpose light management scheme that can incorporate thick and nontransparent metal contacts or catalysts while minimizing light obscuration has the potential to significantly increase the efficiencies of a wide range of device architectures.

Dielectric nanostructures for broadband absorption in semiconductor devices are explored for many optoelectronic applications. These structures include nanowires,[67, 212, 213] inverted pyramids,[214] nanodomes,[215] nanoshells,[216] nanospheres,[217] nanopillars,[218, 219] and nanocones.[220] For many of these structures, electrical conductivity at the interface is achieved by depositing transparent conducting materials, such as sputtered indium-doped tin oxide (ITO). Nanostructured Si was shown to reduce angular and spectrally-averaged reflectivity through an

opaque and highly-conductive front-side metal contact with high surface coverage. [219] Patterned Au films on Si were used for metal-assisted chemical etching, resulting in square Si nanopillars with small aspect ratios. Together with a 50 nm SiN_x antireflection coating, this structure displayed very high absorptance (> 90%) in both simulation and experiment, while achieving high surface conductivity across the 16 nm Au film that covered 65% of the Si surface.[219] However, the selective etching process limits this approach for use on very few interfaces like Au-Si, and precludes use on other device designs. Dielectric nanostructures with processing decoupled from other device components, and which do not require modification of the underlying semiconductor or contact interfaces, could increase the efficiencies of many planar PV and PEC devices.

It is previously demonstrated that Si microconical arrays achieve near perfect angular and spectrally averaged reflectivity of < 1 %, and absorption of 89.1 % in 400 – 1100 nm wavelength, and $0^O – 50^O$ angular ranges [31]. It is also demonstrated that sparse nanoconical arrays of InP demonstrate optical absorption that is broadband (450−900 nm), angle-insensitive, and near-unity (>90%) [184]. The conical architecture allows various wavelengths of light to couple to the available waveguide modes enabled due to multiple available radii [183]. Therefore, the conical shape provides the ideal geometry for the design of "perfect" broadband absorbers and the top and bottom radii can be chosen specific to the broadband of interest. Therefore, a novel solution to the issue of metal obscuration in planar devices is to guide light directly to the light absorbing material using an array of dielectric nanocones placed on the semiconducting surface. Coupling into waveguide modes of high-index dielectric nanocones allows confinement of incoming light, bypassing opaque metal films on the surface of planar devices. Such a versatile light management scheme could allow a large increase in conductivity of front-side metal contacts.

Waveguide designs require a high-index material that can be deposited on planar surfaces using scalable methods. For fully-integrated PEC devices, this material must display chemical stability in aqueous environments. TiO_2 was utilized extensively to protect high efficiency PEC devices in highly corrosive environments due to its chemical inertness and a high bandgap that allows for incident solar illumination to pass through [209-211, 221-225]. TiO_2 has a higher index compared to many other dielectric materials, and was previously utilized for increased coupling of light into waveguide modes [226-231]. Compared to dielectrics such as SiO_2 or Al_2O_3 that are typically utilized in solar cells, TiO_2's high index provides a higher index contrast in water, therefore making

it more applicable for light trapping in photoelectrochemical devices. Therefore, TiO_2 is an ideal choice material for coupling of light to waveguides in nanocones. Ni metal is widely used as an earth abundant catalyst for oxygen evolution reaction (OER) which is an important part of both water splitting [209, 232, 233], and CO_2 reduction devices [210], therefore in this study we utilize Ni metal as the front contact deposited between hexagonally-packed TiO_2 nanocones on Si.

6.2 Optical Simulation Results

3D full-field electromagnetic wave finite difference time domain (FDTD) simulations of TiO_2 nanocone arrays and/or Ni hole arrays on Si were performed using a commercial software package, Lumerical FDTD. The nanocone arrays on Si were constructed using the 3D simulation region with periodic boundary conditions along *x*- and *y*-axes, and infinite boundary conditions rendered as perfectly matched layers along the *z*-axis. Palik materials data was used for Si and Ni. Material data from the Ioffe Institute's is utilized for simulation of TiO_2 nanocone optical properties. A plane wave illumination source was utilized to simulate steady state behavior of TiO_2 nanocones and/or Ni arrays on Si substrate. Broadband simulations were performed in the 400 – 1100 nm broadband regime for two orthogonal polarizations. The unpolarized transmission spectra shown in Figure 1 were obtained by averaging the transmission spectra of both the orthogonal polarizations. These transmission spectra along with AM 1.5G were utilized to calculate the fraction of spectral photon flux that is transmitted into Si and thus the expected short circuit current density. Frequency-Domain Field and Power monitors were utilized to collect the steady state electric field data for plotting electric field profiles to understand the wave guiding properties.

Figure 6.1 (a) – (c) show the schematics of the 3 different device configurations that were used to understand the optical properties of TiO_2 nanocones. In (a) TiO_2 nanocones that are placed over the Si substrate, in (b) Ni is incorporated between the nanocones covering all the exposed Si surface, and (c) shows the configuration with the same amount of Ni covering the Si surface but without the TiO_2 nanocones. The bottom radius of the nanocones was chosen as 250 nm, and the height as 2300 nm. The nanocones are arranged in a 2D hexagonal lattice with 700 nm pitch. The Ni is chosen to be 50 nm thick, which was much higher than the typically used (2-5 nm) in case of oxygen evolution photoanodes [209]. Ni covered about 46.3% of the front surface.

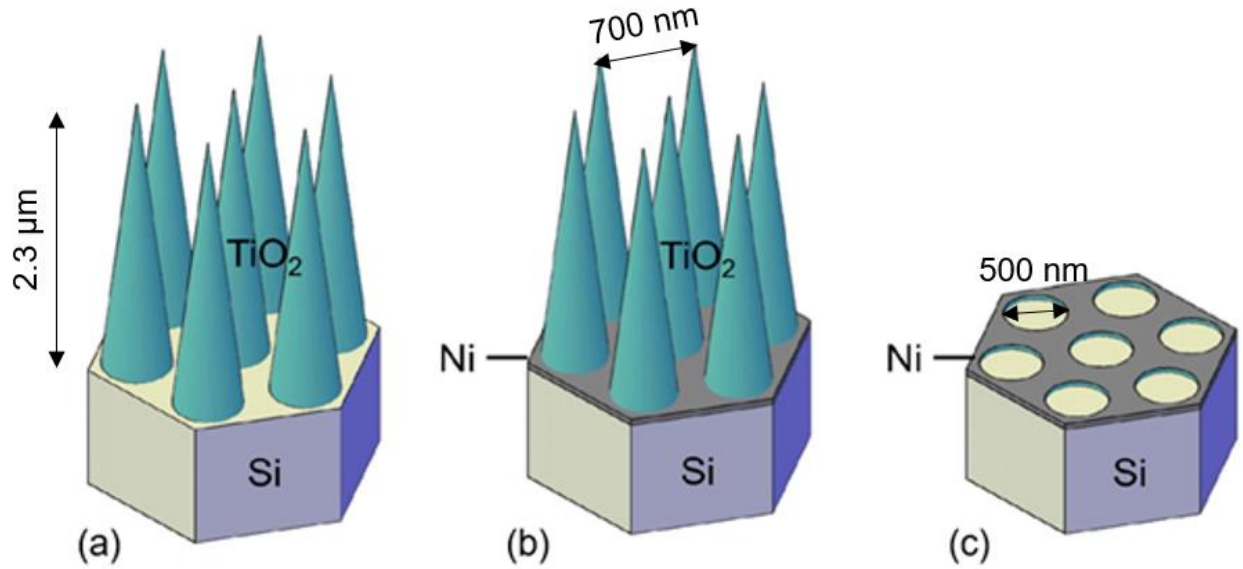

.

***Figure 6.1**: (a), (b), and (c) show the schematics of the three configurations that are simulated*

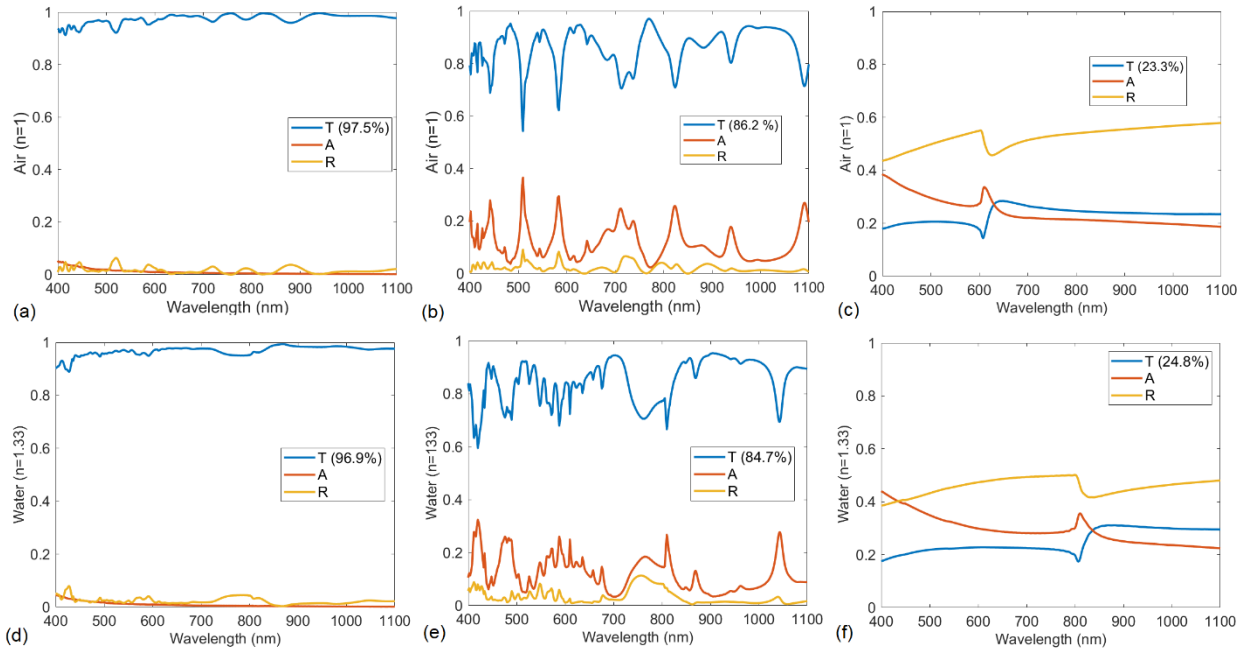

***Figure 6.2**: Simulated transmission (T), absorption (A), and reflection (R) spectra of the three configurations in Figure 6.1. (a), (b), and (c) plots the spectra in air for TiO_2 cones on Si, TiO_2 cones on Si with Ni, and Ni hole array on Si respectively. (d), (e), and (f) plot the same in water.*

Figure 6.2 plots the transmission, absorption, and reflection spectra for the three cases in Figure 6.1 in air and water. The simulations were performed with a background index of n = 1 and n= 1.33 to understand the behavior in air and water respectively. Figure 6.2 (a) and (d) show that the TiO_2 nanocones act as an excellent broadband antireflection structures that can enable 97.5%, and 96.9% of the total number of photons in 400 nm – 1100 nm range in air and water respectively. When 50 nm of Ni was incorporated into the space between the nanocones over the Si substrate the transmitted photon flux was reduced to 86.2%, and 84.7% in air and water respectively. Compared to the structure in Figure 6.1 (c) with no nanocones and same amount of Ni loading as Figure 6.1 (b) the transmitted photon flux was 23.3% and 24.8% in air and water respectively. Therefore, the TiO_2 nanocones enable transmission of more than 3 times the amount of light to pass through in this specific configuration. In case of Ni hole array, the reflection and parasitic absorption account for above 75% of optical losses, whereas when coupled with TiO_2 nanocones the total loss was < 15 % indicating that the TiO_2 nanocones are enabling the light to be transmitted into the Si substrate below Ni with minimal interaction with Ni. Figure 6.3 plots the transmitted photon flux data along with AM 1.5 spectrum using which the percentage of transmitted photon flux was calculated.

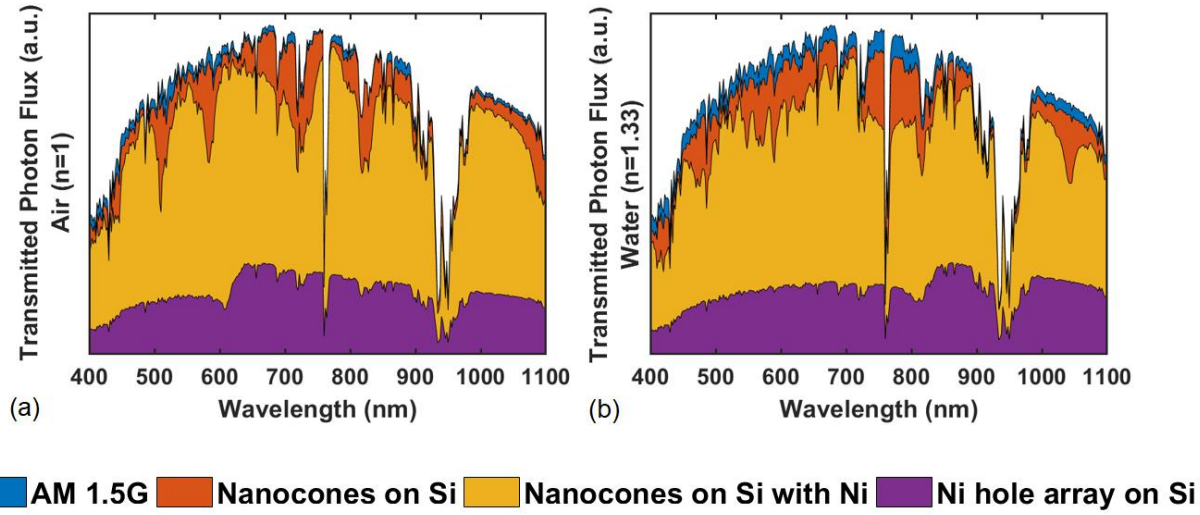

***Figure 6.3**: Area plot of simulated transmitted spectral photon flux in air and water for the three configurations in Figure 6.1. Blue represents AM 1.5G spectral photon flux. Orange, yellow, and purple plot the transmitted spectral photon flux into Si for nanocones on Si, nanocones with Ni on Si, and Ni hole array on Si respectively.*

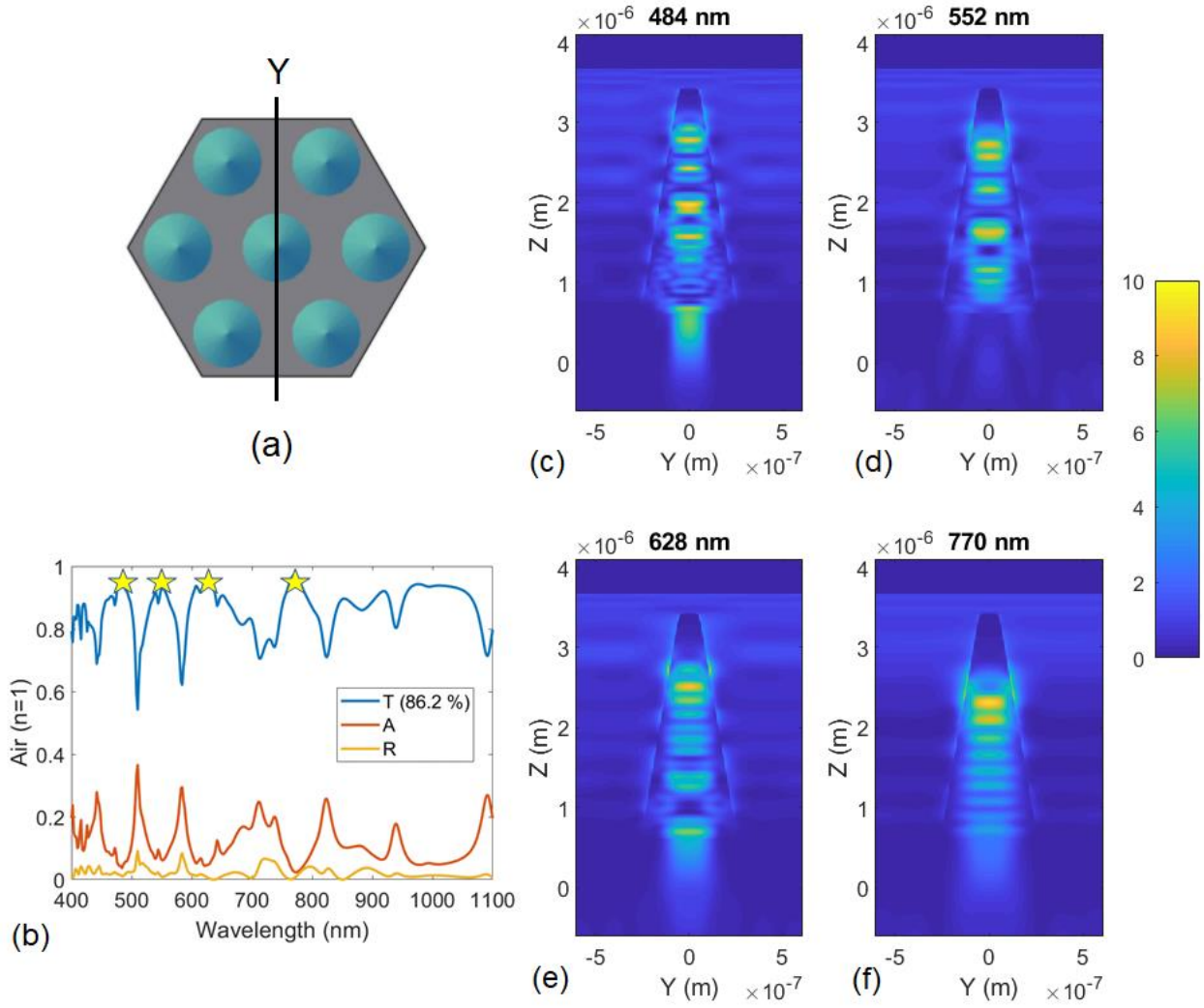

***Figure 6.4**: (c), (d), (e), and (f) show the electric field profiles along the cross section shown in (a) at maxima in transmission spectrum into Si with TiO_2 nanocones and Ni in air. The selected wavelengths are highlighted using the yellow stars in (b).*

To understand the interactions of light with TiO_2 nanocones, frequency domain field and power monitor was utilized to record electric field data in FDTD simulations. Figure 6.4 plots the electric field profiles along a nanocone cross section as shown in Figure 6.4 (a). In Figure 6.4 plots the field profiles at wavelengths 484 nm, 552 nm, 628 nm, and 770 nm. These wavelengths correspond to the maxima in transmission spectra into Si with TiO_2 nanocones and Ni as shown in Figure 6.1 (b). It can be observed that most of the electric field is confined in the nanocone. Strong coupling of incident light occurs at different radii for different wavelengths as expected from a nanoconical

structure [31, 183, 184]. The light propagates in the nanocone and is transmitted into the Si substrate below, where decay in field intensity can be observed due to absorption.

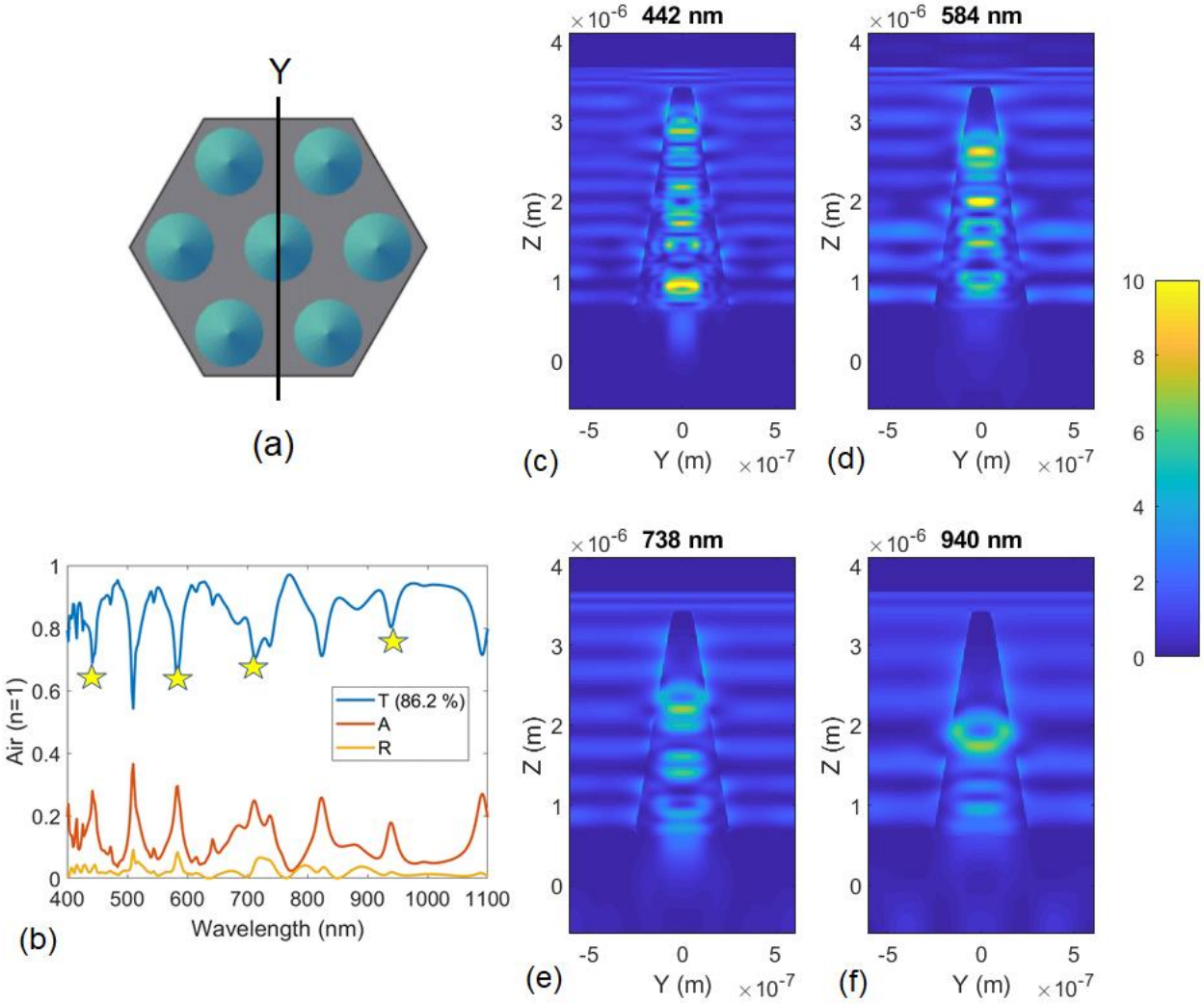

***Figure 6.5**: (c), (d), (e), and (f) show the electric field profiles along the cross section shown in (a) at minima in transmission spectrum into Si with TiO_2 nanocones and Ni in air. The selected wavelengths are highlighted using the yellow stars in (b).*

Similar plots are shown in Figure 6.5 and this time the wavelengths 442 nm, 584 nm, 738 nm, and 940 nm are chosen from the minima of the transmission spectrum. Compared to field profiles in Figure 6.4 the profiles in Figure 6.5 show a higher intensity of electric field in the middle of the nanocones. The minima in transmission spectrum primarily correspond to absorption peaks in Ni and these peaks shift depending on the background index as shown in Figure 6.2 (b) and (e).

The field profiles in Figure 6.5 show that even at the minima, the transmission is 60 % or above, which is still higher compared to the transmission spectra in case of Ni hole array on Si without TiO_2 nanocones as shown in Figure 6.2. This indicates that the incident light couples efficiently to the nanocones which guide the light into the underlying Si substrate. Depending on the slope of the nanocone, electric field associated with some wavelengths of the light are highly confined inside the TiO_2 nanocone while some wavelengths are partially confined. Absorption in Ni is enhanced when the light is not completely confined inside the nanocones causing a potential photocurrent loss. Using the transmitted spectral photon flux, it can be estimated that in air the maximum photocurrent that is achievable in Si with TiO_2 nanocones, in Si with TiO_2 nanocones and Ni, and in Si with Ni hole arrays is 42.9 mA cm^{-2}, 37.9 mA cm^{-2}, and 10.9 mA cm^{-2} respectively. In water the photocurrent respectively corresponds to 41.8 mA cm^{-2}, 36.5 mA cm^{-2}, and 10.7 mA cm^{-2}. Therefore, incorporation of Ni in between TiO_2 nanocones results in ~ 5 mA cm^{-2} photocurrent loss but compared to a Ni hole array with no TiO_2 nanocones the photocurrent enhancement was > 300%. This behavior of TiO_2 nanocones cannot be explained using effective medium theory and wave-optic simulations show that the nanocones act as an antenna for the incoming radiation, coupling the light to the waveguide modes and providing a route for the light to reach underlying Si substrate despite 54 % of the surface being covered by Ni.

6.3 Fabrication of TiO_2 nanocone photoanodes

Czochralski-grown n-type Si wafers with <100> orientation and resistivity 0.1-1 ohm-cm (Addison Engineering Inc.) were cleaned via modified RCA standard clean 1 (5:1:1 H_2O:NH_4OH:H_2O_2 at 70 °C) followed by an RCA standard clean 2 (6:1:1 H_2O:HCl:H_2O_2 at 70 °C) sandwiched between 1 min dips in 10% (v/v) HF. Thermal boron (B) doping was performed to obtain an p^+n Si homojunction using BN-975, B doping source from Saint-Gobain at 950 ^{0}C for 30 mins. Low temperature oxidation was performed in a tube furnace at 750 ^{0}C for 20 mins with 2 min dip in 10% (v/v) HF before and after the growth to remove defective layer on the Si surface. 5 – 10 nm of SiO_2 was deposited via electron beam evaporation prior to 2.3 µm of TiO_2 was evaporated onto p^+n Si wafers via electron beam evaporation. The 5 – 10 nm SiO_2 electrically isolated the TiO2 from making an electrical contact to the SiO2 surface without any affect over the optics. Electron beam evaporation depletes the source of oxygen and becomes more conductive; therefore, the deposition

was performed in 3-4 steps while refilling the TiO_2 source to maintain higher oxygen content. 495 PMMA A4 and 950 PMMA A4 layers were spin coated sequentially over p^+n Si homojunction samples with 2.3 µm TiO_2 at 4000 rpm for 60 s with post baking at 80°C for 5 minutes to form bilayer of positive tone resist for easier lift-off. Direct electron beam lithography system (VISTEC electron beam pattern generator (EBPG) 5000+) at an acceleration voltage of 100 keV with a current of 5 nA was utilized to pattern the 100 nm diameter circular hexagonal array with 700 nm pitch size. After electron beam writing the samples were developed in MIBK (methyl isobutyl ketone) : IPA solution for 60 s at room temperature resulting in 100 nm diameter holes with 700 nm pitch in a hexagonal array in the PMMA layers. 200 nm of Cr was evaporated over these samples and lift-off was performed in acetone resulting in a hexagonal array of Cr that served as a hard mask for TiO_2 dry etching. Dry etching was performed using Oxford instruments plasma lab system 100 ICP-RIE using SF_6 / C_4F_8 etch chemistry, where SF_6 was the etching gas and C_4F_8 was the passivating gas. Etching was performed at a capacitively coupled power of 150 W, inductively coupled power of 2500 W, SF_6 / C_4F_8 gas ratio of 23.5 sccm / 40 sccm, chamber pressure of 7 mTorr, and table temperature of 0^0 C for 15 mins. The SEM image of the resultant TiO_2 nancones is shown in the scanning electron microscope (SEM) image in Figures 6.6 (a) and (c). The resultant TiO_2 nanocone arrays were ~ 2.3 µm high with a bottom radius of ~ 250 nm. The tips of such nanocones ended up being not as smooth as an ideal cone but did have < 50 nm top radius.

Electrodes were prepared using these samples by first cleaving the edges off to avoid shorts due to doped layers. In-Ga eutectic was applied on the backside to form ohmic contact with p^+n Si homojunction. Sn- plated Cu wire was attached to the In-Ga applied back side using Ag paste from Ted Pella. The samples were sealed to a glass tube with the wire running through it using epoxy (Loctite 9460), and annealed at 80 ^{0}C for ~ 6hrs. The Ni catalyst was electrodeposited in between TiO_2 nanocones soon after the sample was dipped in buffered HF (40% NH_4F to 49% HF volume ratio 6:1) for 10s using a commercially available Ni plating solution (Clean Earth Nickel Mirror, Grobet USA) at a potential of -0.956 V vs Ag / AgCl using Biologic SP-200 potentiostat until ~ 300 mC cm^{-2} charge was passed. Since the TiO_2 nanocones were electrically isolated using thin SiO_2, Ni was preferentially deposited in between the TiO_2 nanocones on the Si substrate with an increased concentration closer to the cone as shown in Figures 6.6 (b) and (d). The Ni deposition was uniform over a sample size of ~ 0.04 cm^2.

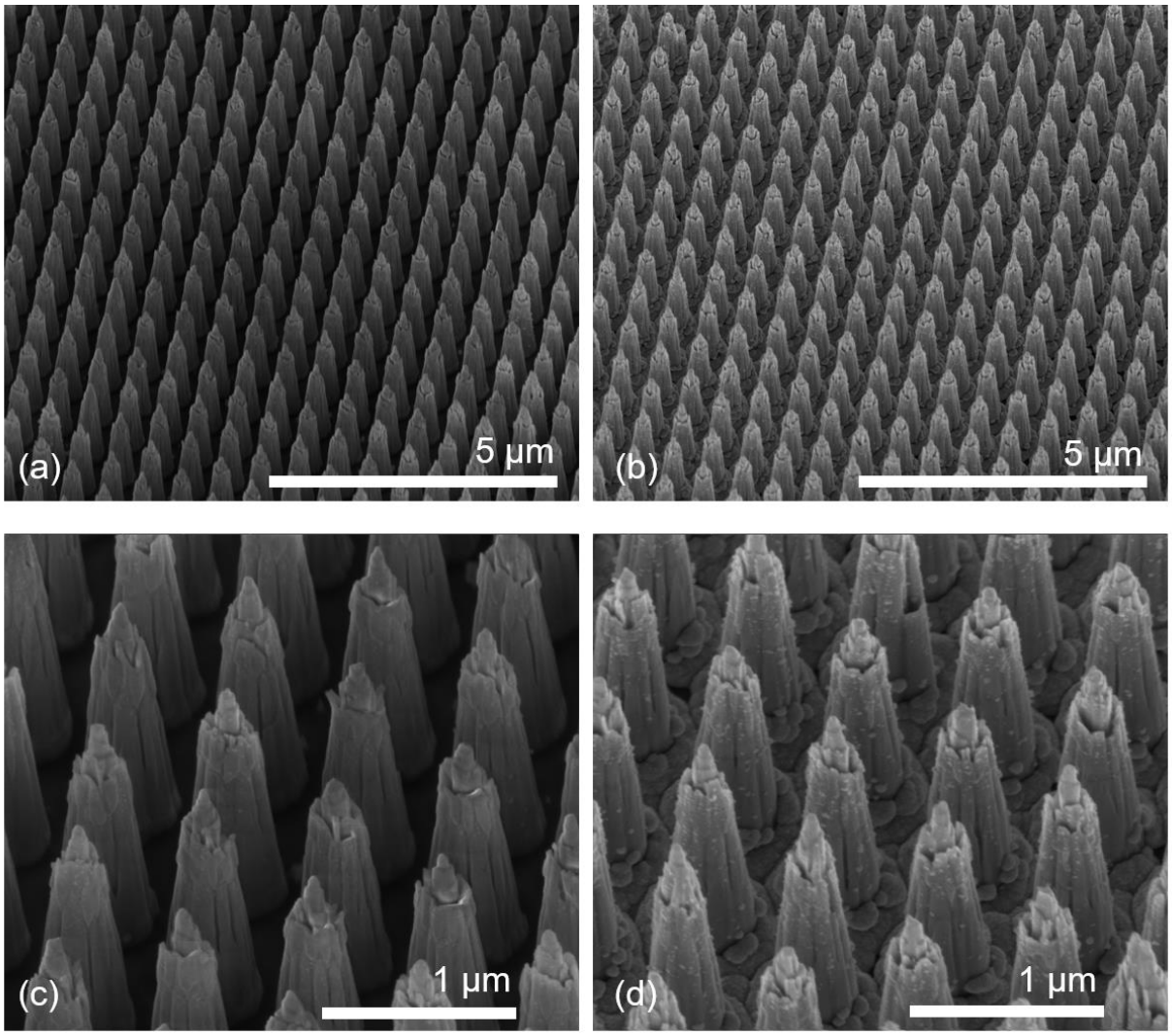

Figure 6.6: *(a) and (c) show the SEM images of TiO2 nanocones prior to Ni electrodeposition, and (b) and (d) show the SEM images taken after Ni electrodeposition.*

6.4 Optical and electrochemical measurements

The reflective index n, k of TiO_2 was characterized using ellipsometry (J.A. Woollam Co. model VASE). The real part of refractive index for evaporated TiO_2 was considerably lower compared to the ideal TiO_2 data from ioffe institute as shown in Figure 6.7. In order to estimate the expected photocurrent from as prepared sample, optical simulations were performed using the refractive index data of evaporated TiO_2. The transmission, absorption, and reflection spectra in this case are plotted

in Figure 6.8 (a) and are plots for transmitted photon flux are plotted in Figure 6.8 (b) for the three scenarios as in Figure 6.1.

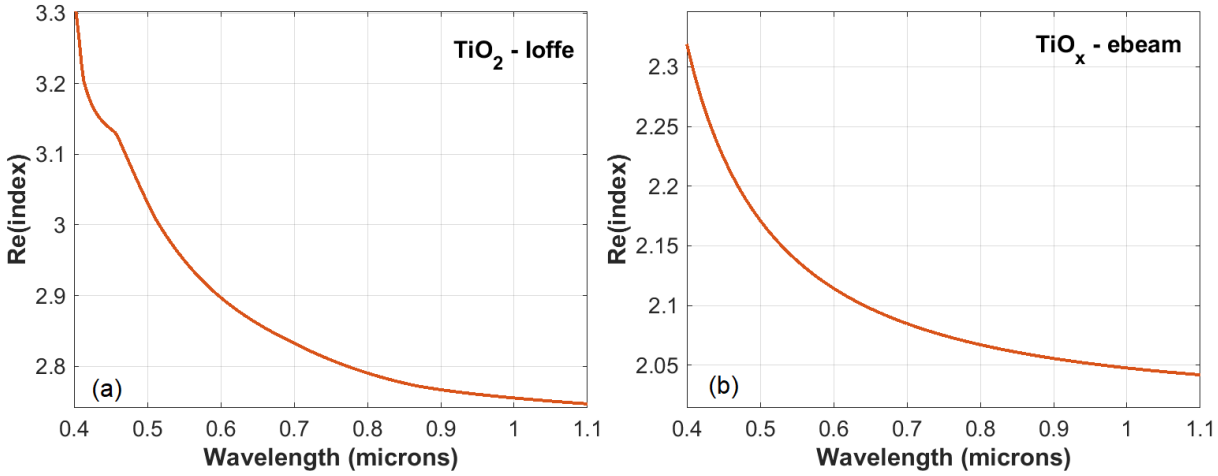

***Figure 6.7**: Real part of refractive index for ideal TiO_2 is shown in (a), and of electron beam evaporated TiO_2 in (b).*

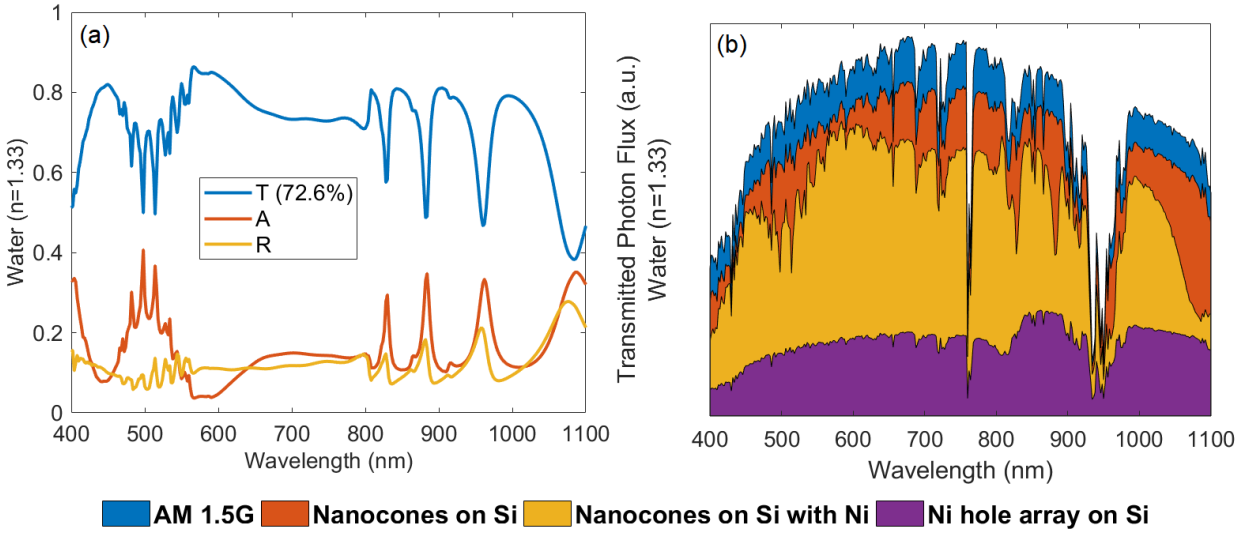

***Figure 6.8**: Transmission (T), absorption (A), and reflection (R) plot for Si with TiO_2 nanocones and 50 nm Ni calculated with evaporated TiO2 refractive index data us shown in (a). (b) shows the area plot overlapped over AM 1.5G spectrum for the three different cases as shown in Figure 6.1 with evaporated TiO_2 refractive index data.*

The expected photocurrent calculated utilizing evaporated TiO_2 refractive index data after correcting for reflection losses from air/glass/water interfaces that are unavoidable in an electrochemical testing setup is ~ 29.8 mA cm^{-2}. This value is significantly lower than in the case of ideal TiO_2 but is slightly higher than ~ 28 mA cm^{-2} that is expected from a bare flat Si surface.

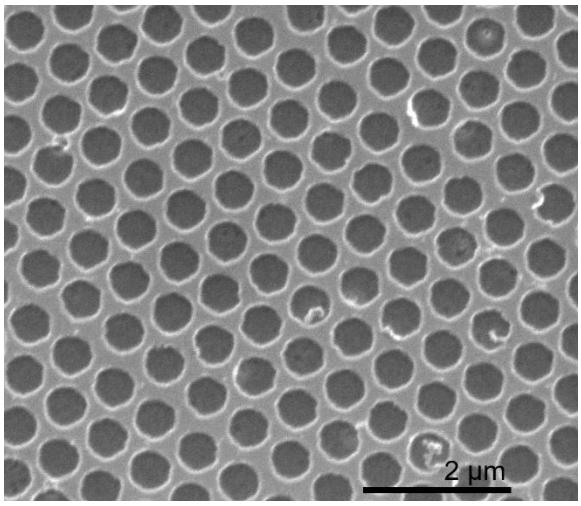

***Figure 6.9**: SEM image of the Ni hole array fabricated via electron beam patterning and dry etching of 50 nm thick Ni layer. Average diameter of the holes is ~ 500 nm. Image taken by Wen-Hui Cheng*

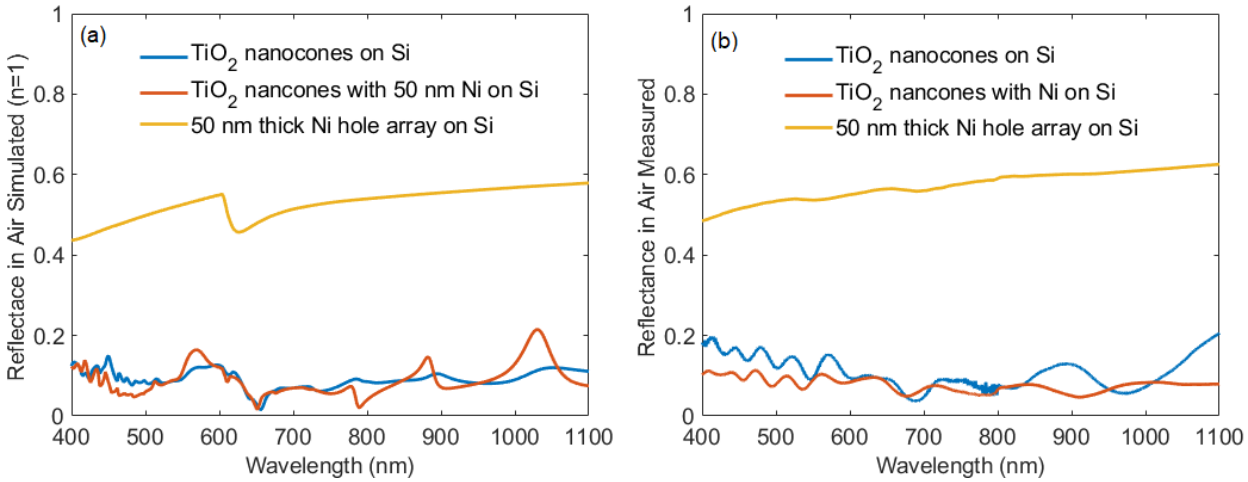

***Figure 6.10**: (a) and (b) show simulated and measured reflectance of Si with TiO_2 nanocones, with TiO_2 nanocones and Ni, and with Ni hole array respectively*

Reflectance measurements were done on the Si with TiO_2 nanocone samples before and after Ni deposition for the ones shown in Figure 6.6, along with a Ni hole array prepared via electron beam patterning of PMMA over a 50 nm Ni sputtered Si sample. Figure 6.9 shows the SEM image of the patterned Ni hole array used for reflectance measurement. Figure 6.10 (a) and (b) plot the simulated and measured reflectance spectra taken using Cary 5000 UV-VIS spectrometer. The experimental and theoretical nominally match in order of magnitude. Simulations were done under a coherent illumination whereas the experimental measurement wasn't, and the TiO_2 nanocones and Ni as can be seen in the SEM images in Figure 6.6 are not perfect cones and perfectly flat layers respectively. Therefore, the simulated and measured experimental spectra have different features.

Photoelectrochemical oxygen evolution reaction (OER) was performed using photoanodes fabricated as discussed in previous section. A three-necked glass cell incorporated with quartz window was utilized as a vessel for this experiment. The OER performance using a three-electrode setup in 1 M KOH (Sigma-Aldrich) using a saturated calomel electrode (SCE) as a reference, carbon as a counter electrode, and the p^+n Si sample with TiO_2 and Ni as the working electrode. Measurements were done under simulated sunlight in Oriel Instruments Solar Simulator equipped with a 1000 W Mercury Xenon lamp calibrated to 100 mA cm^{-2} illumination using a Si photodiode. The active area of the working electrodes was measured using image processing software ImageJ from a high-resolution image taken using a scanner. Typical electrode areas were ~ 0.04 cm^2. The voltage was swept from -0.5 V to 1.5 V relative to SCE at a scan rate of 50 mV s^{-1} for current-voltage (*J-V*) measurement.

Figure 6.11 plots the OER *J-V* characteristics on a p^+n Si surface with TiO_2 nanocones and 300 mC cm^{-2} electrodeposited Ni. 300 mC normalized to the exposed Si area between nanocones is equivalent to ~ 70 nm of flat Ni layer which is slightly higher than the 50 nm utilized in the simulations. The photocurrent calculated at ~ 1 V vs SCE by subtracting the dark current from light current was ~ 28 mA cm^{-2} matches well with the estimate using simulations. Despite the evaporated TiO_2 having a much lower refractive index than an ideal TiO_2 a photocurrent of ~ 28 mA cm^{-2} can be achieve. The magnitude of observed photocurrent is similar to what one would expect when the Si surface is completely bare. This shows that the TiO_2 nanocones act as antireflective structures that can couple to the incoming light and enable transmission of light into the underlying Si light absorber in this case even when ~ 54 % of the surface was loaded with thick Ni layer.

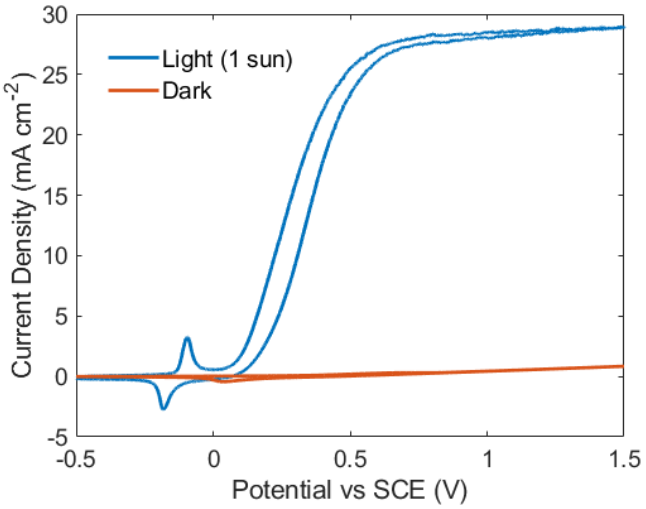

***Figure 6.11**: J-V charectorisitcis of p^+n Si homojunction photoanode with TiO_2 nanocones and 300 mC of electrodeposited Ni performing OER in 1 M KOH in dark and under 1 sun simulated illuminations*

6.5 Conclusion

In conclusion an alternative light trapping scheme utilizing dielectric nanocones was demonstrated. The nanoconical shape of dielectric structures efficiently couple incoming light to available waveguide modes and enable transmission into light absorbing semiconducting substrates even when ~ 54 % of the front surface of the absorber was coated with light blocking catalysts. Proof of concept simulations and experiment were performed using TiO_2 nanocones over Si substrate with Ni as the light blocking catalyst. A photocurrent of ~ 28 mA cm^{-2} was observed using non-ideal TiO_2 towards OER reaction at 1 sun in 1 M KOH electrolyte. Simulations show that using an ideal TiO_2 material with a higher refractive index can provide photocurrents up to 37.8 mA cm^{-2} in air and 36.5 mA cm^{-2} in water under a 50 nm thick Ni coverage of 54 % Si surface. Since this effect depends primarily on optical constants of the materials similar photocurrent enhancement is expected from other light absorbers if used in place of Si. Therefore, incorporating high index dielectric nanocones over planar monolithic photoelectrochemical devices could enable incorporation of high loadings of highly active catalysts to enable higher efficiencies and longer stability.

Chapter 7
Effectively Transparent Contacts (ETCs) for Solar Cells

7.1 Introduction

Silicon (Si) based solar cells dominate the current photovoltaic market. The price decline in Si based solar modules has resulted in the balance of systems cost dominating the cost of solar installations [234]. Si based solar cell technology is very mature and laboratory efficiency record is currently at 26.7 % [23], which is very close to the theoretical maximum of 29.43 % [17]. This record efficiency device utilizes Si heterojunction technology which is composed of high lifetime crystalline Si wafer coated with thin amorphous Si films that result in extremely low surface recombination, and selective carrier collection, therefore resulting in very high open circuit voltages. This device also employs interdigitated back contacts (IBC) in order to reduce front surface reflection losses due to front metal contacts to maximize the photocurrent. Most commercial solar panels do not employ IBC design due to cost constraints and thus suffer from front contact reflection losses. The surface coverage of metallic contacts is typically ~ 6 %, but some of the reflected light from contacts is harvested utilizing total internal reflection from front surface of cover glass. Transparent conducting oxides (TCOs) are employed as an alternative for front metal contacts, but they suffer from reduced conductivity, and increased parasitic absorption losses, and thus decrease the efficiency. One solution for mitigating the front contact reflection losses is by modifying the shape of contacts. In this chapter a triangular shape to the front contacts is explored. These triangular silver contacts were shown to demonstrate 99.9 % transparency rendering them effectively transparent [191]. These contacts are employed over Si heterojunction solar cells as proof of concept demonstration. Finally, a fabrication method for various configurations of triangles is demonstrated opening up new avenues to utilize these contacts over various other solar cell technologies, opening the door to a potential way to set new efficiency records.

7.2 ETCs on planar Si heterojunction solar cells

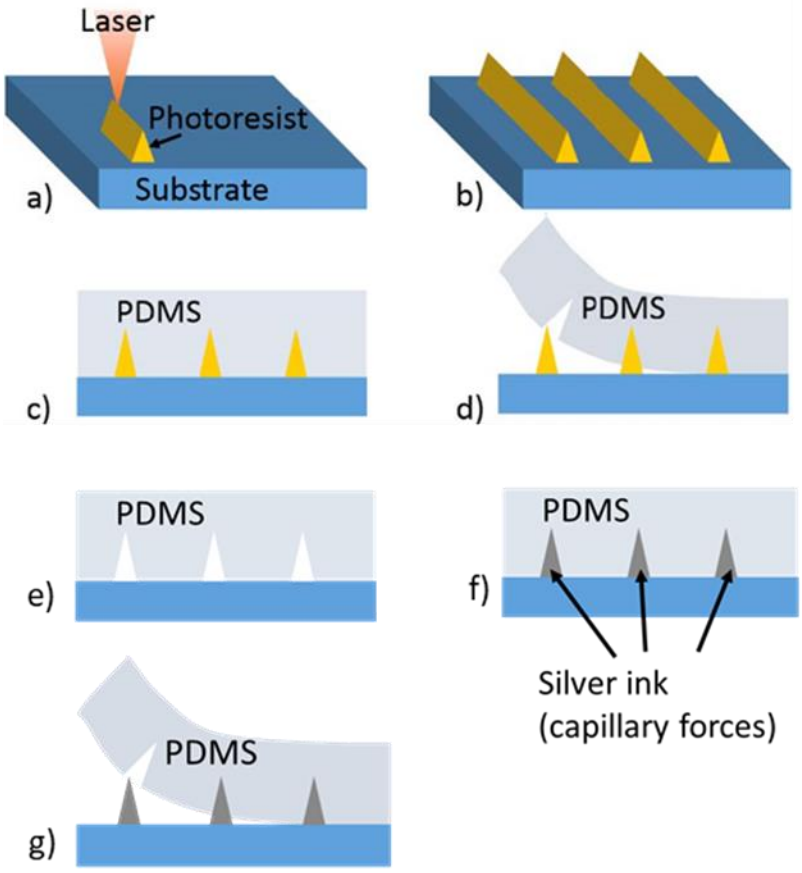

***Figure 7.1**: Schematic for fabrication process of effectively transparent contacts. (a) shows the fabrication of triangular master as shown in (b) via 2-photon lithography. (c) shows the casting of PDMS over the master, which results in PDMS stamp after curing as shown in (d). The PDMS stamp is applied over solar cell substrate as shown in (e). Silver ink is applied to the sides of the stamp resulting in flow onto the substrate via capillary forces as shown in (f). After heating the at 60^{o}C the stamp is peeled off resulting in silver triangles over the solar cell. Image credit: Rebecca Saive*

The fabrication procedure for fabrication of silver triangles over a solar cell is shown in Figure 7.1. Effectively transparent contacts were prepared using imprint lithography. Using two-photon lithography triangular cross section polymer lines were written on silicon substrates. The width of the triangle was 4.5 µm, height 15 µm and period 80 µm. The lines were written to be up to 10 mm

long. These samples were used as a mold for the preparation of a PDMS stamps. The PDMS stamps were cut open on both sides of the line grid and put in isopropanol for 6–12 hours in order to obtain a favorable surface energy. Then, the stamp was placed on the ITO patch of the solar cell and silver ink was infilled from the sides via capillary action. This process ensured clean triangular cross-section silver lines without unwanted silver residues between the lines. The samples were then annealed ~200 ^{O}C for a few minutes to make the silver ink in the triangular lines conductive. As prepared triangular contacts had a sheet resistance of 4.8 Ω sq^{-1}.

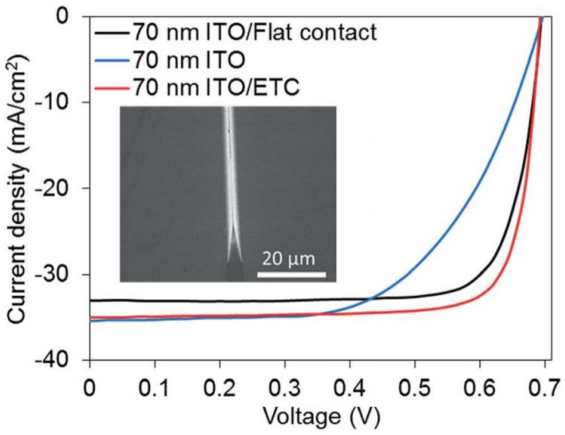

***Figure 7.2**: Current–voltage characteristics of silicon heterojunction solar cells with three different front contact. Inset: scanning electron microscope image of a triangular cross-section contact line.*

For proof of concept demonstrations, the ETCs were employed over silicon heterojunction cells. Silicon heterojunction (SHJ) solar cells were prepared in the same way as described by S. Y. Herasimenka [235]. The solar cells had textured back surfaces and flat front surfaces and were fabricated on 270 mm thick 4-inch wafers. These cells were cut to 1.4 cm x 1.4 cm pieces and 7 mm x 7 mm ITO patches defined the active area. ITO layers were 70 nm thick. Three different contact layouts were compared against each other: (i) an ITO layer with a flat metal grid of 6% surface coverage, (ii) an ITO layer without any metal contact and (iii) an ITO layer with effectively transparent contacts (ETCs). Figure 7.2 shows the current–voltage (J–V) characteristics of these three devices. The black curve shows the J–V characteristics of a cell with 70 nm ITO and a flat contact grid. The short circuit current density is 33 mA cm^{-2} and therefore, 2 mA cm^{-2} lower than the one of a cells with only the ITO layer and no metallic contacts (blue curve). This corresponds approximately to the 6% shading of the contact grid. The active area of the measured cells was 5

mm x 6 mm. Therefore, a metal contact grid is necessary to provide good lateral transport and cells with only ITO exhibited a low fill factor (59.3%) as can be seen from the blue curve. ETCs on top of the ITO layer (red curve) lead to short circuit current densities comparable to those for cells without any metal contact, which agrees with previously reported effective contact transparency of up to 99.9% [191]. Furthermore, fill factors of up to 80.7% were achieved. With a short circuit current density of 35.0 mA cm^{-2} and an open circuit voltage of 690 mV, this leads to an efficiency of 19.5 %, which is 1.4 % (absolute) higher than the cells with flat contacts. Table 7.1 compares the solar cell metric for the three cases shown in Figure 7.2.

	70 nm ITO / Flat Contacts	70 nm ITO	70 nm ITO / ETCs
V_{OC} (mV)	693	697	690
J_{SC} (mA cm^{-2})	33.0	35.4	35
FF (%)	79.0	59.3	80.3
η (%)	18.1	14.6	19.5

Table 7.1: *Summary of efficiency (η), open circuit voltage (V_{OC}), short circuit current (J_{SC}), and fill factor (FF) for silicon heterojunction solar cells with different contact layouts.*

7.3 ETC implementation over other solar cells

Currently the application of ETCs on solar cells was limited to solar cell technologies with a flat front surface that can withstand the annealing process of the silver ink. The ink utilized over Si heterojunction cells is a low temperature ink that needs to be annealed ~ 200 ^{O}C. For solar cells that may not withstand the high temperature annealing processes like perovskite-based ones, an alternative way of implementing the ETCs is by fabricating the cell over an ETC "superstrate". An ETC superstrate can be imagined as polymer with triangular gives on a glass handle for support, with the triangular groves filled with silver ink that is annealed prior to solar cell fabrication over it. Figure 7.3 shows the schematics of an ETC superstrate fabrication.

Implementing ETCs over textured Si solar cells which are the most widely used technology in the photovoltaics market has the potential to make ETCs a highly valuable technology. Printing ETCs over rough or textured Si solar cells is not trivial due to the ink leaking into areas in the middle of

triangular contacts resulting in more light blocking. Figure 7.4 shows one such attempt of printing ETCs over a rough (2 -3 µm surface roughness) Si solar cell. Metal contacts over Si homojunction cells are currently implemented utilizing screen printing. Such contacts are typically 30 – 50 µm wide. Any implementation of ETCs over these cells must be compatible with screen printing for the barrier of entry of ETCs into solar cell market is reduced. The superstrate way of implementing ETCs may have the potential to be applicable to very rough Si solar cells. Perovskite / Si tandems are being considered as a cheaper alternative way to improve the efficiency beyond the theoretical limit of Si solar cells. Therefore, being able to implement ETCs over the textured Si and perovskite solar cells may improve the light management and enable record efficiencies in a 4 terminal tandem device.

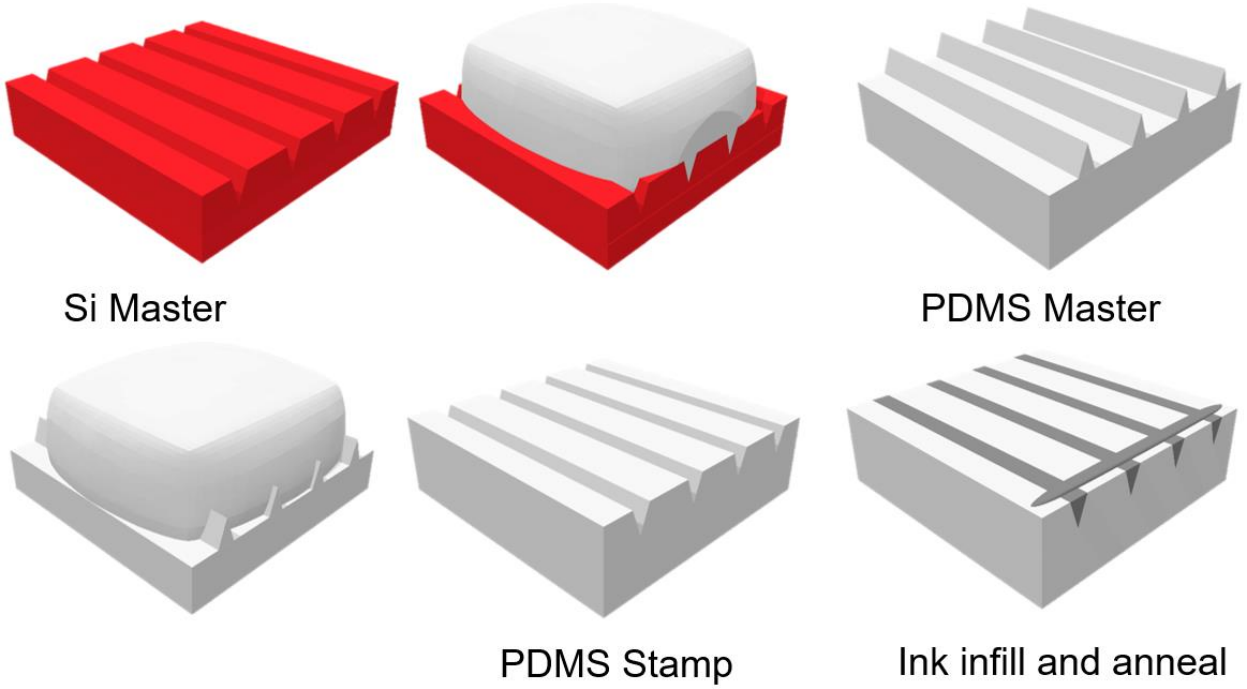

Figure 7.3*: Schematics of fabrication of an ETC superstrate staring from a Si master with triangular groves using PDMS. Figure credit: Sophia Coplin*

The proof of concept implementation of ETCs so far has utilized one specific configuration of 4.5 µm wide, and 15 µm high triangles with a spacing of 80 µm. It was shown recently that a dense array of ETCs over thin Si solar cells and the back of bifacial solar cell can improve the light trapping properties and lead to higher efficiencies [236, 237]. The fabrication of ETC masters via 2-photon lithography is very slow and not scalable to large triangle sizes that are ideal for a Si homojunction cell.

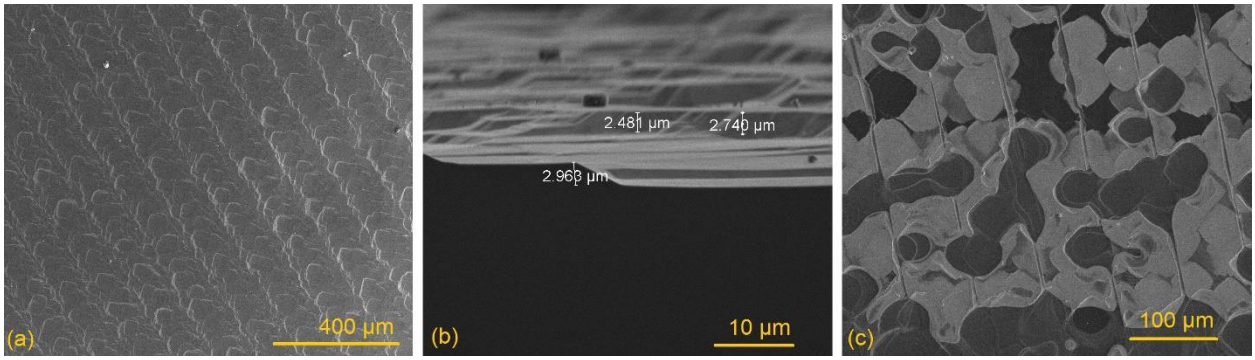

***Figure 7.4**: (a) and (b) show SEM images of the front surface of a rough Si homojunction solar cell recieved from UNSW. (C) shows the SEM image of an attempted ETC print on this rough surface resulting in Ag ink spillage all over the solar cell.*

Apart from solar cells the ETCs can also be very useful in photoelectrochemical devices. As mentioned in the previous chapter on Si microcone photocathodes the incorporation of metal catalyst onto semiconducting substrates is a very important issue in achieving high efficiencies in photoelectrodes. Ag is known for being able to act as catalysts for converting CO_2 into CO. Therefore, Ag triangles so far implemented over solar cells can be utilized as an "effectively transparent catalyst" for photoelectrochemical CO_2 reduction. Higher catalyst loadings typically improve the reaction kinetics as more sites become available for the reaction to take place. Therefore, in such a scenario increasing in the number of ETCs by reducing their spacing is very beneficial. In the following section the fabrication of ETC masters for a wide range of sizes, and spacings is explored keeping all these possibilities in mind.

7.4 Fabrication of Si masters for ETCs

Inductively coupled plasma reactive ion etching (ICP-RIE) was utilized for fabricating triangular structures and then triangular groves into a Si wafer. Typical procedure includes photolithographically patterning a Si wafer to expose areas for etch mask deposition. Al_2O_3 etch mask is chosen similar to the etching process for Si microcones as discussed in the earlier chapters. For fabricating triangular structures, the mask covered the areas where the triangular structure is to be formed, and for triangular groves mask was deposited over its inverse structure.

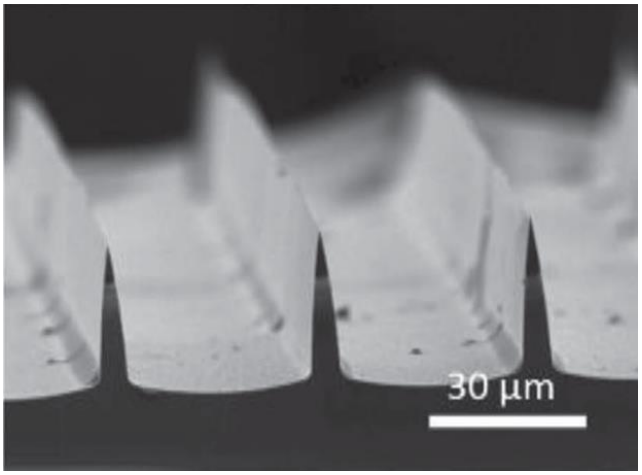

Figure 7.5*: SEM image of the triangular structure etched into a Si wafer for utilization as a master for making PDMS stamps for printing ETCs.*

Triangular shaped structures etched into Si wafer are shown in Figure 7.5. First, an etch mask composed of Al_2O_3 was defined by lithography. Then cryogenic ICP-RIE was performed using SF_6 as etching gas and O_2 as a passivation gas. The aspect ratio and taper of the triangular shaped lines etched into the silicon sample can be adjusted by varying the SF_6 / O_2 ratio in the plasma. Here we started with a line pattern with ~2.5 µm width and the etching was performed at 900 W of inductively coupled plasma power, 5 W of capacitive coupled plasma power, 70 sccm SF_6, and 9 sccm O_2 for 10 min at −120 °C. Post etching the samples were etched briefly in isotropic Si etch utilizing HF / nitric acid / acetic acid (HNA) to sharpen the triangle tips. These structures turned out to be not as applicable for ETCs due to the unavoidable curvature that can be observed at the bottom of triangles. When PDMS stamps were made from these structures the curvature causes ink to spill between the ETCs.

To overcome the ink bottom curvature related issues triangular groves can be etched into Si with Al_2O_3 mask covering all the areas that are between the triangles, and therefore the middle areas retain their flat nature enabling printing without spillage. Figure 7.6 (a) and (b) show the resultant structures of two different attempts of the triangular groves etched into Silicon wafer. Figure 6.6 (a) shows the SEM image of the structures etched with SF_6 / O_2 = 70 sccm / 12 sccm, for 15 mins at -120 ^{O}C, and (b) etched with same gas ratio for 7 mins at -80 ^{O}C. It was observed that at very low temperatures significant micro masking results in black Si inside the triangular groves.

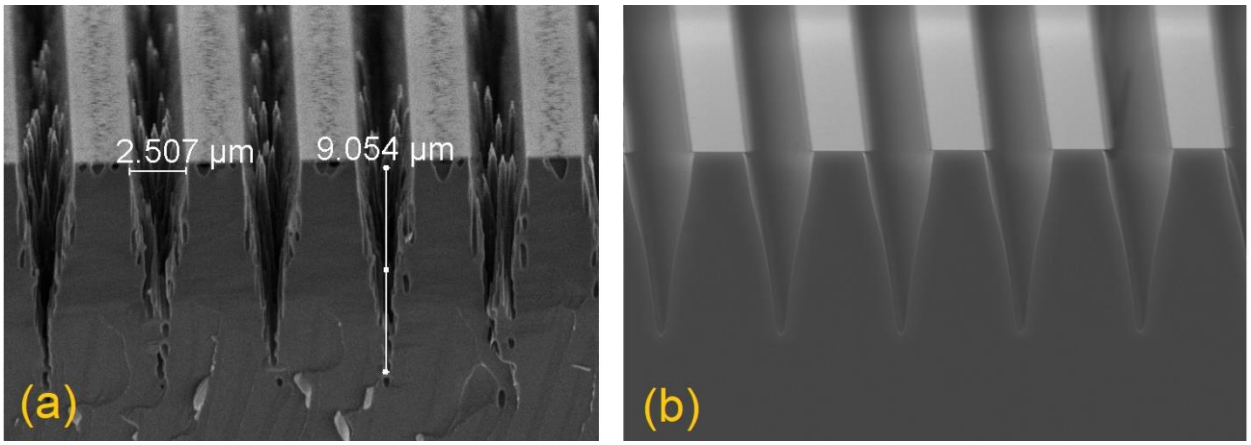

***Figure 7.6**: (a) and (b) show SEM images of triangular groves etched via ICP-RIE at -120 OC and -80 OC respectively.*

Black Si can be reduced by decreasing the passivation gas or by increasing the table temperature. In this case, since we need to maintain the triangular shape of the etch, changing the amount of etch gas in the plasma change the slope of the sidewalls. Therefore, temperature was raised to -80 ^{O}C and structures shown in Figure 7.6 (b) were obtained. The reduced passivation of sidewalls enables faster etching and therefore ~ 7.5 µm depth was obtained in 7 mins. The two images in Figure 7.6 are designed for a 50 % coverage of ETCs designed via electron beam lithography.

To demonstrate that this etching process is more general to different spacings, multiple aspect ratios, and even for a crossing grid lines, samples were prepared via photolithography to define 2.5 µm, 5 µm, and 10 µm grid lines with various spacings. The resultant etch geometries are shown in Figure 7.7. The ~ 1:3 aspect ratio of triangles is maintained under SF_6 / O_2 gas ratio of 70 sccm / 12 sccm for the three cases. The etch times were 7.5 mins, 15 mins, and 30 mins for the three cases respectively. It can be observed that for very long etch time like ~ 30 mins the walls of the triangles are not as smooth as for shorter etch times. Longer etch times result in deeper structures and therefore the products of etching during the etching have a harder task of escaping out. This results in mask undercut and rougher sidewalls as shown in Figure 7.7 (c). The dimensions of the base of triangles are slightly off from the expected dimensions of 2.5 µm, 5 µm, and 10 µm due to non-optimal lithography conditions.

Figure 7.8 shows SEM images of a grid of triangular groves etched using ICP-RIE. At SF_6 / O_2 ratio of 70 sccm / 15 sccm, 1:2 aspect ratio triangular groves were obtained and changing the ratio to 70 sccm / 12 sccm results in 1:3 aspect ratio groves. The effect of etching for more than required time can be seen in Figure 6.8 (a). The tip of 1:2 aspect ratio triangle was slightly elongated as a result of over etching. Therefore, it is important to stop the etching process right when the grove reaches a triangular shape. Etching for a lower time results in blunt triangular tip. Figure 7.8 shows that etching doesn't show any artifacts when a grid of lines was used in place of separated straight lines, thus expanding the scope of possible front contact designs.

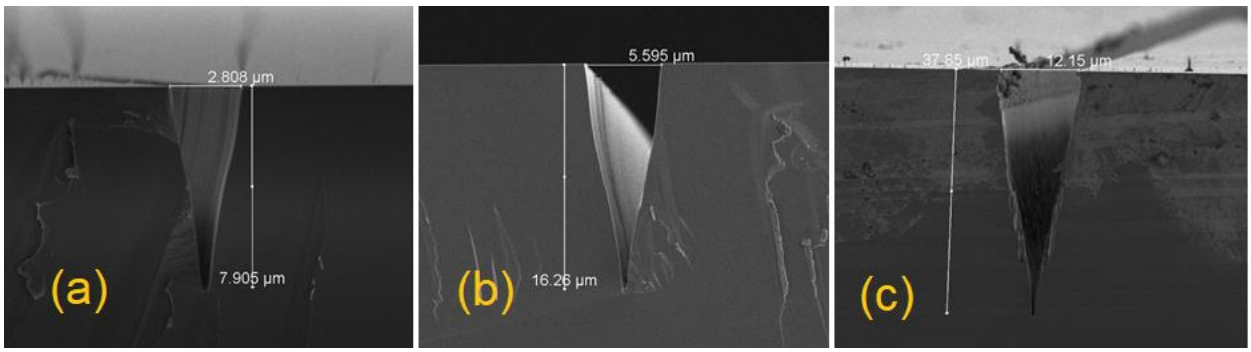

***Figure 7.7**: (a), (b), and (c) show the SEM images of triangular groves etched vai ICP-RIE at -80 ^{O}C, with a SF_6 / O_2 gas ratio of 70 sccm / 12 sccm for 7.5 mins, 15 mins, and 30 mins respectively.*

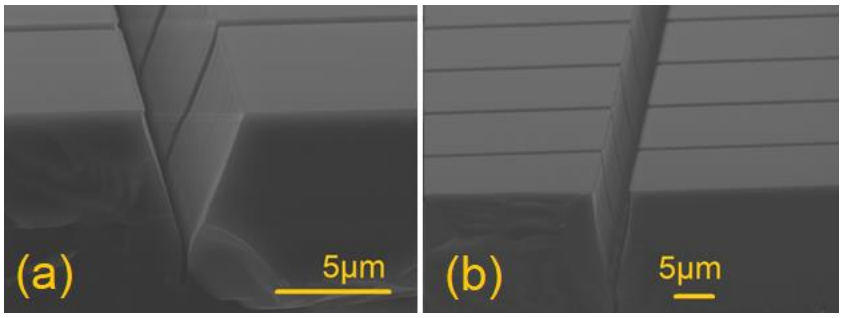

***Figure 7.8**: (a) and (b) show SEM images of etched triangular groves of 5 um bases with 1:2 and 1:3 aspect ratios respectively. These samples employed a grid of lines pattern, and therefore horizontal triangular groves can be see intersecting the triangular grove facing out of the plane of this page. Etching is performed at -80 ^{O}C. SF_6 / O_2 gas ratios utilized are 70 sccm /15 sccm, and 70 sccm / 12 sccm for in case of (a) and (b) respectively.*

7.5 Printing ETCs from etched Si masters

In order to demonstrate that Ag triangles can be printed using the stamps fabricated from the etched Si masters, the contact pattern on a typical Alta Device's GaAs solar cell pattern was utilized. The zoomed-out AutoCAD schematic of the contact pattern is shown in Figure 7.9. The busbar is in the middle and tapers from thick to thin as one moves away from the rectangular contact pad. Fingers extend perpendicular from the bus bar and are ~ 5 μm wide.

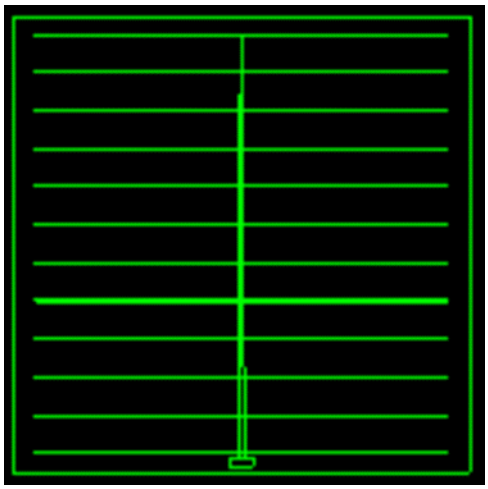

Figure 7.9*: Screen grab of the AutoCAD pattern of Alta Device solar cell's contact pattern. Picture credit: Michael D. Kelzenberg.*

Si wafer was photolithographically patterned and etched such that the fingers are of 1:3 aspect ratio. PDMS stamp was fabricated as described in Figure 7.3. The SEM image of as prepared stamp is shown in Figure 7.10. Figure 7.10 (a) shows the part of the stamp with the contact pad extending into a bus bar, (b) shows the busbar with perpendicular triangular fingers somewhere in the middle of the contact pattern, and (c) zooms into one of the fingers and the triangular shape of the stamp can be observed. The bumps in the middle of the bus bar are a result of some unetched areas inside the bus bar due to photolithography artifacts resulting in the bumps in the stamp. This stamp was applied on a glass slide and Ag ink was injected into the contact pad area. The end of the fingers was opened to let the air come out and create space for the flowing Ag ink using a razor blade. This rested in the Ag ink that was applied to the contact pad flow into the bus bar and then into the fingers replicating the full contact pattern. SEM image in Figure 7.11 (a) shows the zoomed-out view of the middle of

the contact pattern demonstrating the Ag ink in the bus bar and fingers. Figure 6.11 (b) show the zoomed in SEM image of one of the fingers, and it can be observed that the triangular shape is well maintained after printing.

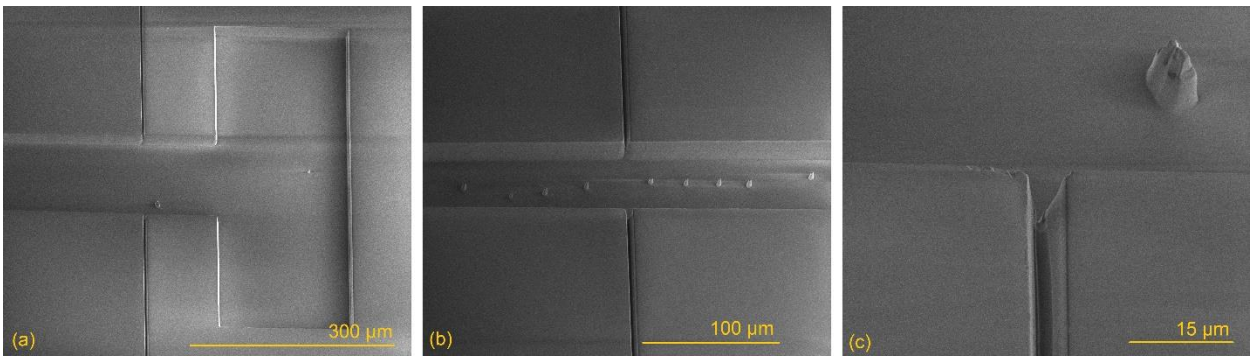

Figure 7.10*: (a), (b), and (c) show the SEM images of different parts of the PDMS stamp fabricated using the Alta Device's contact etch pattern in Si. (a) shows the contact pad area, (b) shows an area in the middle of the pattern with bus bar in the middle and fingers perpendicular to it, and (c) shows the triangular morphology of a finger in the stamp*

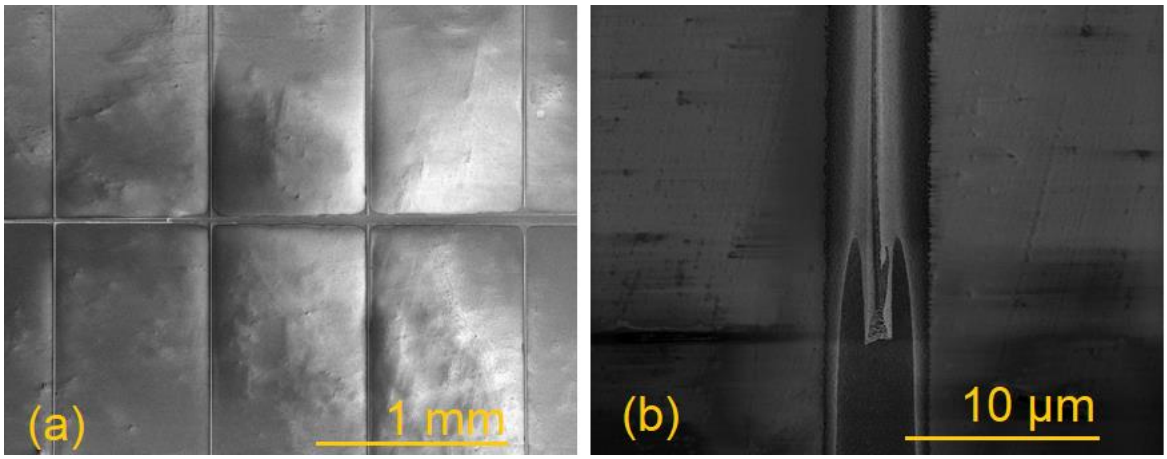

Figure 7.11*:. (a) and (b) show the SEM image of printed Ag triangles over a glass slide utilizing the Alta Device's contact pattern. (a) shows the zoomed-out view showing the busbar is filled with Ag ink and is connected to the triangular fingers with minor spills around the bus bar. (b) shows a zoomed in image of one of the fingers that shows the top view of the triangular morphology of the contact pattern.*

7.6 ETC superstrates

As discussed in previous section fabrication of ETC superstrates has the potential to solve the integration of ETCs onto very rough Si homojunctions solar cells that occupy majority of the photovoltaic market. Schematic in Figure 6.12 shows the ETC superstrate scheme for incorporating ETCs over textured Si solar cells.

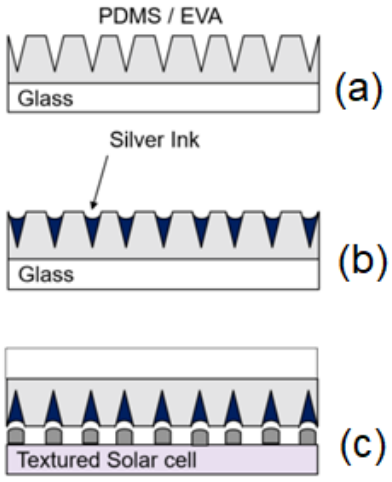

***Figure 7.12**: Schematic for incorporating ETC superstrates over textured Si homojunction solar cells.*

Figure 7.12 (a) shows a schematic of a superstrate made from PDMS or EVA (ethylene-vinyl acetate) with triangular groves over a glass handle. They were prepared in a way similar to making a PDMS stamp from Si master with an addition of a glass handle over the PDMS while it cures to be a stamp. (b) shows the schematic of the superstrate after infilling Ag ink. Ag ink infill was done by applying the Ag ink to the edges of the fingers. Capillary forces associated with the triangular grove allows for the ink to infill into the superstrate. It is observed that a 10 s oxygen plasma at 100 W and 300 mTorr chamber pressure increase the travel distance of the ink in a superstrate. In best case scenarios ink travel length of 1 cm was observed. Optical photograph of one such sample is shown in Figure 7.13. The superstrate appears visually transparent since the triangular Ag infilled allows for transmission of most of the incident light. Figure 7.14 shows the SEM cross sectional image of one such superstrate showing the flow pattern of the Ag ink.

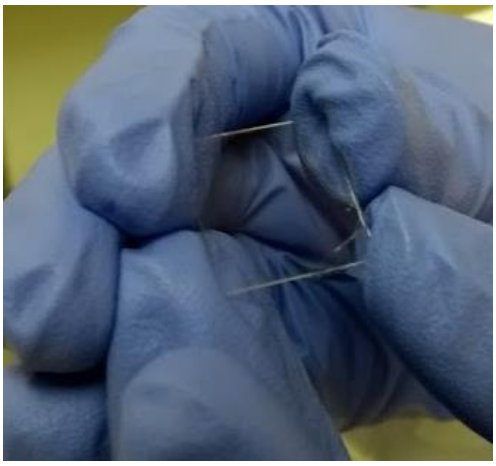

Figure 7.14*: Photograph of an ETC superstrate with Ag filled triangular groves in PDMS on glass. Picture credit: Rebecca Saive and Sophia Coplin*

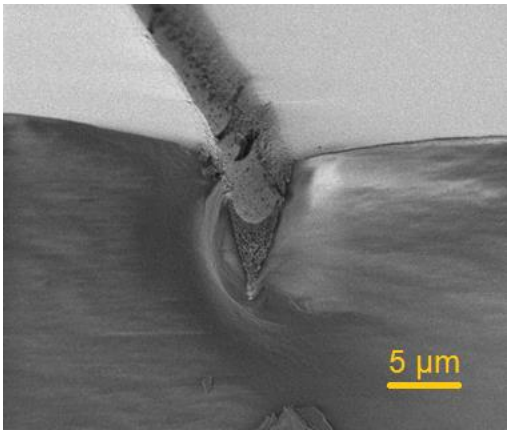

Figure 7.13*: Cross sectional SEM image of an ETC superstrate showing the flow pattern of the ink.*

The superstrates demonstrated so far utilized ETC patterns with 5 µm base. As mentioned previously the fabrication of Si masters with 30 – 50 µm width is yet to be realized, and therefore are not yet ready for application to Si homojunction solar cells. Currently efforts are ongoing to fabricate large size triangles in Si or utilizing 3D printing to realize hard masters with 1:3 aspect ratio triangles with a 30 – 50 µm base.

7.7 Future Work on ETCs

Until now ETCs were implemented over flat surfaces reliably and photocurrent enhancement was demonstrated when implemented over Si heterojunction solar cells. The ability to etch multiple sizes and spacings of triangular groves in Si and being able to print Ag triangles over flat substrates already provides an opportunity to utilize ETCs over bifacial flat Si heterojunction solar cells, III – V group based single and multijunction solar cells that are typically utilized in concentrated photovoltaic, and space applications. It was previously calculated that below 25 % coverage Ag usage does not exceed a standard cell[237] but is yet to be experimentally demonstrated.

Previous theoretical calculations showed that up to 50 % coverage of ETCs on the front surface doesn't significantly reduce the absorbed light in the substrate, and that 83 % coverage on the front can enhance light absorption in thin Si / Ag structures [236]. This opens new possibilities for using Ag triangles as "effectively transparent catalysts" over photoelectrochemical cells. Ag is known for being able to catalyze CO_2 to CO [238], therefore high density of ETCs can provide a lot of surface sites to catalyze the reaction while simultaneously not compromising on light absorption.

If one aims to bring ETCs into real world, future ETC research must be focused on building a tool that can reliably implement ETCs on various solar cells with minimum Ag waste. Current method of applying ink on the sides of a stamp wastes a lot of ink and depends on capillary forces for the ink to travel long distances. The longest travel distances observed till date are ~ 1 cm and therefore a system that can potentially incorporate an inlet and outlet such that pressure is controlled in a similar manner to microfluidic systems.

ETC superstrate strategy can be an alternative for incorporating the ETCs over textured surfaces. For implementation over Si solar cells that occupy most of the photovoltaic market, PDMS must be replaced by EVA. EVA is known to last for > 20 years and is cheap for laminating solar cells while making solar panels. Preliminary studies with EVA showed that one can fabricate a superstrate utilizing EVA. Currently the biggest bottleneck is the realization of a hard master with large (30 – 50 μm) triangular groves. Having the ability to fabricate large triangles enables trials of incorporating ETCs with screen printed contacts over conventional solar cells.

One other major question that is not explored is whether the ETCs can survive the laminating process after implementing over a solar cell. All the solar cell technologies are incorporated in a polymer for preventing physical and chemical degradation due to external factors and demonstrating that ETCs can withstand the process of lamination will be an important step in convincing us the researchers and the photovoltaics industry that they can be realized outside the lab for real world applications.

In conclusion, ETCs provide an opportunity to reach new heights in efficiencies in principle for all the solar cell technologies, and potentially for photoelectrochemical solar fuel devices when implemented as a catalyst. Implementation over textured solar cells remains a challenge due to Ag ink spillage, and implementation over perovskite solar cells is a challenge to be solved since these cells don't withstand high temperatures required for annealing the ink. ETC superstrate strategy can be a potential solution in these two cases.

Chapter 8

Future and Outlook

In summary this thesis deals primarily with optical strategies utilizing pointy structures for light trapping that is generally applicable to solar photovoltaics and/or photoelectrochemical systems. First few chapters discussed how to maximize absorption in a semiconducting conical light absorber, followed by a general light trapping strategy using dielectric nanocones which can enable high loadings of light blocking catalyst or metal front contact, and finally explored structuring the metal itself into a triangular shape to redirect incident light on to the substrate that is otherwise lost due to front surface reflection. In this final chapter I would like to point out some interesting unanswered questions that may be of interest for future energy research involving pointy structures.

8.1 Semiconducting micro- and nano- cones

The physics and advantages of conical architecture was demonstrated in detail in this thesis. Semiconducting conical architecture provides an ideal design for maximizing the absorption. The choice of bottom and top radii of a conical architecture determines the broadband of illumination that can couple light efficiently to a nano cone. The cone must be long enough to maximize the absorption by providing enough length for light to propagate until it is absorbed. Therefore, for an indirect band gap material like Si the cone must be as long as ~75 μm as shown in this thesis, whereas in case of a direct band gap semiconductors such as GaAs or InP only a few microns are enough to absorb light effectively [183, 184].

The impressive optical properties of conical semiconducting structures come at a cost of increased surface area. In case of Si cones the surface area increases by more than an order of magnitude. Therefore, any surface passivation mechanism that must be as many times lower in terms of surface recombination velocity. In terms of the possibility of just reaching the current efficiency record for Si based solar cells the surface recombination velocity must be ~ 1 cm/s or below, and it has to be as low even in places where one wishes to make a contact to get current out. This rules out any type

of direct metal contact to the Si cone since such an interface will act as a site for infinite surface recombination velocity. An infinite recombination velocity center will limit the average diffusion length of the carriers to a number smaller than its maximum dimension. Therefore any Si cone based device must employ a surface passivation and a carrier selective contact which can maintain < 1% SRVs throughout the surface.

The conical arrays being embedded in a polymer, along with being able to incorporate catalysts on their tips without any significant photocurrent losses make these structures very attractive for a flexible integrated photoelectrochemcial device that could possibly be made roll to roll if this technology wishes to enter the real world. Currently the fabrication involves a cryogenic dry etching process which is a very costly way to manufacture at a large scale. This technique was chosen in this work due to the ability to control the shape precisely, and therefore demonstrate concepts in a scientific setting. If one envisions a path for a future Si microcone based device, a photoelectrochemical etching process similar to the porous Si etching process could be explored to manufacture these structures in a cheaper way [239].

Pt and Co-P hydrogen evolution catalysts were incorporated with Si microcones to demonstrate that high loadings of light blocking highly active catalysts can be employed with minimum photocurrent loss. This can easily be extended to photoanodes that perform oxygen evolution reaction given the abundance of many protection layers that can extend Si photoanode working lifetime [240]. In chapter 4 light directed photoelectrochemical deposition of Au was demonstrated. Au itself can act as a catalyst for reducing CO_2 into CO electrochemically. Therefore, an array of photocathodes with Au deposited at multiple locations over a cone can be explored to figure out the best architecture for Si cones utilizing gold for CO_2 reduction. One can also imagine photoelectrodepositing another material or electrodepositing it over the gold as possibilities for future designs.

Another avenue of study can be understanding the optical effects of bubbles that are formed when H_2 or O_2 or CO or any other gas that can be evolved when these structures are utilized as photoelectrodes. According to reflection measurements Si cones are expected to deliver close to 43 mA cm^{-2}. But experimentally as photocathodes for H_2 evolution these on an average gave only about 35 mA cm-^{2} though an occasional sample might reach up to 38 mA cm^{-2}. This begs the question of where are all those photons going? At such high current it was experimentally observed that a lot of

bubbles were formed and come of the light is being scattered away from the absorber surface. Therefore, an interesting future research problem could be the study of bubble evolution and how to engineer that to minimize the photocurrent loss due to scattering.

Unlike Si, direct band gap semiconductor such as GaAs and InP demonstrate might higher light confinement. It was shown previously that the coupling of light to a nanocone of a direct band gap semiconductor depends on wavelength of light and the radius of the nanocone similar to Si, but the confinement is much stronger. Therefore, photoelectrochecmial Au depositions can be performed over these nanocones to experimentally show the region of high light confinement, which could potentially deposit Au at different radius on the nanocone depending on the wavelength of illumination.

8.2 Dielectric nanocones

It was shown in this thesis that dielectric nanocones enable similar light trapping properties as semiconducting nanocones but since they don't absorb light they can act as light trapping structures over an absorbing semiconductor. Since light was mostly confined inside the nanocones, light blocking catalyst can be incorporated in the middle of these nanocones, making this strategy a universal light trapping strategy for an arbitrary broadband of interest on light absorbers. In this case it was demonstrated primarily for a Si photoanode performing oxygen evolution reaction in basic environment. This strategy being general can be extended any photoelectrochemical reaction as long as the dielectric chosen is stable under operating conditions.

It is well known that higher the dielectric constant higher the light confinement, therefore more detailed investigation is required on a case to case basis to investigate the ideal spacing of these nanocones over light absorbers. Utilizing these nanocones over photoelectrochemical devices can enable incorporate higher loadings of highly active light blocking catalysts, which can enhance the total length of the time the device is active and also enables a more optimum choice for the underlying absorbers tandems. Therefore, these nanocones could enable higher efficiencies than previously shown in the literature, and is an exciting opportunity to pursue in the future.

The nanocones utilized in the work presented in this thesis were fabricated utilizing dry etching. In terms of cost reduction, and scalability, these structures could in principle be fabricated utilizing nanoimprint lithography [241]. Nanoimprint could also be a gentler process than etching in terms of inducing damage on the underlying light absorber due to criticality of stopping the etching right when the dielectric is etched. In this case n-type Si wafer was utilized for the proof of principle demonstrations. Similar process on multijunction III–V solar cells could be disastrous if the etch was not stopped in time given the layers in such cases are 100s on nm to a few microns.

8.3 Metal Triangles

One other way to overcome the front surface losses in a photovoltaic or a photoelectrochemical cell is to restructure the metal contacts into a triangular shape. Triangular shape redirects the light that is otherwise lost due to reflection, back onto the light absorbing substrate improving the photocurrent in a Si heterojunction cell by up to 2 mA cm^{-2} and an increase in the efficiency of ~ 1%. Current demonstrations of such triangular metal contacts were limited to planar solar cell surfaces, and the dimensions were limited to 2.5 – 5 μm at the base and 7.5 – 15 μm height dimensions. By developing an etching process that was described previously in this thesis, the parameter space of triangles in terms of dimensions and spacing can now be varied, and therefore the triangles can be applied to other solar photovoltaic technologies.

Incorporating the metal triangles over textured surfaces and over those surfaces that cannot withstand the Ag ink annealing temperatures are yet to be realized. “Superstrate” strategy previously discussed could potentially be a way to incorporate the Ag triangles in such cases. More work needs to be done in terms of alignment of these superstrates over existing contacts, and also in being able to fill the triangular channels in superstrates to an arbitrary level depending on need. One pathway that is currently being explored is electrodepositing Ag over the partially infilled Ag lines in a superstrate.

Most of the current work in triangles was towards increasing efficiencies in photovoltaics. Application of triangular catalysts on to photoelectrochemical systems is to be explored. The ability to fabricate masters with high density of triangles and coupled with the availability of many nano-particular inks of catalytic materials could enable incorporation of high catalyst loadings to reduce

overpotential while still maintaining high photocurrents in a photoelectrochemical cells. Inks for Ag, and Cu among others are available in the market, and both these are known catalysts for CO_2 reduction. Apart from optical enhancement, there may or may not be some structure related variation in reaction kinetics, that are yet to be explored. Previous study of Au, and Pd nanocones demonstrated a reduction in overpotential due to field induced reagent concentration [242]. Since triangles are also sharp structures similar effects may be applicable, which could enhance the overall photoelectrochemical device efficiency even higher.

8.4 Conclusion

In conclusion the work demonstrated in this thesis demonstrates multiple light trapping strategies that are applicable to both photovoltaics and photoelectrochemical cells. Semiconducting or dielectric conical structures can be designed for an arbitrary broadband of illumination that is of interest for either absorption or transmission. Therefore, the semiconducting cones provide an ideal architecture for maximizing absorption and the dielectric cones for maximizing transmission. Alternatively, triangular metal contacts are a general strategy to render the front contacts of a solar cell effectively transparent, while fabrication challenges remain on textured surfaces.

Appendix A

Limiting Efficiency Simulation Code

The following provides the code for simulating limiting efficiencies for the case of a cone. It can be manipulated into a rectangle by changing coordinates and symmetry options.

Sentaurus structure editor code

```
(sde:clear)
################ Silicon Cone Structure Defined ################
# Cone Surface Passivation Definition
(define verticis2 (list (position 0 -1 0) (position 4.5 -1 0) (position 1.025 76 0) (position 0 76 0)))
# Cone Surface Passivation Material Definition : material name
(sdegeo:create-polygon verticis2 "Anyinsulator" "Cone_Surface")
# Cone Structure Definition
(define verticis1 (list (position 0 0 0) (position 3.5 0 0) (position 0.025 75 0) (position 0 75 0)))
# Cone Material Definition : material name
(sdegeo:create-polygon verticis1 "Silicon" "Cone_1")
# Constant Doping Options : name species concentration
(sdedr:define-constant-profile "BulkDoping" "PhosphorusActiveConcentration" @BulkDoping@)
# Placing Doping Profiles in Cone : name profile region
(sdedr:define-constant-profile-region "BulkDopingPlacement" "BulkDoping" "Cone_1")
# Opt Gen Initializing to zero
(sdedr:define-constant-profile "OptGen" "OpticalGeneration" 0.0)
(sdedr:define-constant-profile-material "OptGen" "OptGen" "Silicon")
(sdedr:define-constant-profile-material "OptGen" "OptGen" "Anyinsulator")
###################### Meshing the Cone ######################
# Define Window
```

```
# (sdedr:define-refinement-window "Cone_EvalWindow1" "Rectangle" (position -1 -1 0) (position 80 80 0))
# Define Mesh Refinement : name max( x y z ) min( x y z )
(sdedr:define-refinement-size "Cone_RefDef1" 1 1 0 0.1 0.1 0)
# Defining Meshing Function : RefinementName Algorithm Material Interface begin ramp
(sdedr:define-refinement-function "Cone_RefDef1" "MaxLenInt" "Silicon" "Anyinsulator" 0.001 1.5)
# Define the Region : Name RefinementName Material StructureName
(sdedr:define-refinement-region "Cone_RefReg1" "Cone_RefDef1" "Cone_1")
# Define Refinement Placement : Name Region
# (sdedr:define-refinement-placement "Cone_RefPlace1" "Cone_RefReg1" "Cone_EvalWindow1")
(sdedr:append-cmd-file "xy.cmd")
# Build Mesh : Mesher Options filebase
(sde:build-mesh "snmesh" "-numThreads 8" "n@node@")
#Save Model
(sde:save-model "n@node@_SiliconConePL")
```

Sentaurus device code

```
File {
## Input Files
Grid = "n@node|sde@_msh.tdr"
Doping = "n@node|sde@_msh.tdr"
Parameter = "@parameter@"
OpticalGenerationInput = "n@node|sde@_optgen.tdr"
## Output Files
Plot = "@tdrdat@"
Current = "@plot@"
Output = "@log@"
}
```

```
Electrode{
}
Physics {
## Recombination & Mobility Models
Recombination (SRH Auger Radiative)
Mobility(DopingDep)
Optics( OpticalGeneration( ReadFromFile( Scaling=0) ) )
}
Physics(Region = "Cone_1") {
EffectiveIntrinsicDensity (BandGapNarrowing (Slotboom))
eQuantumPotential(LocalModel=SchenkBGN_elec)
hQuantumPotential(LocalModel=SchenkBGN_hole)
}
Physics (MaterialInterface="Silicon/Anyinsulator")
{
Recombination(SurfaceSRH)
}
Plot{
eDensity hDensity eCurrent/Vector hCurrent/Vector current/vector
Potential SpaceCharge ElectricField/Vector
SRH Auger RadiativeRecombination TotalRecombination SurfaceRecombination
Doping DonorConcentration AcceptorConcentration EffectiveIntrinsicDensity
ConductionBandEnergy ValenceBandEnergy
eQuasiFermi hQuasiFermi
OpticalGeneration
}
CurrentPlot{
OpticalGeneration(Integrate(Material="Silicon"))
RadiativeRecombination(Integrate(Material="Silicon"))
Auger(Integrate(Material="Silicon"))
```

```
SRH(Integrate(Material="Silicon"))
SurfaceRecombinaiton(Integrate(MaterialInterface = "Silicon/Anyinsulator"))
TotalRecombination(Integrate(Material="Silicon"))
hDensity(Integrate(Material="Silicon"))
eDensity(Integrate(Material="Silicon"))
EffectiveIntrinsicDensity(Integrate(Material="Silicon"))
DonorConcentration(Integrate(Material="Silicon"))
}
Math{
NumberOfThreads=maximum
Extrapolate
Derivatives
RelErrControl
Iterations=25
Notdamped=30
ExitOnFailure
Wallclock
CheckRhsAfterUpdate
ExtendedPrecision(128)
Digits=7
RhsMin=1e-12
StackSize = 5000000
PeriodicBC(Direction=0 Coordinates=(0 10))
Method=Pardiso
CurrentPlot (IntegrationUnit = cm)
}
Solve{
Coupled { poisson }
Coupled { poisson electron }
Coupled { poisson electron hole }
```

```
Save( FilePrefix="PLdark_n@node@" )
Quasistationary( InitialStep=0.1 MinStep=1e-10 MaxStep=1 Goal { ModelParameter = "Optics/OpticalGeneration/ReadFromFile/Scaling" Value = 0.000001637323944} ){ Coupled { poisson electron hole }}
Plot( FilePrefix="PLlight_n@node@" )
}
```

Sentaurus visual code

```
set volumefactor [expr 2e6]
set Thickness [expr 5e-4]
echo "af = $volumefactor \[cm^2\]"
set RECOMBINATIONS [load_file n@previous@_des.plt -name RECOMBINATIONS]
set OPTgen [get_variable_data "IntegrSilicon OpticalGenerationFromFile" -dataset RECOMBINATIONS]
set RADrec [get_variable_data "IntegrSilicon RadiativeRecombination" -dataset RECOMBINATIONS]
set AUGrec [get_variable_data "IntegrSilicon AugerRecombination" -dataset RECOMBINATIONS]
set SRHrec [get_variable_data "IntegrSilicon SRHRecombination" -dataset RECOMBINATIONS]
set SURrec [get_variable_data "IntegrSilicon/Anyinsulator SurfaceRecombination" -dataset RECOMBINATIONS]
set Hd [get_variable_data "IntegrSilicon hDensity" -dataset RECOMBINATIONS]
set Ed [get_variable_data "IntegrSilicon eDensity" -dataset RECOMBINATIONS]
set Ni [get_variable_data "IntegrSilicon EffectiveIntrinsicDensity" -dataset RECOMBINATIONS]
set OPT [expr [lindex $OPTgen end]*$volumefactor]
set RAD [expr [lindex $RADrec end]*$volumefactor]
set AUG [expr [lindex $AUGrec end]*$volumefactor]
set SRH [expr [lindex $SRHrec end]*$volumefactor]
set SUR [expr [lindex $SURrec end]*$volumefactor]
set hD [expr [lindex $Hd end]*$volumefactor]
set eD [expr [lindex $Ed end]*$volumefactor]
```

```
set ni [expr [lindex $Ni end]*$volumefactor]
set Voc [expr 0.02585*log(($hD*$eD)/($ni*$ni))]
set Jsc [expr $OPT*(1.6e-19)*$Thickness*1000]
set voc [expr $Voc*(1.6e-19)/(300*(1.38064852e-23))]
set FF [expr ($voc - log($voc + 0.72))/($voc + 1)]
set Eff [expr $Voc*$Jsc*$FF]
puts "DOE: OPT [format %.2e $OPT]"
puts "DOE: RAD [format %.2e $RAD]"
puts "DOE: AUG [format %.2e $AUG]"
puts "DOE: SRH [format %.2e $SRH]"
puts "DOE: SUR [format %.2e $SUR]"
puts "DOE: hD [format %.2e $hD]"
puts "DOE: eD [format %.2e $eD]"
puts "DOE: ni [format %.2e $ni]"
puts "DOE: Voc [format %.2f $Voc]"
puts "DOE: Jsc [format %.2f $Jsc]"
puts "DOE: FF [format %.2f $FF]"
puts "DOE: Eff [format %.2f $Eff]"
exit
```

Appendix B

Fabrication Conditions for Si Microcones

The etching parameters are subject to vary a little between etching machines. The conditions given here are the ones used at the time of writing this thesis.

Following is the recipe on Oxford instruments plasmalab ICP/RIE 380 system

Step 1

CCP (W)	ICP (W)	SF_6 (sccm)	O_2 (sccm)	T (^{0}C)	P (mTorr)	Time (min)
7	900	70	6	-120	10	30

Step 2

CCP (W)	ICP (W)	SF_6 (sccm)	O_2 (sccm)	T (^{0}C)	P (mTorr)	Time (min)
7	900	70	6.5	-120	10	30

Step 3

CCP (W)	ICP (W)	SF_6 (sccm)	O_2 (sccm)	T (^{0}C)	P (mTorr)	Time (min)
7	900	70	7	-120	10	30

Following is the recipe on Oxford instruments plasmalab DRIE system

Step 1

CCP (W)	ICP (W)	SF_6 (sccm)	O_2 (sccm)	T (^{0}C)	P (mTorr)	Time (min)
3	900	70	6	-130	10	30

Step 2

CCP (W)	ICP (W)	SF_6 (sccm)	O_2 (sccm)	T (^{0}C)	P (mTorr)	Time (min)
3	900	70	7	-130	10	30

Step 3

CCP (W)	ICP (W)	SF_6 (sccm)	O_2 (sccm)	T (^{0}C)	P (mTorr)	Time (min)
3	900	70	8	-130	10	30

Note on etching: If the voltage corresponding to CCP power is ~ 26 V the oxygen must increase in steps of 1 sccm in each step, and if it is ~ 19 V the oxygen must increase in steps of 0.5 sccm to maintain the conical shape utilized in this thesis. It is recommended that a 10 min oxygen plasma clean is done prior to cry etching, followed by a 30 min chamber conditioning run using the conditions of step 1 before loading the Si sample for cone etching using the 3 steps described here,

Appendix C

Fabrication Conditions for TiO_2 Nanocones

Given the limited amount of information regarding dry etching of TiO_2, multiple recipes were attempted before settling on the recipe utilized in this thesis.

***Table C 1**: Etching perfomed at 00C, 7 mTorr, and for 5 mins with a 150 nm Cr mask*

Sample	SF_6	Ar	C_4F_8	CH_4
1	15	0	40	0
2	15	0	40	15
3	15	0	40	30
4	15	50	40	30
5	15	50	20	15
6	15	50	40	0

*Flow rates in SCCM

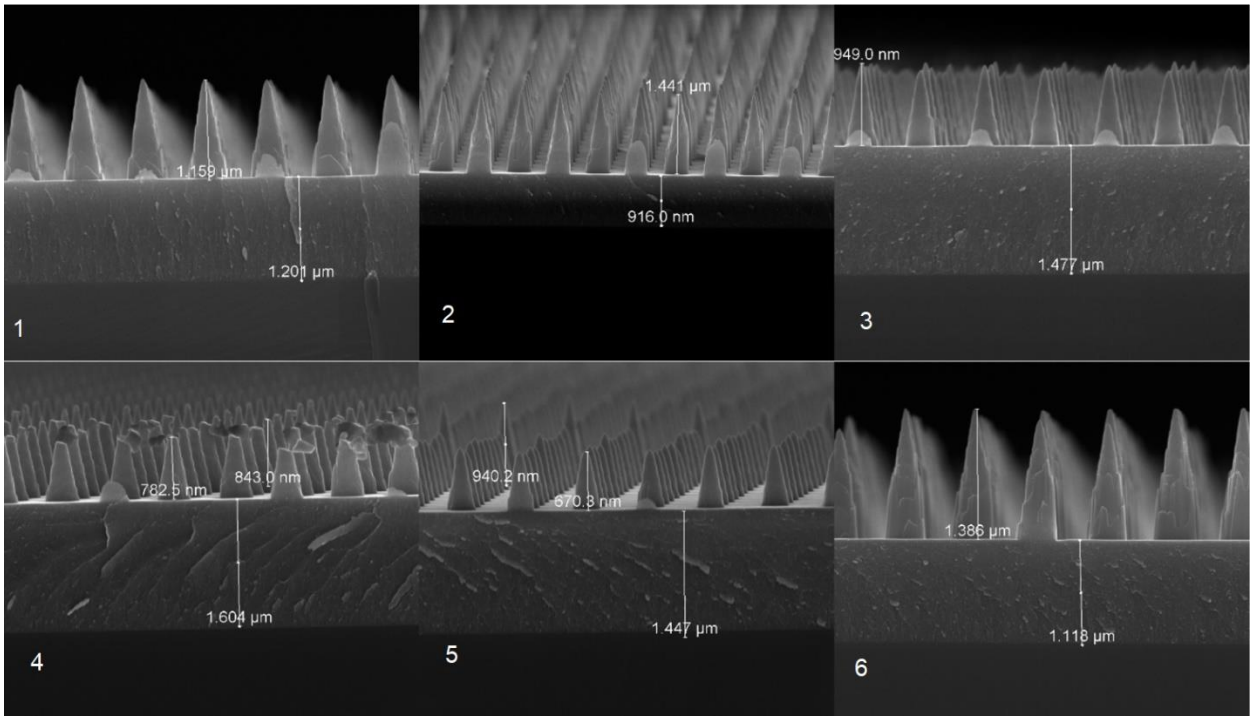

***Figure C 1**: SEM images of etchied TiO2 nanocones using recipes 1-6*

Final Recipe for TiO_2 cone etching is given below. The Cr mask used is ~ 200 nm thick to make it last longer to obtain taller cones. Increasing SF_6 flow increases the cone taper.

CCP (W)	ICP (W)	SF_6 (sccm)	C_4F_8 (sccm)	T (^{0}C)	P (mTorr)	Time (min)
150	2500	23.5	40	0	7	15

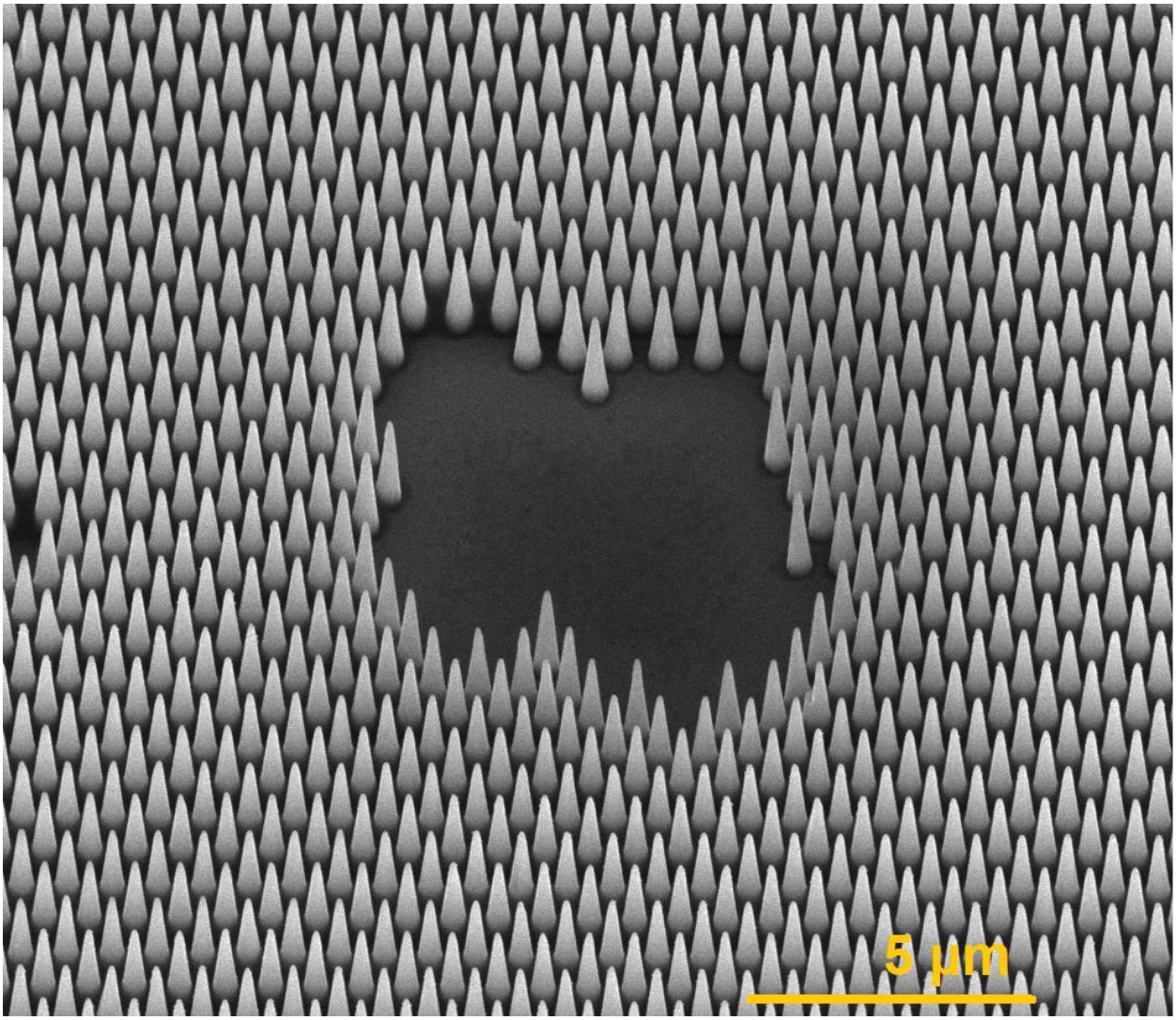

Figure C 2*: SEM image of one of the samples with smooth uniform cones etched using the optimized recipe.*

Appendix D

Fabrication Conditions for Triangular Si Groves

Following is the recipe for etching of 1:3 aspect ratio triangular groves using Oxford instruments plasmalab ICP/RIE 380 system.

CCP (W)	ICP (W)	SF_6 (sccm)	O_2 (sccm)	T (^{0}C)	P (mTorr)
7	900	70	12	-80	10

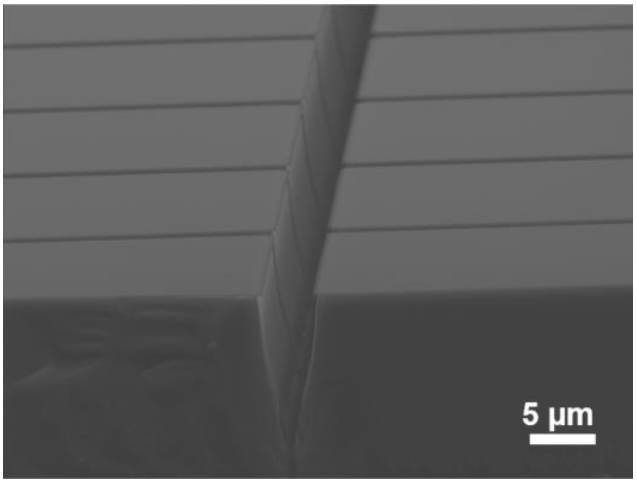

Figure D 1*: 1:3 aspect ratio triangular groves etched for ~ 14 mins*

Following recipe is for etching 1:2 aspect ratio triangular groves using Oxford instruments plasmalab ICP/RIE 380 system

CCP (W)	ICP (W)	SF_6 (sccm)	O_2 (sccm)	T (^{0}C)	P (mTorr)
7	900	70	15	-80	10

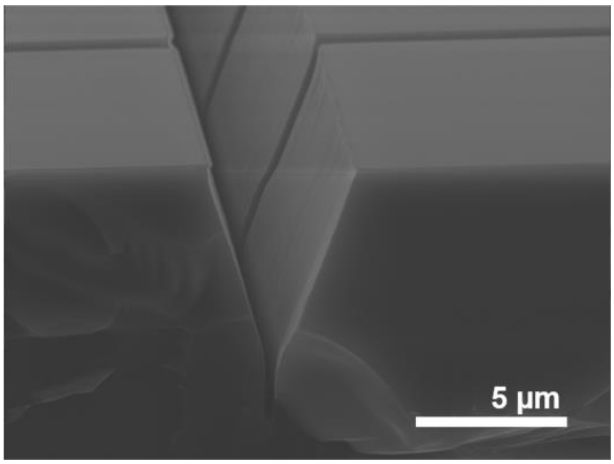

***Figure D 2**: 1:2 aspect ratio triangular groves etched for ~ 12 mins*

Appendix E

Fabrication Procedure for Metal Cones

Fabrication of metal cones was attempted for fabricating 3-dimensional conical metal catalysts similar to a previous study that utilized evaporation [243]. This was explored as an alternative for effectively transparent catalyst. Schematic in Figure E1 shows the fabrication steps. Figure E2 shows the SEM image of as prepared Cu cones. The cones didn't stick to the underlying Si surface and therefore can be seen to be scattered around.

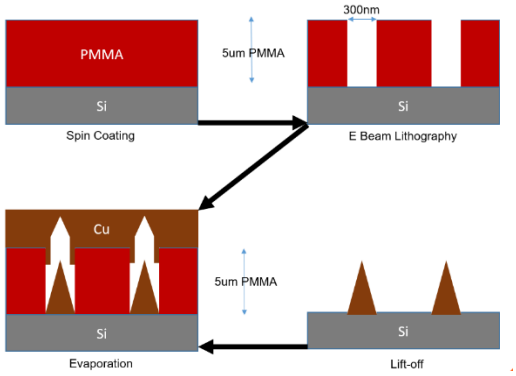

***Figure E 1**: Fabrication procedure for metal nanocones via evaporation*

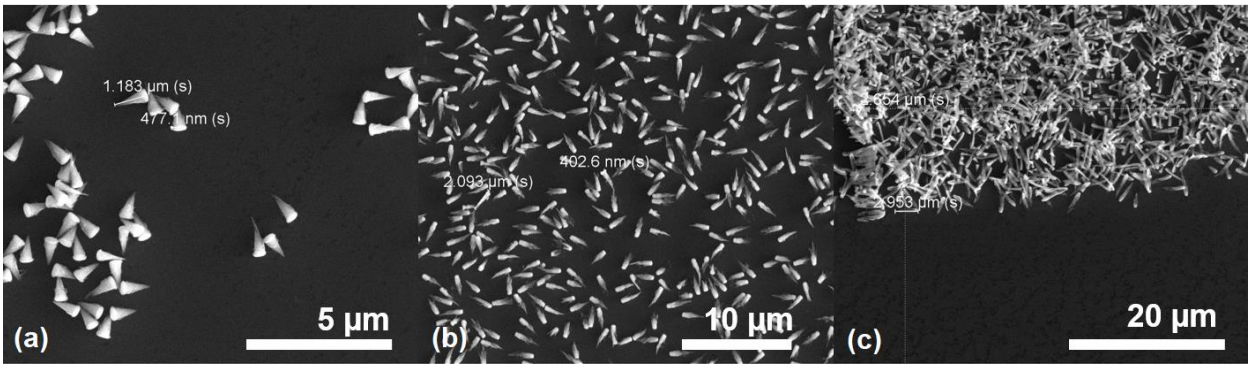

***Figure E 2**: (a), (b), and (c) show the SEM images of Cu nanocones fabricated using electron beam evaporation. They have different heights due to different angles at which evaporation is done, which lead to closing of the hole in PMMA differ leading to different lengths.*

Bibliography

[1] R. Joyeux and R. D. Ripple, "Household energy consumption versus income and relative standard of living: A panel approach," *Energy Policy,* vol. 35, no. 1, pp. 50-60, 2007/01/01/ 2007.

[2] J. Asafu-Adjaye, "The relationship between energy consumption, energy prices and economic growth: time series evidence from Asian developing countries," *Energy Economics,* vol. 22, no. 6, pp. 615-625, 2000/12/01/ 2000.

[3] N. S. Ouedraogo, "Energy consumption and human development: Evidence from a panel cointegration and error correction model," *Energy,* vol. 63, pp. 28-41, 2013/12/15/ 2013.

[4] M. I. Hoffert *et al.*, "Energy implications of future stabilization of atmospheric CO2 content," *Nature,* vol. 395, p. 881, 10/29/online 1998.

[5] "International Energy Outlook 2015," Energy Information Administration2015.

[6] H. D. Matthews and K. Caldeira, "Stabilizing climate requires near-zero emissions," *Geophysical Research Letters,* vol. 35, no. 4, 2008/02/01 2008.

[7] R. Joeri *et al.*, "Zero emission targets as long-term global goals for climate protection," *Environmental Research Letters,* vol. 10, no. 10, p. 105007, 2015.

[8] United Nations. (2016). *The Paris Agreement*.

[9] IEA, "Key World Energy Statistics," IEA2017, Available: http://www.iea.org/publications/freepublications/.

[10] J. Tsao, N. S. Lewis, and G. Crabtree, "Solar FAQs," Sandia National Lab2006, Available: https://www.sandia.gov/~jytsao/Solar%20FAQs.pdf.

[11] BP, "Statitstical Review of World Energy," BP 2018, Available: https://www.bp.com/content/dam/bp/en/corporate/pdf/energy-economics/statistical-review/bp-stats-review-2018-full-report.pdf.

[12] "Photovoltaics Report," Frauenhofer Institute for Solar EnergyAugust 10, 2018 2018, Available: https://www.ise.fraunhofer.de/content/dam/ise/de/documents/publications/studies/Photovoltaics-Report.pdf.

[13] N. S. Lewis, "Research opportunities to advance solar energy utilization," *Science,* vol. 351, no. 6271, pp. 353-362, 2016.

[14] K. Yoshikawa *et al.*, "Silicon heterojunction solar cell with interdigitated back contacts for a photoconversion efficiency over 26%," Article vol. 2, p. 17032, 03/20/online 2017.

[15] S. J. Davis *et al.*, "Net-zero emissions energy systems," *Science,* 10.1126/science.aas9793 vol. 360, no. 6396, 2018.

[16] W. Shockley and H. J. Queisser, "Detailed Balance Limit of Efficiency of p-n Junction Solar Cells," *Journal of Applied Physics,* vol. 32, no. 3, pp. 510-519, 1961/03/01 1961.

[17] A. Richter, M. Hermle, and S. W. Glunz, "Reassessment of the Limiting Efficiency for Crystalline Silicon Solar Cells," *IEEE Journal of Photovoltaics,* vol. 3, no. 4, pp. 1184-1191, 2013.

[18] M. L. Brongersma, Y. Cui, and S. Fan, "Light management for photovoltaics using high-index nanostructures," *Nature Materials,* Review Article vol. 13, p. 451, 04/22/online 2014.

[19] H. K. Raut, V. A. Ganesh, A. S. Nair, and S. Ramakrishna, "Anti-reflective coatings: A critical, in-depth review," *Energy & Environmental Science,* 10.1039/C1EE01297E vol. 4, no. 10, pp. 3779-3804, 2011.

[20] E. Yablonovitch, "Statistical ray optics," *Journal of the Optical Society of America,* vol. 72, no. 7, pp. 899-907, 1982/07/01 1982.

[21] A. Bozzola, P. Kowalczewski, and L. C. Andreani, "Towards high efficiency thin-film crystalline silicon solar cells: The roles of light trapping and non-radiative recombinations," *Journal of Applied Physics,* vol. 115, no. 9, p. 094501, 2014.

[22] P. Kowalczewski and L. C. Andreani, "Towards the efficiency limits of silicon solar cells: How thin is too thin?," *Solar Energy Materials and Solar Cells,* vol. 143, pp. 260-268, 2015/12/01/ 2015.

[23] K. Yoshikawa *et al.*, "Silicon heterojunction solar cell with interdigitated back contacts for a photoconversion efficiency over 26%," *Nature Energy,* Article vol. 2, p. 17032, 03/20/online 2017.

[24] T. Trupke *et al.*, "Temperature dependence of the radiative recombination coefficient of intrinsic crystalline silicon," *Journal of Applied Physics,* vol. 94, no. 8, pp. 4930-4937, 2003.

[25] R. Häcker and A. Hangleiter, "Intrinsic upper limits of the carrier lifetime in silicon," *Journal of Applied Physics,* vol. 75, no. 11, pp. 7570-7572, 1994.

[26] J. G. Fossum, R. P. Mertens, D. S. Lee, and J. F. Nijs, "Carrier recombination and lifetime in highly doped silicon," *Solid-State Electronics,* vol. 26, no. 6, pp. 569-576, 1983/06/01/ 1983.

[27] G. Masetti, M. Severi, and S. Solmi, "Modeling of carrier mobility against carrier concentration in arsenic-, phosphorus-, and boron-doped silicon," *IEEE Transactions on Electron Devices,* vol. 30, no. 7, pp. 764-769, 1983.

[28] M. A. Green, "Accurate expressions for solar cell fill factors including series and shunt resistances," *Applied Physics Letters,* vol. 108, no. 8, p. 081111, 2016.

[29] U. Rau, "Reciprocity relation between photovoltaic quantum efficiency and electroluminescent emission of solar cells," *Physical Review B,* vol. 76, no. 8, p. 085303, 08/02/ 2007.

[30] D. B. M. Klaassen, J. W. Slotboom, and H. C. de Graaff, "Unified apparent bandgap narrowing in n- and p-type silicon," *Solid-State Electronics,* vol. 35, no. 2, pp. 125-129, 1992/02/01/ 1992.

[31] S. Yalamanchili, H. S. Emmer, K. T. Fountaine, C. T. Chen, N. S. Lewis, and H. A. Atwater, "Enhanced Absorption and <1% Spectrum-and-Angle-Averaged Reflection in Tapered Microwire Arrays," *ACS Photonics,* vol. 3, no. 10, pp. 1854-1861, 2016/10/19 2016.

[32] S. Yalamanchili, H. S. Emmer, N. S. Lewis, and H. A. Atwater, "Highly absorbing and high lifetime tapered silicon microwire arrays as an alternative for thin film crystalline silicon solar cells," in *2016 IEEE 43rd Photovoltaic Specialists Conference (PVSC),* 2016, pp. 2999-3003.

[33] T. Tiedje, E. Yablonovitch, G. D. Cody, and B. G. Brooks, "Limiting efficiency of silicon solar cells," *Electron Devices, IEEE Transactions on,* vol. 31, no. 5, pp. 711-716, 1984.

[34] A. Richter, S. W. Glunz, F. Werner, J. Schmidt, and A. Cuevas, "Improved quantitative description of Auger recombination in crystalline silicon," *Physical Review B,* vol. 86, no. 16, p. 165202, 10/09/ 2012.

[35] M. A. Green, K. Emery, Y. Hishikawa, W. Warta, and E. D. Dunlop, "Solar cell efficiency tables (version 47)," *Progress in Photovoltaics: Research and Applications,* vol. 24, no. 1, pp. 3-11, 2016.
[36] M. Taguchi *et al.*, "24.7% Record Efficiency HIT Solar Cell on Thin Silicon Wafer," *Photovoltaics, IEEE Journal of,* vol. 4, no. 1, pp. 96-99, 2014.
[37] P. Ortega *et al.*, "High-efficiency black silicon interdigitated back contacted solar cells on p-type and n-type c-Si substrates," *Progress in Photovoltaics: Research and Applications,* vol. 23, no. 11, pp. 1448-1457, 2015.
[38] P. Kowalczewski, A. Bozzola, M. Liscidini, and L. Claudio Andreani, "Light trapping and electrical transport in thin-film solar cells with randomly rough textures," *Journal of Applied Physics,* vol. 115, no. 19, p. 194504, 2014.
[39] A. Deinega and S. John, "Solar power conversion efficiency in modulated silicon nanowire photonic crystals," *Journal of Applied Physics,* vol. 112, no. 7, p. 074327, 2012.
[40] R. Brendel *et al.*, "High-Efficiency Cells From Layer Transfer: A First Step Toward Thin-Film/Wafer Hybrid Silicon Technologies," *IEEE Journal of Photovoltaics,* vol. 1, no. 1, pp. 9-15, 2011.
[41] L. Wang *et al.*, "Development of a 16.8% Efficient 18-μm Silicon Solar Cell on Steel," *IEEE Journal of Photovoltaics,* vol. 4, no. 6, pp. 1397-1404, 2014.
[42] M. S. Branham *et al.*, "Silicon Solar Cells: 15.7% Efficient 10-μm-Thick Crystalline Silicon Solar Cells Using Periodic Nanostructures (Adv. Mater. 13/2015)," *Advanced Materials,* vol. 27, no. 13, pp. 2268-2268, 2015.
[43] S. Jeong, M. D. McGehee, and Y. Cui, "All-back-contact ultra-thin silicon nanocone solar cells with 13.7% power conversion efficiency," *Nat Commun,* Article vol. 4, 12/16/online 2013.
[44] M. L. Brongersma, Y. Cui, and S. Fan, "Light management for photovoltaics using high-index nanostructures," *Nat Mater,* Review vol. 13, no. 5, pp. 451-460, 05//print 2014.
[45] M. Berginski *et al.*, "Experimental studies and limitations of the light trapping and optical losses in microcrystalline silicon solar cells," *Solar Energy Materials and Solar Cells,* vol. 92, no. 9, pp. 1037-1042, 9// 2008.
[46] V. Jovanov, U. Planchoke, P. Magnus, H. Stiebig, and D. Knipp, "Influence of back contact morphology on light trapping and plasmonic effects in microcrystalline silicon single junction and micromorph tandem solar cells," *Solar Energy Materials and Solar Cells,* vol. 110, pp. 49-57, 3// 2013.
[47] V. Depauw *et al.*, "Micrometer-Thin Crystalline-Silicon Solar Cells Integrating Numerically Optimized 2-D Photonic Crystals," *IEEE Journal of Photovoltaics,* vol. 4, no. 1, pp. 215-223, 2014.
[48] M. C. Putnam *et al.*, "Si microwire-array solar cells," *Energy & Environmental Science,* 10.1039/C0EE00014K vol. 3, no. 8, pp. 1037-1041, 2010.
[49] M. D. Kelzenberg *et al.*, "High-performance Si microwire photovoltaics," *Energy & Environmental Science,* 10.1039/C0EE00549E vol. 4, no. 3, pp. 866-871, 2011.
[50] W. Kern and A. A. Puotinen, "Cleaning Solutions Based on Hydrogen Peroxide for Use in Silicon Semiconductor Technology," *RCA review,* vol. 31, pp. 187-206, 1970.
[51] W. H. Southwell, "Gradient-index antireflection coatings," *Optics Letters,* vol. 8, no. 11, pp. 584-586, 1983/11/01 1983.

[52] X. Liu, P. R. Coxon, M. Peters, B. Hoex, J. M. Cole, and D. J. Fray, "Black silicon: fabrication methods, properties and solar energy applications," *Energy & Environmental Science,* 10.1039/C4EE01152J vol. 7, no. 10, pp. 3223-3263, 2014.

[53] L. Sainiemi *et al.*, "Non-Reflecting Silicon and Polymer Surfaces by Plasma Etching and Replication," *Advanced Materials,* vol. 23, no. 1, pp. 122-126, 2011.

[54] S. J. Cho, T. An, and G. Lim, "Three-dimensionally designed anti-reflective silicon surfaces for perfect absorption of light," *Chemical Communications,* 10.1039/C4CC07341J vol. 50, no. 99, pp. 15710-15713, 2014.

[55] K. E. Plass *et al.*, "Flexible Polymer-Embedded Si Wire Arrays," *Advanced Materials,* vol. 21, no. 3, pp. 325-328, 2009.

[56] D. B. Turner-Evans, H. Emmer, C. T. Chen, and H. A. Atwater, "Flexible, Transparent Contacts for Inorganic Nanostructures and Thin Films," *Advanced Materials,* vol. 25, no. 29, pp. 4018-4022, 2013.

[57] Y. A. Akimov, W. S. Koh, and K. Ostrikov, "Enhancement of optical absorption in thin-film solar cells through the excitation of higher-order nanoparticle plasmon modes," *Optics Express,* vol. 17, no. 12, pp. 10195-10205, 2009/06/08 2009.

[58] E. D. Kosten, E. L. Warren, and H. A. Atwater, "Ray optical light trapping in silicon microwires: exceeding the 2n2 intensity limit," *Optics Express,* vol. 19, no. 4, pp. 3316-3331, 2011/02/14 2011.

[59] E. Chow *et al.*, "Three-dimensional control of light in a two-dimensional photonic crystal slab," *Nature,* vol. 407, no. 6807, p. 983, 2000.

[60] J. D. Joannopoulos, P. R. Villeneuve, and S. Fan, "Photonic crystals: putting a new twist on light," *Nature,* 10.1038/386143a0 vol. 386, no. 6621, pp. 143-149, 03/13/print 1997.

[61] J. D. J. S. G. J. J. N. W. R. D. Meade, *Photonic Crystals: Molding the Flow of Light*, 2nd ed. Princeton: Princeton University Press, 2008.

[62] K. T. Fountaine, C. G. Kendall, and H. A. Atwater, "Near-unity broadband absorption designs for semiconducting nanowire arrays via localized radial mode excitation," (in English), *Optics Express,* Article vol. 22, no. 9, pp. A930-A940, May 2014.

[63] G. Grzela, R. Paniagua-Domínguez, T. Barten, Y. Fontana, J. A. Sánchez-Gil, and J. Gómez Rivas, "Nanowire antenna emission," *Nano letters,* vol. 12, no. 11, pp. 5481-5486, 2012.

[64] L. Cao *et al.*, "Semiconductor nanowire optical antenna solar absorbers," *Nano letters,* vol. 10, no. 2, pp. 439-445, 2010.

[65] K. T. Fountaine, W. S. Whitney, H. A. Atwater, and Ieee, "Achieving Near-Unity Broadband Absorption in Sparse Arrays of GaAs NWs via a Fundamental Understanding of Localized Radial Modes," (in English), *2014 Ieee 40th Photovoltaic Specialist Conference (Pvsc),* Proceedings Paper pp. 3507-3509, 2014.

[66] K. T. Fountaine, W. S. Whitney, and H. A. Atwater, "Resonant absorption in semiconductor nanowires and nanowire arrays: Relating leaky waveguide modes to Bloch photonic crystal modes," (in English), *Journal of Applied Physics,* Article vol. 116, no. 15, p. 6, Oct 2014, Art. no. 153106.

[67] E. Garnett and P. D. Yang, "Light Trapping in Silicon Nanowire Solar Cells," (in English), *Nano Letters,* vol. 10, no. 3, pp. 1082-1087, Mar 2010.

[68] L. Y. Cao, J. S. White, J. S. Park, J. A. Schuller, B. M. Clemens, and M. L. Brongersma, "Engineering light absorption in semiconductor nanowire devices," (in English), *Nature Materials,* Article vol. 8, no. 8, pp. 643-647, Aug 2009.

[69] M. Dasog, A. I. Carim, S. Yalamanchili, H. A. Atwater, and N. S. Lewis, "Profiling Photoinduced Carrier Generation in Semiconductor Microwire Arrays via Photoelectrochemical Metal Deposition," *Nano Letters*, vol. 16, no. 8, pp. 5015-5021, 2016/08/10 2016.

[70] L. Hu and G. Chen, "Analysis of Optical Absorption in Silicon Nanowire Arrays for Photovoltaic Applications," *Nano Letters*, vol. 7, no. 11, pp. 3249-3252, 2007/11/01 2007.

[71] D. R. Abujetas, R. Paniagua-Dominguez, and J. A. Sanchez-Gil, "Unraveling the Janus Role of Mie Resonances and Leaky/Guided Modes in Semiconductor Nanowire Absorption for Enhanced Light Harvesting," (in English), *Acs Photonics*, Article vol. 2, no. 7, pp. 921-929, Jul 2015.

[72] N. Anttu and H. Q. Xu, "Coupling of Light into Nanowire Arrays and Subsequent Absorption," (in English), *Journal of Nanoscience and Nanotechnology*, Article; Proceedings Paper vol. 10, no. 11, pp. 7183-7187, Nov 2010.

[73] A. W. S. J. Love, *Optical Waveguide Theory*. Spring Science & Business Media, 2012.

[74] S. Rein, *Lifetime Spectroscopy - A Method of Defect Characterization in Silicon for Photovoltaic Applications*. Springer Series in Materials Science, 2005.

[75] H. Savin *et al.*, "Black silicon solar cells with interdigitated back-contacts achieve 22.1% efficiency," *Nat Nano*, Article vol. 10, no. 7, pp. 624-628, 07//print 2015.

[76] S. Rein, "Lifetime measurement techniques," in *Lifetime Spectroscopy - A method of defect characterization in silicon for photovoltaic applications*Germany: Springer, 2005, pp. 59-68.

[77] W. Shockley and W. T. Read, "Statistics of the Recombinations of Holes and Electrons," *Physical Review*, vol. 87, no. 5, pp. 835-842, 09/01/ 1952.

[78] P. Auger, "Sur les rayons β secondaires produits dans un gaz par des rayons X," *C.R.A.S.*, vol. 177, 1923.

[79] M. A. Green, "Accuracy of analytical expressions for solar cell fill factors," *Solar Cells*, vol. 7, no. 3, pp. 337-340, 1982/12/01 1982.

[80] Z. Yu, A. Raman, and S. Fan, "Fundamental limit of nanophotonic light trapping in solar cells," *Proceedings of the National Academy of Sciences*, vol. 107, no. 41, pp. 17491-17496, October 12, 2010 2010.

[81] D. M. Callahan, J. N. Munday, and H. A. Atwater, "Solar Cell Light Trapping beyond the Ray Optic Limit," *Nano Letters*, vol. 12, no. 1, pp. 214-218, 2012/01/11 2012.

[82] E. V. Kerschaver and G. Beaucarne, "Back-contact solar cells: a review," *Progress in Photovoltaics: Research and Applications*, vol. 14, no. 2, pp. 107-123, 2006.

[83] S. Wang *et al.*, "Large-Area Free-Standing Ultrathin Single-Crystal Silicon as Processable Materials," *Nano Letters*, vol. 13, no. 9, pp. 4393-4398, 2013/09/11 2013.

[84] S. Ardo, S. H. Park, E. L. Warren, and N. S. Lewis, "Unassisted solar-driven photoelectrosynthetic HI splitting using membrane-embedded Si microwire arrays," *Energy & Environmental Science*, 10.1039/C5EE00227C vol. 8, no. 5, pp. 1484-1492, 2015.

[85] S. W. Boettcher *et al.*, "Photoelectrochemical Hydrogen Evolution Using Si Microwire Arrays," *Journal of the American Chemical Society*, vol. 133, no. 5, pp. 1216-1219, 2011/02/09 2011.

[86] J. R. Maiolo *et al.*, "High Aspect Ratio Silicon Wire Array Photoelectrochemical Cells," *Journal of the American Chemical Society*, vol. 129, no. 41, pp. 12346-12347, 2007/10/01 2007.

[87] M. G. Walter *et al.*, "Solar Water Splitting Cells," *Chemical Reviews,* vol. 110, no. 11, pp. 6446-6473, 2010/11/10 2010.
[88] E. L. Warren, H. A. Atwater, and N. S. Lewis, "Silicon Microwire Arrays for Solar Energy-Conversion Applications," *The Journal of Physical Chemistry C,* vol. 118, no. 2, pp. 747-759, 2014/01/16 2014.
[89] L. Cao, J. S. White, J. S. Park, J. A. Schuller, B. M. Clemens, and M. L. Brongersma, "Engineering light absorption in semiconductor nanowire devices," *Nat Mater,* vol. 8, no. 8, pp. 643-647, Aug 2009.
[90] S. Liu, Z. R. Tang, Y. Sun, J. C. Colmenares, and Y. J. Xu, "One-dimension-based spatially ordered architectures for solar energy conversion," *Chem Soc Rev,* vol. 44, no. 15, pp. 5053-5075, Aug 7 2015.
[91] M. Dasog, J. Kehrle, B. Rieger, and J. G. Veinot, "Silicon Nanocrystals and Silicon-Polymer Hybrids: Synthesis, Surface Engineering, and Applications," *Angewandte Chemie International Edition,* vol. 55, no. 7, pp. 2322-2339, Feb 2016.
[92] F. Wang, A. Dong, and W. E. Buhro, "Solution-Liquid-Solid Synthesis, Properties, and Applications of One-Dimensional Colloidal Semiconductor Nanorods and Nanowires," *Chemical Reviews,* p. DOI: 10.1021/acs.chemrev.5b00701, Mar 14 2016.
[93] A. J. Shields, "Semiconductor quantum light sources," *Nature Photonics,* vol. 1, pp. 215-223, 2007.
[94] A. J. Hoffman *et al.*, "Negative refraction in semiconductor metamaterials," *Nat Mater,* vol. 6, no. 12, pp. 946-950, Dec 2007.
[95] R. Yan, D. Gargas, and P. Yang, "Nanowire photonics," *Nature Photonics,* vol. 3, no. 10, pp. 569-576, 2009.
[96] A. J. Nozik, M. C. Beard, J. M. Luther, M. Law, R. J. Ellingson, and J. C. Johnson, "Semiconductor Quantum Dots and Quantum Dot Arrays and Applications of Multiple Exciton Generation to Third-Generation Photovoltaic Solar Cells," *Chemical Reviews,* vol. 110, pp. 6873-6890, 2010.
[97] A. J. Nozik, "Nanoscience and nanostructures for photovoltaics and solar fuels," *Nano Lett,* vol. 10, no. 8, pp. 2735-2741, Aug 11 2010.
[98] P. P. Boix *et al.*, "From Flat to Nanostructured Photovoltaics - Balance between Thickness of the Absorber and Charge Screening in Sensitized Solar Cells," *ACS Nano,* vol. 6, no. 1, pp. 873-880, 2012.
[99] G. H. Carey, A. L. Abdelhady, Z. Ning, S. M. Thon, O. M. Bakr, and E. H. Sargent, "Colloidal Quantum Dot Solar Cells," *Chem Rev,* vol. 115, no. 23, pp. 12732-12763, Dec 9 2015.
[100] F. S. Kim, G. Ren, and S. A. Jenekhe, "One-Dimensional Nanostructures of π-Conjugated Molecular Systems: Assembly, Properties, and Applications from Photovoltaics, Sensors, and Nanophotonics to Nanoelectronics†," *Chemistry of Materials,* vol. 23, no. 3, pp. 682-732, 2011.
[101] P. J. Price, "Mesostructure Electronics," *IEEE Transactions on Electron Devices,* vol. 28, no. 8, pp. 911-914, 1981.
[102] P. V. Kamat, "Meeting the Clean Energy Demand: Nanostructure Architectures for Solar Energy Conversion," *Journal of Physical Chemistry C,* vol. 111, pp. 2834-2860, 2007.
[103] R. M. Navarro Yerga, M. C. Alvarez Galvan, F. del Valle, J. A. Villoria de la Mano, and J. L. Fierro, "Water splitting on semiconductor catalysts under visible-light irradiation," *ChemSusChem,* vol. 2, no. 6, pp. 471-485, 2009.

[104] M. G. Walter *et al.*, "Solar Water Splitting Cells," *Chemical Reviews,* vol. 110, pp. 6446-6473, 2010.
[105] C. J. Murphy, "Optical Sensing with Quantum Dots," *Anal. Chem.,* vol. 74, no. 19, pp. 520A-526A, 2002.
[106] A. Kolmakov and M. Moskovits, "Chemical Sensing and Catalysis by One-Dimensional Metal-Oxide Nanostructures," *Annual Review of Materials Research,* vol. 34, no. 1, pp. 151-180, 2004.
[107] B. M. Kayes, M. A. Filler, M. C. Putnam, M. D. Kelzenberg, N. S. Lewis, and H. A. Atwater, "Growth of vertically aligned Si wire arrays over large areas (>1 cm^2) with Au and Cu catalysts," *Applied Physics Letters,* vol. 91, no. 10, p. 103110, 2007.
[108] Y. Wu, H. Yan, and P. Yang, "Semiconductor nanowire array: potential susbstrates for photocatalysis and photovoltaics," *Topics in Catalysis,* vol. 19, no. 2, pp. 197-202, 2002.
[109] X. Duan, J. Wang, and C. M. Lieber, "Synthesis and optical properties of gallium arsenide nanowires," *Applied Physics Letters,* vol. 76, no. 9, pp. 1116-1118, 2000.
[110] Y. Yang *et al.*, "Synthesis of PbTe Nanowire Array using Lithographically Patterned Nanowire Electrodeposition," *Nano Letters,* vol. 8, no. 8, pp. 2447-2451, 2008.
[111] L. Li, Y. Yang, X. Huang, G. Li, and L. Zhang, "Fabrication and Characterization of Single-Crystalline ZnTe Nanowires Arrays," *J. Phys. Chem. B,* vol. 109, pp. 12394-12398, 2005.
[112] Y. Wu, H. Yan, M. Huang, B. Messer, J. H. Song, and P. Yang, "Inorganic Semiconductor Nanowires: Rational Growth, Assembly, and Novel Properties," *Chem. Eur. J.,* vol. 8, no. 6, pp. 1260-1268, 2002.
[113] D. Routkevitch, A. A. Tager, J. Haruyama, D. Almalwai, M. Moskovits, and J. M. Xu, "Nonlithographic Nano-Wire Arrays: Fabrication, Physics, and Device Applications," *IEEE Transactions on Electron Devices,* vol. 43, no. 10, pp. 1646-1658, 1996.
[114] S. M. Collins, J. M. Hankett, A. I. Carim, and S. Maldonado, "Preparation of photoactive ZnGeP2 nanowire films," *Journal of Materials Chemistry,* vol. 22, no. 14, pp. 6613-6622, 2012.
[115] T. Vo, A. J. Williamson, and G. Galli, "First principles simulations of the structural and electronic properties of silicon nanowires," *Physical Review B,* vol. 74, no. 4, p. 045116, 2006.
[116] W. I. Park, G. Zheng, X. Jiang, B. Tian, and C. M. Lieber, "Controlled Synthesis of Millimeter-long Silicon Nanowires with Uniform Electronic Properties," *Nano Letters,* vol. 8, no. 9, pp. 3004-3009, 2008.
[117] M. Yao *et al.*, "GaAs nanowire array solar cells with axial p-i-n junctions," *Nano Lett,* vol. 14, no. 6, pp. 3293-3303, Jun 11 2014.
[118] C. Xiang, A. C. Meng, and N. S. Lewis, "Evaluation and optimization of mass transport of redox species in silicon microwire-array photoelectrodes," *Proc Natl Acad Sci U S A,* vol. 109, no. 39, pp. 15622-15627, Sep 25 2012.
[119] T. J. Kempa, R. W. Day, S.-K. Kim, H.-G. Park, and C. M. Lieber, "Semiconductor nanowires: a platform for exploring limits and concepts for nano-enabled solar cells," *Energy & Environmental Science,* vol. 6, no. 3, p. 719, 2013.
[120] K. T. Fountaine and H. A. Atwater, "Mesoscale modeling of photoelectrochemical devices: light absorption and carrier collection in monolithic, tandem, Si|WO3 microwires," *Opt. Express,* vol. 22, no. S6, pp. A1453-A1461, Oct 20 2014.

[121] H. Alaeian, A. C. Atre, and J. A. Dionne, "Optimized light absorption in Si wire array solar cells," *J. Opt.*, vol. 14, no. 2, p. 024006, 2012.
[122] K. T. Fountaine, W. S. Whitney, and H. A. Atwater, "Resonant absorption in semiconductor nanowires and nanowire arrays: Relating leaky waveguide modes to Bloch photonic crystal modes," *Journal of Applied Physics*, vol. 116, no. 15, p. 153106, 2014.
[123] K. T. Fountaine, C. G. Kendall, and H. A. Atwater, "Near-unity broadband absorption designs for semiconducting nanowire arrays via localized radial mode excitation," *Opt. Express*, vol. 22, no. S3, pp. A930-A940, May 5 2014.
[124] P. A. M. Hotsenpiller, J. D. Bolt, W. E. Farneth, J. B. Lowekamp, and G. S. Rohrer, "Orientation Dependence of Photochemical Reactions on TiO_2 Surfaces," *J. Phys. Chem. B*, vol. 102, pp. 3216-3226, 1998.
[125] A. E. Attard and D. E. Brown, "Photoelectroplating Light Modulator," *Applied Optics*, vol. 7, no. 3, pp. 511-516, 1968.
[126] T. Inoue, A. Fujishima, and K. Honda, "Photoelectrochromic Characteristics of Photoelectrochemical Imaging System with a Semiconductor/Solution (Metallic Ion) Junction," *J. Electrochem. Soc.*, vol. 127, no. 7, pp. 1582-1588, 1980.
[127] S. Morishita, "Photoelectrochemical Deposition of Copper on TiO_2 Particles. Generation of Copper Patterns without Photoresists," *Chemistry Letters*, vol. 21, no. 10, pp. 1979-1982, 1992.
[128] S. Yoshihara, K. Shinozaki, T. Shirakashi, K. Hashimoto, D. A. Tryk, and A. Fujishima, "Photoelectrodeposition of copper on boron-doped diamond films: application to conductive pattern formation on diamond. The photographic diamond surface phenomenon," (in English), *Electrochimica Acta*, Article vol. 44, no. 16, pp. 2711-2719, 1999.
[129] R. H. Micheels, A. D. Darrow, and R. D. Rauh, "Photoelectrochemical deposition of microscopic metal film patterns on Si and GaAas," *Applied Physics Letters*, vol. 39, no. 5, pp. 418-420, 1981.
[130] M. D. Kelzenberg *et al.*, "Enhanced absorption and carrier collection in Si wire arrays for photovoltaic applications," *Nat Mater*, vol. 9, no. 3, pp. 239-244, Mar 2010.
[131] M. Gharghi, E. Fathi, B. Kante, S. Sivoththaman, and X. Zhang, "Heterojunction silicon microwire solar cells," *Nano Lett*, vol. 12, no. 12, pp. 6278-6282, Dec 12 2012.
[132] S. W. Boettcher *et al.*, "Energy-Conversion Properties of Vapor-Liquid-Solid-Grown Silicon Wire-Array Photocathodes," *Science (Washington, DC, United States)*, vol. 327, pp. 185-187, 2010.
[133] I. Park, Z. Li, A. P. Pisano, and R. S. Williams, "Top-down fabricated silicon nanowire sensors for real-time chemical detection," *Nanotechnology*, vol. 21, no. 1, p. 015501, Jan 8 2010.
[134] D. R. Abujetas, R. Paniagua-Domínguez, and J. A. Sánchez-Gil, "Unraveling the Janus Role of Mie Resonances and Leaky/Guided Modes in Semiconductor Nanowire Absorption for Enhanced Light Harvesting," *ACS Photonics*, vol. 2, no. 7, pp. 921-929, 2015.
[135] K.-S. Choi, "Shape Control of Inorganic Materials via Electrodeposition," *Dalton Transactions*, 10.1039/B807848C no. 40, pp. 5432-5438, 2008.
[136] C. M. McShane and K.-S. Choi, "Photocurrent Enhancement of n-Type Cu2O Electrodes Achieved by Controlling Dendritic Branching Growth," *Journal of the American Chemical Society*, vol. 131, pp. 2561-2569, 2009.

[137] A. I. Carim, S. M. Collins, J. M. Foley, and S. Maldonado, "Benchtop Electrochemical Liquid–Liquid–Solid Growth of Nanostructured Crystalline Germanium," *Journal of the American Chemical Society,* vol. 133, no. 34, pp. 13292-13295, 2011/08/31 2011.
[138] F. Wang, V. L. Wayman, R. A. Loomis, and W. E. Buhro, "Solution-Liquid-Solid Growth of Semiconductor Quantum-Wire Films," *ACS Nano,* vol. 5, no. 6, pp. 5188-5194, 2011.
[139] A. I. Carim, N. A. Batara, A. Premkumar, H. A. Atwater, and N. S. Lewis, "Polarization Control of Morphological Pattern Orientation During Light-Mediated Synthesis of Nanostructured Se-Te Films," *ACS Nano,* vol. 10, pp. 102-111, 2016.
[140] R. M. Penner, "Electrodeposited Nanophotonics," *The Journal of Physical Chemistry C,* vol. 118, no. 31, pp. 17179-17192, 2014.
[141] P. A. Kohl, "Photoelectrochemical etching of semiconductors," *IBM J. Res. Develop.,* vol. 42, no. 5, pp. 629-637, 1998.
[142] Y. Zhao, N. M. Vargas-Barbosa, E. A. Hernandez-Pagan, and T. E. Mallouk, "Anodic deposition of colloidal iridium oxide thin films from hexahydroxyiridate(IV) solutions," *Small,* vol. 7, no. 14, pp. 2087-2093, Jul 18 2011.
[143] F. W. Ostermayer, P. A. Kohl, and R. H. Burton, "Photoelectrochemical etching of integral lenses on InGaAsP/InP light-emitting diodes," *Applied Physics Letters,* vol. 43, no. 7, pp. 642-644, 1983.
[144] R. M. Lum, A. M. Glass, F. W. Ostermayer, P. A. Kohl, A. A. Ballman, and R. A. Logan, "Holographic photoelectrochemical etching of diffraction gratings in n-InP and n-GaInAsP for distributed feedback lasers," *Journal of Applied Physics,* vol. 57, no. 1, pp. 39-44, 1985.
[145] D. S. Barth *et al.*, "Macroscale Transformation Optics Enabled by Photoelectrochemical Etching," *Advanced Materials (Weinheim, Germany),* vol. 27, no. 40, pp. 6131-6136, Oct 28 2015.
[146] A. I. Carim, N. A. Batara, A. Premkumar, H. A. Atwater, and N. S. Lewis, "Self-Optimizing Photoelectrochemical Growth of Nanopatterned Se-Te Films in Response to the Spectral Distribution of Incident Illumination," *Nano Lett,* vol. 15, no. 10, pp. 7071-7076, Oct 14 2015.
[147] D. Kang, T. W. Kim, S. R. Kubota, A. C. Cardiel, H. G. Cha, and K. S. Choi, "Electrochemical Synthesis of Photoelectrodes and Catalysts for Use in Solar Water Splitting," *Chem Rev,* vol. 115, no. 23, pp. 12839-12887, Dec 9 2015.
[148] A. Heller and R. G. Vadimsky, "Efficient Solar to Chemical Conversion: 12% Efficient Photoassisted Electrolysis in the [*p*-type InP(Ru)]/HCl-KCl/Pt(Rh) Cell," *Physical Review Letters,* vol. 46, no. 17, pp. 1153-1156, 1981.
[149] E. Aharon-Shalom and A. Heller, "Efficient p-InP(Rh-H alloy) and p-InP(Re-H alloy) Hydrogen Evolving Photocathodes," *J. Electrochem. Soc.,* vol. 129, no. 12, pp. 2865-2866, 1982.
[150] A. Heller, D. E. Aspnes, J. D. Porter, T. T. Sheng, and R. G. Vadimsky, ""Transparent" Metals: Preparation and Characterization of Light-Transmitting Platinum Films," *J. Phys. Chem.,* vol. 89, pp. 4444-4452, 1985.
[151] W. W. Wu *et al.*, "Growth of multiple metal/semiconductor nanoheterostructures through point and line contact reactions," *Nano Lett,* vol. 10, no. 10, pp. 3984-3989, Oct 13 2010.
[152] B. M. Kayes, H. A. Atwater, and N. S. Lewis, "Comparison of the Device Physics Principles of Planar and Radial p-n Junction Nanorod Solar Cells," *J. Appl. Phys.,* vol. 97, no. 11, p. 114302, 2005.

[153] D. C. Bookbinder, J. A. Bruce, R. N. Dominey, N. S. Lewis, and M. S. Wrighton, "Synthesis and characterization of a photosensitive interface for hydrogen generation: Chemically modified p-type semiconducting silicon photocathodes," *Proceedings of the National Academy of Sciences*, 10.1073/pnas.77.11.6280 vol. 77, no. 11, p. 6280, 1980.

[154] Q. Huang, Z. Ye, and X. Xiao, "Recent progress in photocathodes for hydrogen evolution," *Journal of Materials Chemistry A*, 10.1039/C5TA03594E vol. 3, no. 31, pp. 15824-15837, 2015.

[155] Y. Nakato, Y. Egi, M. Hiramoto, and H. Tsubomura, "Hydrogen evolution and iodine reduction on an illuminated n-p junction silicon electrode and its application to efficient solar photoelectrolysis of hydrogen iodide," *The Journal of Physical Chemistry*, vol. 88, no. 19, pp. 4218-4222, 1984/09/01 1984.

[156] B. Kumar, M. Llorente, J. Froehlich, T. Dang, A. Sathrum, and C. P. Kubiak, "Photochemical and Photoelectrochemical Reduction of CO2," *Annual Review of Physical Chemistry*, vol. 63, no. 1, pp. 541-569, 2012.

[157] J. L. White *et al.*, "Light-Driven Heterogeneous Reduction of Carbon Dioxide: Photocatalysts and Photoelectrodes," *Chemical Reviews*, vol. 115, no. 23, pp. 12888-12935, 2015/12/09 2015.

[158] M. Ali *et al.*, "Nanostructured photoelectrochemical solar cell for nitrogen reduction using plasmon-enhanced black silicon," *Nature Communications*, Article vol. 7, p. 11335, 04/20/online 2016.

[159] T. Oshikiri, K. Ueno, and H. Misawa, "Plasmon-Induced Ammonia Synthesis through Nitrogen Photofixation with Visible Light Irradiation," *Angewandte Chemie International Edition*, vol. 53, no. 37, pp. 9802-9805, 2014/09/08 2014.

[160] E. L. Warren, J. R. McKone, H. A. Atwater, H. B. Gray, and N. S. Lewis, "Hydrogen-evolution characteristics of Ni–Mo-coated, radial junction, n+p-silicon microwire array photocathodes," *Energy & Environmental Science*, 10.1039/C2EE23192A vol. 5, no. 11, pp. 9653-9661, 2012.

[161] C. W. Roske *et al.*, "Comparison of the Performance of CoP-Coated and Pt-Coated Radial Junction n+p-Silicon Microwire-Array Photocathodes for the Sunlight-Driven Reduction of Water to H2(g)," *The Journal of Physical Chemistry Letters*, vol. 6, no. 9, pp. 1679-1683, 2015/05/07 2015.

[162] W. Vijselaar *et al.*, "Spatial decoupling of light absorption and catalytic activity of Ni–Mo-loaded high-aspect-ratio silicon microwire photocathodes," *Nature Energy*, vol. 3, no. 3, pp. 185-192, 2018/03/01 2018.

[163] K. R. McIntosh and S. C. Baker-Finch, "OPAL 2: Rapid optical simulation of silicon solar cells," in *2012 38th IEEE Photovoltaic Specialists Conference*, 2012, pp. 000265-000271.

[164] S. Rühle, "Tabulated values of the Shockley–Queisser limit for single junction solar cells," *Solar Energy*, vol. 130, pp. 139-147, 2016/06/01/ 2016.

[165] A. Vázquez-Guardado, J. Boroumand, D. Franklin, and D. Chanda, "Broadband angle-independent antireflection coatings on nanostructured light trapping solar cells," *Physical Review Materials*, vol. 2, no. 3, p. 035201, 03/22/ 2018.

[166] Z. Chen, S. Ye, A. R. Wilson, Y.-C. Ha, and B. J. Wiley, "Optically transparent hydrogen evolution catalysts made from networks of copper–platinum core–shell nanowires," *Energy & Environmental Science*, 10.1039/C4EE00211C vol. 7, no. 4, pp. 1461-1467, 2014.

[167] Q. Ding *et al.*, "Designing Efficient Solar-Driven Hydrogen Evolution Photocathodes Using Semitransparent MoQxCly (Q = S, Se) Catalysts on Si Micropyramids," *Advanced Materials,* vol. 27, no. 41, pp. 6511-6518, 2015.

[168] Y. Chen, K. Sun, H. Audesirk, C. Xiang, and N. S. Lewis, "A quantitative analysis of the efficiency of solar-driven water-splitting device designs based on tandem photoabsorbers patterned with islands of metallic electrocatalysts," *Energy & Environmental Science,* 10.1039/C5EE00311C vol. 8, pp. 1736-1747, 2015.

[169] M. R. Shaner, J. R. McKone, H. B. Gray, and N. S. Lewis, "Functional integration of Ni–Mo electrocatalysts with Si microwire array photocathodes to simultaneously achieve high fill factors and light-limited photocurrent densities for solar-driven hydrogen evolution," *Energy & Environmental Science,* 10.1039/C5EE01076D vol. 8, no. 10, pp. 2977-2984, 2015.

[170] M. Cabán-Acevedo *et al.*, "Efficient hydrogen evolution catalysis using ternary pyrite-type cobalt phosphosulphide," *Nature Materials,* Article vol. 14, p. 1245, 09/14/online 2015.

[171] X.-Q. Bao, M. Fatima Cerqueira, P. Alpuim, and L. Liu, "Silicon nanowire arrays coupled with cobalt phosphide spheres as low-cost photocathodes for efficient solar hydrogen evolution," *Chemical Communications,* 10.1039/C5CC02331A vol. 51, no. 53, pp. 10742-10745, 2015.

[172] P. Dai, J. Xie, M. T. Mayer, X. Yang, J. Zhan, and D. Wang, "Solar Hydrogen Generation by Silicon Nanowires Modified with Platinum Nanoparticle Catalysts by Atomic Layer Deposition," *Angewandte Chemie International Edition,* vol. 52, no. 42, pp. 11119-11123, 2013.

[173] N. P. Dasgupta, C. Liu, S. Andrews, F. B. Prinz, and P. Yang, "Atomic Layer Deposition of Platinum Catalysts on Nanowire Surfaces for Photoelectrochemical Water Reduction," *Journal of the American Chemical Society,* vol. 135, no. 35, pp. 12932-12935, 2013/09/04 2013.

[174] Z. Huang *et al.*, "Tungsten Sulfide Enhancing Solar-Driven Hydrogen Production from Silicon Nanowires," *ACS Applied Materials & Interfaces,* vol. 6, no. 13, pp. 10408-10414, 2014/07/09 2014.

[175] Z. Huang, C. Wang, L. Pan, F. Tian, X. Zhang, and C. Zhang, "Enhanced photoelectrochemical hydrogen production using silicon nanowires@MoS3," *Nano Energy,* vol. 2, no. 6, pp. 1337-1346, 2013/11/01/ 2013.

[176] I. Oh, J. Kye, and S. Hwang, "Enhanced Photoelectrochemical Hydrogen Production from Silicon Nanowire Array Photocathode," *Nano Letters,* vol. 12, no. 1, pp. 298-302, 2012/01/11 2012.

[177] U. Sim *et al.*, "N-doped graphene quantum sheets on silicon nanowire photocathodes for hydrogen production," *Energy & Environmental Science,* 10.1039/C4EE03607G vol. 8, no. 4, pp. 1329-1338, 2015.

[178] Y. Yang, M. Wang, P. Zhang, W. Wang, H. Han, and L. Sun, "Evident Enhancement of Photoelectrochemical Hydrogen Production by Electroless Deposition of M-B (M = Ni, Co) Catalysts on Silicon Nanowire Arrays," *ACS Applied Materials & Interfaces,* vol. 8, no. 44, pp. 30143-30151, 2016/11/09 2016.

[179] H. Zhang *et al.*, "A p-Si/NiCoSex core/shell nanopillar array photocathode for enhanced photoelectrochemical hydrogen production," *Energy & Environmental Science,* 10.1039/C6EE02215D vol. 9, no. 10, pp. 3113-3119, 2016.

[180] L. Zhang, C. Liu, A. B. Wong, J. Resasco, and P. Yang, "MoS2-wrapped silicon nanowires for photoelectrochemical water reduction," *Nano Research*, journal article vol. 8, no. 1, pp. 281-287, January 01 2015.
[181] J. R. McKone *et al.*, "Evaluation of Pt, Ni, and Ni–Mo electrocatalysts for hydrogen evolution on crystalline Si electrodes," *Energy & Environmental Science*, 10.1039/C1EE01488A vol. 4, no. 9, pp. 3573-3583, 2011.
[182] M. D. Kelzenberg *et al.*, "Enhanced absorption and carrier collection in Si wire arrays for photovoltaic applications," *Nature Materials*, vol. 9, p. 239, 02/14/online 2010.
[183] K. T. Fountaine, C. G. Kendall, and H. A. Atwater, "Near-unity broadband absorption designs for semiconducting nanowire arrays via localized radial mode excitation," *Optics Express*, vol. 22, no. S3, pp. A930-A940, 2014/05/05 2014.
[184] K. T. Fountaine, W.-H. Cheng, C. R. Bukowsky, and H. A. Atwater, "Near-Unity Unselective Absorption in Sparse InP Nanowire Arrays," *ACS Photonics*, vol. 3, no. 10, pp. 1826-1832, 2016/10/19 2016.
[185] R. Saive *et al.*, "Effectively transparent contacts (ETCs) for solar cells," in *2016 IEEE 43rd Photovoltaic Specialists Conference (PVSC)*, 2016, pp. 3612-3615.
[186] R. H. Coridan *et al.*, "Methods for comparing the performance of energy-conversion systems for use in solar fuels and solar electricity generation," *Energy & Environmental Science*, 10.1039/C5EE00777A vol. 8, pp. 2886-2901, 2015.
[187] P. Mialhe, J. P. Charles, A. Khoury, and G. Bordure, "The diode quality factor of solar cells under illumination," *Journal of Physics D: Applied Physics*, vol. 19, no. 3, p. 483, 1986.
[188] P. A. Kempler, M. A. Gonzalez, K. M. Papadantonakis, and N. S. Lewis, "Hydrogen Evolution with Minimal Parasitic Light Absorption by Dense Co–P Catalyst Films on Structured p-Si Photocathodes," *ACS Energy Letters*, vol. 3, no. 3, pp. 612-617, 2018/03/09 2018.
[189] F. H. Saadi, A. I. Carim, E. Verlage, J. C. Hemminger, N. S. Lewis, and M. P. Soriaga, "CoP as an Acid-Stable Active Electrocatalyst for the Hydrogen-Evolution Reaction: Electrochemical Synthesis, Interfacial Characterization and Performance Evaluation," *J. Phys. Chem. C*, vol. 118, no. 50, pp. 29294-29300, 2014.
[190] F. H. Saadi *et al.*, "Operando Spectroscopic Analysis of CoP Films Electrocatalyzing the Hydrogen-Evolution Reaction," *Journal of the American Chemical Society*, vol. 139, no. 37, pp. 12927-12930, 2017/09/20 2017.
[191] R. Saive *et al.*, "Effectively Transparent Front Contacts for Optoelectronic Devices," *Advanced Optical Materials*, vol. 4, no. 10, pp. 1470-1474, 2016.
[192] R. Saive *et al.*, "Silicon heterojunction solar cells with effectively transparent front contacts," *Sustainable Energy & Fuels*, 10.1039/C7SE00096K vol. 1, no. 3, pp. 593-598, 2017.
[193] D. B. Turner-Evans, C. T. Chen, H. Emmer, W. E. McMahon, and H. A. Atwater, "Optoelectronic analysis of multijunction wire array solar cells," *Journal of Applied Physics*, vol. 114, no. 1, p. 014501, 2013.
[194] C. T. Chen, D. B. Turner-Evans, H. Emmer, S. Aloni, and H. A. Atwater, "Design and growth of III-V on Si microwire array tandem solar cells," in *2013 IEEE 39th Photovoltaic Specialists Conference (PVSC)*, 2013, pp. 3397-3401.
[195] "Light Management in Silicon Solar Cells," in *Photovoltaic Solar Energy*.

[196] S. Manzoor *et al.*, "Improved light management in planar silicon and perovskite solar cells using PDMS scattering layer," *Solar Energy Materials and Solar Cells,* vol. 173, pp. 59-65, 2017/12/01/ 2017.
[197] F. J. Haug and C. Ballif, "Light management in thin film silicon solar cells," *Energy & Environmental Science,* 10.1039/C4EE03346A vol. 8, no. 3, pp. 824-837, 2015.
[198] M. Schmid, "Review on light management by nanostructures in chalcopyrite solar cells," *Semiconductor Science and Technology,* vol. 32, no. 4, p. 043003, 2017.
[199] A. Peer, R. Biswas, J.-M. Park, R. Shinar, and J. Shinar, "Light management in perovskite solar cells and organic LEDs with microlens arrays," *Optics Express,* vol. 25, no. 9, pp. 10704-10709, 2017/05/01 2017.
[200] S. Hu, C. Xiang, S. Haussener, A. D. Berger, and N. S. Lewis, "An analysis of the optimal band gaps of light absorbers in integrated tandem photoelectrochemical water-splitting systems," *Energy & Environmental Science,* 10.1039/C3EE40453F vol. 6, no. 10, pp. 2984-2993, 2013.
[201] K. T. Fountaine, H. J. Lewerenz, and H. A. Atwater, "Efficiency limits for photoelectrochemical water-splitting," *Nature Communications,* Article vol. 7, p. 13706, 12/02/online 2016.
[202] J. Krč, F. Smole, and M. Topič, "Potential of light trapping in microcrystalline silicon solar cells with textured substrates," *Progress in Photovoltaics: Research and Applications,* vol. 11, no. 7, pp. 429-436, 2003.
[203] P. Campbell and M. A. Green, "Light trapping properties of pyramidally textured surfaces," *Journal of Applied Physics,* vol. 62, no. 1, pp. 243-249, 1987.
[204] E. Yablonovitch and G. D. Cody, "Intensity enhancement in textured optical sheets for solar cells," *IEEE Transactions on Electron Devices,* vol. 29, no. 2, pp. 300-305, 1982.
[205] S. Mokkapati and K. R. Catchpole, "Nanophotonic light trapping in solar cells," *Journal of Applied Physics,* vol. 112, no. 10, p. 101101, 2012.
[206] G. Wilson, "The multi-TW scale future for photovoltaics," *AIP Conference Proceedings,* vol. 1924, no. 1, p. 020003, 2018.
[207] M. D. Lammert and R. J. Schwartz, "The interdigitated back contact solar cell: A silicon solar cell for use in concentrated sunlight," *IEEE Transactions on Electron Devices,* vol. 24, no. 4, pp. 337-342, 1977.
[208] M. B. Spitzer and J. C. C. Fan, "Multijunction cells for space applications," *Solar Cells,* vol. 29, no. 2, pp. 183-203, 1990/08/01/ 1990.
[209] E. Verlage *et al.*, "A monolithically integrated, intrinsically safe, 10% efficient, solar-driven water-splitting system based on active, stable earth-abundant electrocatalysts in conjunction with tandem III–V light absorbers protected by amorphous TiO2 films," *Energy & Environmental Science,* 10.1039/C5EE01786F vol. 8, no. 11, pp. 3166-3172, 2015.
[210] X. Zhou *et al.*, "Solar-Driven Reduction of 1 atm of CO2 to Formate at 10% Energy-Conversion Efficiency by Use of a TiO2-Protected III–V Tandem Photoanode in Conjunction with a Bipolar Membrane and a Pd/C Cathode," *ACS Energy Letters,* vol. 1, no. 4, pp. 764-770, 2016/10/14 2016.
[211] W.-H. Cheng *et al.*, "Monolithic Photoelectrochemical Device for Direct Water Splitting with 19% Efficiency," *ACS Energy Letters,* vol. 3, no. 8, pp. 1795-1800, 2018/08/10 2018.
[212] B. Z. Tian *et al.*, "Coaxial silicon nanowires as solar cells and nanoelectronic power sources," (in English), *Nature,* vol. 449, no. 7164, pp. 885-U8, Oct 18 2007.

[213] J. Wallentin *et al.*, "InP Nanowire Array Solar Cells Achieving 13.8% Efficiency by Exceeding the Ray Optics Limit," (in English), *Science,* vol. 339, no. 6123, pp. 1057-1060, Mar 1 2013.
[214] A. Mavrokefalos, S. E. Han, S. Yerci, M. S. Branham, and G. Chen, "Efficient Light Trapping in Inverted Nanopyramid Thin Crystalline Silicon Membranes for Solar Cell Applications," (in English), *Nano Letters,* vol. 12, no. 6, pp. 2792-2796, Jun 2012.
[215] J. Zhu, C. M. Hsu, Z. F. Yu, S. H. Fan, and Y. Cui, "Nanodome Solar Cells with Efficient Light Management and Self-Cleaning," (in English), *Nano Letters,* vol. 10, no. 6, pp. 1979-1984, Jun 2010.
[216] Y. Yao *et al.*, "Broadband light management using low-Q whispering gallery modes in spherical nanoshells," (in English), *Nature Communications,* vol. 3, Feb 2012.
[217] J. Grandidier, D. M. Callahan, J. N. Munday, and H. A. Atwater, "Light Absorption Enhancement in Thin-Film Solar Cells Using Whispering Gallery Modes in Dielectric Nanospheres," (in English), *Advanced Materials,* vol. 23, no. 10, p. 1272, Mar 2011.
[218] R. Kapadia, Z. Y. Fan, K. Takei, and A. Javey, "Nanopillar photovoltaics: Materials, processes, and devices," (in English), *Nano Energy,* vol. 1, no. 1, pp. 132-144, Jan 2012.
[219] V. K. Narasimhan, T. M. Hymel, R. A. Lai, and Y. Cui, "Hybrid Metal-Semiconductor Nano structure for Ultrahigh Optical Absorption and Low Electrical Resistance at Optoelectronic Interfaces," (in English), *Acs Nano,* vol. 9, no. 11, pp. 10590-10597, Nov 2015.
[220] S. Jeong *et al.*, "Hybrid Silicon Nanocone-Polymer Solar Cells," (in English), *Nano Letters,* vol. 12, no. 6, pp. 2971-2976, Jun 2012.
[221] S. Hu, M. R. Shaner, J. A. Beardslee, M. Lichterman, B. S. Brunschwig, and N. S. Lewis, "Amorphous TiO₂ coatings stabilize Si, GaAs, and GaP photoanodes for efficient water oxidation," *Science,* 10.1126/science.1251428 vol. 344, no. 6187, p. 1005, 2014.
[222] M. F. Lichterman *et al.*, "Stabilization of n-cadmium telluride photoanodes for water oxidation to O2(g) in aqueous alkaline electrolytes using amorphous TiO2 films formed by atomic-layer deposition," *Energy & Environmental Science,* 10.1039/C4EE01914H vol. 7, no. 10, pp. 3334-3337, 2014.
[223] M. T. McDowell *et al.*, "The Influence of Structure and Processing on the Behavior of TiO2 Protective Layers for Stabilization of n-Si/TiO2/Ni Photoanodes for Water Oxidation," *ACS Applied Materials & Interfaces,* vol. 7, no. 28, pp. 15189-15199, 2015/07/22 2015.
[224] M. T. McDowell *et al.*, "Improved Stability of Polycrystalline Bismuth Vanadate Photoanodes by Use of Dual-Layer Thin TiO2/Ni Coatings," *The Journal of Physical Chemistry C,* vol. 118, no. 34, pp. 19618-19624, 2014/08/28 2014.
[225] M. R. Shaner, S. Hu, K. Sun, and N. S. Lewis, "Stabilization of Si microwire arrays for solar-driven H2O oxidation to O2(g) in 1.0 M KOH(aq) using conformal coatings of amorphous TiO2," *Energy & Environmental Science,* 10.1039/C4EE03012E vol. 8, no. 1, pp. 203-207, 2015.
[226] J. T. Choy *et al.*, "Integrated TiO2 resonators for visible photonics," *Optics Letters,* vol. 37, no. 4, pp. 539-541, 2012/02/15 2012.
[227] C. C. Evans, C. Liu, and J. Suntivich, "Low-loss titanium dioxide waveguides and resonators using a dielectric lift-off fabrication process," *Optics Express,* vol. 23, no. 9, pp. 11160-11169, 2015/05/04 2015.

[228] C. C. Evans, K. Shtyrkova, J. D. B. Bradley, O. Reshef, E. Ippen, and E. Mazur, "Spectral broadening in anatase titanium dioxide waveguides at telecommunication and near-visible wavelengths," *Optics Express,* vol. 21, no. 15, pp. 18582-18591, 2013/07/29 2013.
[229] C. C. Evans *et al.*, "Multimode phase-matched third-harmonic generation in sub-micrometer-wide anatase TiO2 waveguides," *Optics Express,* vol. 23, no. 6, pp. 7832-7841, 2015/03/23 2015.
[230] X. Guan, H. Hu, L. K. Oxenløwe, and L. H. Frandsen, "Compact titanium dioxide waveguides with high nonlinearity at telecommunication wavelengths," *Optics Express,* vol. 26, no. 2, pp. 1055-1063, 2018/01/22 2018.
[231] J. D. B. Bradley *et al.*, "Submicrometer-wide amorphous and polycrystalline anatase TiO2 waveguides for microphotonic devices," *Optics Express,* vol. 20, no. 21, pp. 23821-23831, 2012/10/08 2012.
[232] S. A. Lee *et al.*, "Tailored NiOx/Ni Cocatalysts on Silicon for Highly Efficient Water Splitting Photoanodes via Pulsed Electrodeposition," *ACS Catalysis,* vol. 8, no. 8, pp. 7261-7269, 2018/08/03 2018.
[233] M. J. Kenney *et al.*, "High-Performance Silicon Photoanodes Passivated with Ultrathin Nickel Films for Water Oxidation," *Science,* 10.1126/science.1241327 vol. 342, no. 6160, p. 836, 2013.
[234] N. S. Lewis, "Research opportunities to advance solar energy utilization," *Science,* 10.1126/science.aad1920 vol. 351, no. 6271, 2016.
[235] S. Y. Herasimenka, W. J. Dauksher, and S. G. Bowden, ">750 mV open circuit voltage measured on 50 μm thick silicon heterojunction solar cell," *Applied Physics Letters,* vol. 103, no. 5, p. 053511, 2013/07/29 2013.
[236] R. Saive and H. A. Atwater, "Mesoscale trumps nanoscale: metallic mesoscale contact morphology for improved light trapping, optical absorption and grid conductance in silicon solar cells," *Optics Express,* vol. 26, no. 6, pp. A275-A282, 2018/03/19 2018.
[237] R. Saive, T. C. R. Russell, and H. A. Atwater, "Enhancing the Power Output of Bifacial Solar Modules by Applying Effectively Transparent Contacts (ETCs) With Light Trapping," *IEEE Journal of Photovoltaics,* vol. 8, no. 5, pp. 1183-1189, 2018.
[238] S. Zhao, R. Jin, and R. Jin, "Opportunities and Challenges in CO2 Reduction by Gold- and Silver-Based Electrocatalysts: From Bulk Metals to Nanoparticles and Atomically Precise Nanoclusters," *ACS Energy Letters,* vol. 3, no. 2, pp. 452-462, 2018/02/09 2018.
[239] E. V. Astrova and G. V. Fedulova, "Formation of deep periodic trenches in photo-electrochemical etching of n-type silicon," *Journal of Micromechanics and Microengineering,* vol. 19, no. 9, p. 095009, 2009.
[240] S. Hu, N. S. Lewis, J. W. Ager, J. Yang, J. R. McKone, and N. C. Strandwitz, "Thin-Film Materials for the Protection of Semiconducting Photoelectrodes in Solar-Fuel Generators," *The Journal of Physical Chemistry C,* vol. 119, no. 43, pp. 24201-24228, 2015/10/29 2015.
[241] H. Yin, L. Longju, J. Michael, C. H. Andrew, and L. Meng, "One-step sol–gel imprint lithography for guided-mode resonance structures," *Nanotechnology,* vol. 27, no. 9, p. 095302, 2016.
[242] M. Liu *et al.*, "Enhanced electrocatalytic CO2 reduction via field-induced reagent concentration," *Nature,* vol. 537, p. 382, 08/03/online 2016.
[243] J. M. Kontio, J. Simonen, J. Tommila, and M. Pessa, "Arrays of metallic nanocones fabricated by UV-nanoimprint lithography," *Microelectronic Engineering,* vol. 87, no. 9, pp. 1711-1715, 2010/11/01/ 2010.